



UNIVERSITY
OF TRENTO

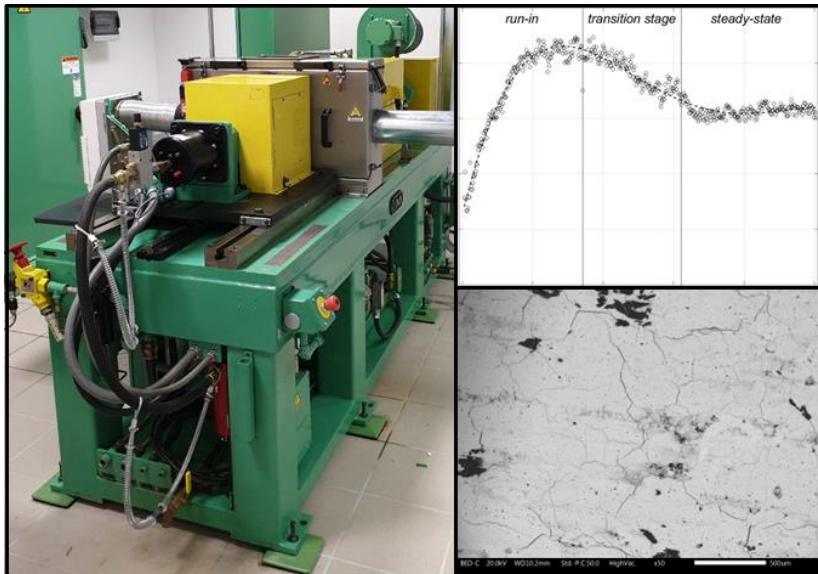
Department of
Industrial Engineering

Doctoral School in Materials, Mechatronics and
System Engineering

XXXV cycle

Brake performance and emission behaviors of brake materials on a sub-scale dynamometer

Stefano Candeo



8th September 2023

Brake performance and emission behaviors of brake materials on a sub-scale dynamometer

Stefano Candeo

E-mail: stefano.candeo@unitn.it

Prof. Giovanni Straffelini, Advisor, Department of Industrial Engineering, *University of Trento*, Italy

Prof. Stefano Gialanella, Department of Industrial Engineering, *University of Trento*, Italy.

Ph.D. Commission:

Prof. Giovanni Bolelli, Department of Materials and Environmental Engineering, *University of Modena and Reggio Emilia*, Italy

Ulf Olofsson, Department of Machine Design, *Royal Institute of Technology (KTH)*, Sweden

*University of Trento,
Department of Industrial Engineering*

University of Trento - Department of Industrial Engineering

Doctoral Thesis

Stefano Candeo – 2023

A Cristina e Francesco

Abstract

Brake materials represent an important source of air pollution, especially in urban areas, where they can contribute to approx. 21 % of the traffic-related particulate matter emission. For this reason, the design of new brake materials with low emissions is a topical issue. In addition to low emissions, the design of new friction materials has to ensure excellent performance with stable coefficients of friction and low wear rate. Due to the several requirements that these materials need to fulfill, their development and testing are complex and intercorrelated. Good performance and low emission strongly depend on the mechanisms acting at the disc-pad interfaces. In this thesis, a brake dynamometer testing protocol is developed to better understand the relationships of the braking parameters with the brake performance and emission behavior, correlating them with the surface characteristics. The surface characteristics were investigated with *a-posteriori* analysis, in terms of extension of the contact area, degree of compaction of the wear particles and relevant composition. The work is focused on the bedding process and the influence of the braking parameters on the frictional, wear and emission behaviors. Regarding the bedding process, run-in, transition stage and steady states were identified as concerns the frictional, wear and emission behaviors. The frictional behavior gets stabilized by the extension of the secondary plateaus, whereas the wear and emission behaviors are stabilized as their degree of compaction increases. The influence of pressure and velocity under mild sliding conditions were studied for a low-met and NAO material, the two most common types of friction materials. The low-met material featured a more stable and higher friction coefficient and lower wear and emissions than the NAO material. The wear behavior is strongly affected by pressure for the NAO material, and for the low-met material, velocity is very influential. Emissions follow a cube relationship with velocity for both materials. The significant differences in the observed behaviors are explained in terms of the different features of the surfaces. The NAO material featured a smooth and uniform surface, with higher coverage than the low-met material, on which steel fibers play important adhesive and abrasive actions. From tests under mild sliding conditions of several friction materials sliding against cast-iron discs, a linear relationship is found between the specific wear rate and the emission factor. This relationship identifies a wear rate below $2.5 \cdot 10^{-14} \text{ m}^2/\text{N}$ complying with the Euro 7 limitation of 3 mg/km/vehicle after 2034. Among the friction materials sliding against cast iron discs, the NAO material and only one friction material displayed an emission factor below the limit of 3 mg/km/vehicle. In addition, the emission factor of low-met material sliding against a cermet-coated disc was lower than this limit. These observations confirm that the NAO materials and coated discs are effective systems to mitigate emissions, whereas further efforts are required to improve the emission behavior of low-met materials. Interestingly, the low-met materials with a reduced presence of secondary plateaus featured higher wear and emissions. Regarding the brake performance, under severe sliding conditions, the NAO material displayed worse frictional and wear behaviors than the reference low-met material. For high-pressure ranges, the effect of pressure is to cause a monotonic decrease in the friction coefficient. The effect of temperature on the friction coefficient causes an increase in the friction coefficient when the tribo-oxidative processes are contained up to 300 °C. For combinations of high velocity and temperature, the tribo-oxidative processes are high enough

to form a thick glaze layer on the surfaces. The glaze layers were correlated to a lubricating effect, or *fade effect*, at disc temperatures above 400 °C, especially when their extension covered the steel fibers. The cermet-coated disc displayed the same fade behavior at high velocity-temperature values, although at low velocities and high temperatures, friction instability was observed and related to larger but fewer patches originating to a significant extent from material transfer from the disc. The friction instability in the coated disc was ascribed to the different tribo-oxidative behavior in the formation of 'glazes' due to the low source of iron in the disc material.

Contents

1. Introduction	1
2. Brake materials for lightweight vehicles - General Concepts	5
2.1 Brake materials	5
2.2 Environmental Aspects Related to the Brake Particle Particle Emissions	7
2.3 Lab-scale testing of Brake Materials	8
3. Wear processes in Brake Materials	9
3.1 Wear mechanisms General Concepts	8
3.2 Adhesive interaction	10
3.3 Abrasive interaction	12
3.4 Third body approach	14
3.5 Tribo-oxidative wear	14
3.6 Bedding process	16
4. Braking System Parameters	19
4.1 Light and heavy braking conditions	19
4.2 Influence on the frictional, wear and emission behaviors	20
5. Experimental setup, Materials and Testing procedures	23
5.1 Sub-scale dynamometer	23
5.1.1 Scaling	23
5.1.2 Linear Variable Differential Transformer measurements for wear evaluation	26
5.1.3 Design of the system for emission measurements	29
5.2 Materials	31
5.2.1 Reference Cu-free low-met friction material	32
5.2.2 NAO friction material	34
5.2.3 Cu-less low-met friction material and coated-disc	35
5.3 Braking Cycles	36
5.3.1 Bedding of SAE J 2707	36
5.3.2 Reduced Cycle	36
5.3.3 Modified SAE J 2522	39
5.3.4 pvT-friction Map Brake Cycle	41
6. Results and Discussion	43
6.1 Bedding process of a low-met friction material	45
6.1.1 Evolution of the friction coefficient, wear rate and emissions	45
6.1.2 Characterization	50
6.1.2.1 Worn surfaces	50
6.1.2.2 Airborne Particulate Matter	55
6.1.2.3 Non-Airborn Particle Matter	58
6.1.3 Main wear mechanisms	59
6.2 Influence of contact pressure and velocity on the brake behavior and fine particulate matter emissions of a low-met and a NAO friction materials	61
6.2.1 Bedding	61

6.2.2	Reference blocks	63
6.2.3	pv-blocks	65
6.2.3.1	Contact temperature	65
6.2.3.2	Friction coefficient	65
6.2.3.3	Wear rate	66
6.2.3.4	Emissions	68
6.2.4	Characterization of the worn surfaces	70
6.2.5	Main wear mechanisms	75
6.3	Relationship between specific wear rate and emission factors for friction materials	79
6.3.1	Specific wear rate	80
6.3.2	Emission factor	81
6.3.3	Characterization of the worn surfaces	84
6.4	Development of a Modified AK-Master Braking Cycle for friction, wear and emission evaluations of brake materials	86
6.4.1	Friction coefficient	86
6.4.2	Wear rate	88
6.4.3	Emissions	89
6.5	Brake performance under mild and severe sliding conditions of a conventional cast iron disc and a cermet-coated disc	91
6.5.1	Contact temperature	92
6.5.2	Friction coefficient	92
6.5.3	Wear rate	98
6.5.4	Characterization of the worn surfaces	99
6.5.4.1	Friction materials	99
6.5.4.2	Discs	106
6.5.5	Main wear mechanisms	108
7.	Conclusions	113
8.	Future Perspectives	117
	Bibliography	118
	Appendix A: Participation in Congresses, Schools and Workshops	125
	Appendix B: List of Publications	126
	Acknowledgements	127

Chapter I

Introduction

Several efforts have been made to develop strategies to reduce particulate matter (PM) emissions in urban environments and the consequent hazards for the environment and human health. A major source of PM in urban areas is particle emissions due to the wear of brake materials of passenger vehicles. Recently, the Euro 7 regulation introduced limits also regarding brake particle emissions. On this basis, the design of new brake materials with lower emissions and without hazardous components in the formulations has become a topical issue.

In addition to these environmental requirements, brake materials should fulfill their basic function. They should have excellent performance: stable coefficients of friction and low wear over a wide range of braking conditions. However, brake performance and the relative particle emissions depend on the material compositions and braking conditions. Different combinations of braking conditions are typically simulated on brake dynamometers according to testing procedures or brake cycles. From this perspective, good testing methodologies will enable effective material development.

In this thesis, the frictional, wear and emission behaviors of commercial and innovative brake materials are studied through the development of specific brake cycles. The adopted approach consists in correlating the behaviors of interest with surface characterization to better understand the tribological processes acting on the surfaces at the tested conditions. The characterization of the worn surfaces and particulate matter was done by scanning electron microscopy (SEM) techniques and composition analysis by energy dispersive X-ray spectroscopy (EDXS) techniques.

Chapters II-IV provide the required background to understand the general aspects of the field and the experimental part of the thesis. Chapter II describes the basic function of a brake system, the classification and design of brake materials, and the environmental aspects related to brake emissions. Whereas Chapter III gives a tribological background on wear processes acting on the brake materials surfaces. Finally, Chapter IV describes the influence of the braking parameters on the frictional, wear, and emission behaviors.

The experimental part of the thesis includes the development of new testing methodologies, or the modification of standard ones, using the sub-scale dynamometer at the University of Trento. This sub-scale dynamometer is equipped with a Linear Variable Differential Transformer (LVDT) sensor to have an evaluation of the wear and was designed for emission measurement with an Optical Particle Sizer (OPS) and an impactor for the collection of the emitted PM. Section 5.1 describes the sub-scale dynamometer: the scaling, the methodology to obtain the wear evaluation from the LVDT measurement and the design of the system for emission measurements. Section 5.2 provides information about the tested

friction materials and discs, whereas Section 5.3 describes the applied braking cycles in the experimental part: the bedding procedure of *SAE J 2707*, the *Reduced Cycle*, a modified version of *SAE J 2522*, and an internal Brembo Procedure to map the brake performance.

First, in Section 6.1, the bedding process of the reference low-met material is considered, focusing on the stability of emissions. Understanding the reason for the stability of emissions is important from a testing perspective as it ensures the representativeness of the following sections in testing methodology. The study identified steady states for the frictional, wear, and emission behaviors with repeated and identical braking conditions. The stabilization of the friction coefficient depends on the stabilization and spreading of the secondary plateaus, whereas the wear and emission stabilization depend on the attainment of a stable composition in the PM and a high degree of compaction of the secondary plateaus.

Section 6.2 deals with the development of a braking cycle, called *Reduced Cycle*, meant to map the frictional, wear, and emission behaviors of brake materials as a function of pressure and velocity. The study is presented as a comparison between a reference low-met and a NAO material. The two friction materials displayed significantly different behaviors, as concerns the variability and sensitivity to the braking parameters, particularly at high velocity. These behaviors were ascribed to the different natures of the friction layers in the two materials. In particular, the significant increase in wear and emissions and the decrease of the friction coefficient at high velocity were correlated to a significant decrease in the extension of the secondary plateaus on the surface of the low-met material.

Several materials have been tested according to the *Reduced Cycle*. Section 6.3 provides the *specific wear rate* and the *emission factors* for the tested materials, drawing an interesting relationship. Most materials comply with the limit of 7 mg/km/vehicle within the limit imposed within 2034 by Euro 7. The NAO and the coated disc couple respect the limit of 3 mg/km/vehicle, which will be issued by 2035, thus confirming such friction materials to represent good strategies to reduce PM emitted from brake systems. However, only one tested low-met material remains below the limit of 3 mg/km/vehicle, suggesting that further developments for this type of material are required.

Section 6.4 describes the proposed *Modified Ak-Master* to include wear and emission evaluation during the testing procedure originally used for brake performances only. This standard procedure is important for comparing the results with the dataset from full-scale dynamometers and to assess the robustness of the methodology. Wear evaluations were specific to different sections of the braking cycle, and the emissions were measured under stable conditions. The results are presented, as done for Section 6.2, as a comparison between the reference low-met and NAO materials. The braking cycle evidenced the significant differences in the frictional and wear behaviors between mild and severe sliding conditions.

The last experimental part, Section 6.5, presents the study of a cycle developed by the Testing Department of the Brembo brake company to map the frictional behavior as a function of pressure, velocity and temperature at severe braking conditions. Herewith, this

cycle will be referred to as the *pvT-friction Map Brake Cycle*. The study compares a cermet-coated disc and a conventional cast iron disc. The brake performance is discussed in terms of friction sensitivity to pressure, velocity and temperature. SEM observations showed that the *fade effect* with temperature is correlated with the primary plateaus being covered by a thick layer of iron oxide for both the brake couples. In addition, the different behavior of the coating and the lower source of Fe were identified as causes for the friction instability for low-intermediate velocities and high temperatures.

Chapter II

Brake materials for lightweight vehicles - General Concepts

The role of a braking system is to reduce the vehicle's speed converting its kinetic energy into mainly thermal energy. The driver starts a braking action by pushing the brake pedal. The actuation of the brakes is hydraulic for light transportation applications: a plunger pump regulates the pressure of the oil in the hydraulic system distributing the pressure into the front and rear axles. Then, the pressure variation into the caliper system engages, through the hydraulic pistons, the brake pads in contact with the discs. As the brake discs are rigidly mounted to the wheel, the frictional force at the pad-disc interface decelerates the rotor and, consequently, the vehicle.

2.1 Brake materials

The transformation of kinetic energy into thermal energy occurs as a consequence of the frictional interaction at the interface of the brake materials: the brake disc and the brake pads. A brake disc should fulfill several requirements. Mechanical integrity to withstand high stresses and high heat dissipation capabilities are paramount requirements. Other important characteristics are wear resistance, generally above 10^5 km, corrosion resistance, low cost, noise and weight [1]. Nowadays, the most used material for conventional brake discs is gray cast iron. However, in the last years, the concern about brake particulate matter emissions increased the interest in discs with improved wear resistance, such as cermet coating on their surfaces [2].

As stated for the brake discs, also friction materials need to meet different requirements. The friction coefficient has to be relatively high and stable over a wide range of braking conditions. Good wear resistance is a paramount characteristic of brake pads in order to extend the lifespan and reduce particulate matter emissions. An important requirement for the formulations is low or zero hazardous constituents for the environment and human health. Other important requirements are mechanical resistance, high thermal and chemical stability, and low level of vibration and noise.

The component of a brake pad that engages the contact with the disc is called *friction material*, and it mainly determines the braking behaviors of the brake pad. The friction material adheres to a rigid steel part, called *backplate*, connected by the *underlayer* and eventually a machined mechanical interlocking.

Organic resins and rubbers in the underlayer provide damping properties to improve comfort during braking. The friction materials for most lightweight vehicles are complex composite materials made of several ingredients embedded in an organic matrix, typically phenolic resin. The ingredients are usually classified according to their role in the frictional behavior into binders, reinforcements, fillers, solid lubricants, and abrasives.

Reinforcements are usually metal fibers or particles to mechanically strengthen the materials. Once steel fibers undergo severe plastic deformation, they represent the so-called *primary plateaus*. Fibers for their relatively high thermal conductivity reduce local temperatures at the interface of the friction materials.

In brake materials, solid lubricants usually refer to laminar solids: graphite, transition metal dichalcogenides, e.g. MoS₂, ceramic materials, such as hBN, and sodium silicates. Laminar solids have a planar or hexagonal layered structure. The atoms within the layers are strongly bonded. However, the individual layers are bonded by weak Van Der Waals forces, providing an easy shear ability that reduces and stabilizes the friction force between the interfaces of the two bodies [3]. Different solid lubricants may degrade or oxidize above a certain temperature losing their function. Thus, in brake pads, different solid lubricants are used to accomplish friction stability in a wide temperature range [4].

On the other hand, abrasives are used to increase the friction coefficient. Typical abrasives used in friction materials are oxides of metals such as Al, Mg, Si and Zr. In the particularly aggressive formulations, ceramic materials such as SiC, WC and NbC could be found. Since solid lubricants and abrasives significantly affect brake performance, special attention should be given to tuning their amounts in the design of friction materials.

Fillers are considered materials tribologically inert and are used to keep low raw material costs. Barite, calcium carbonate, clays, silicates, titanates and expanded mica are examples of fillers used in friction materials [1].

Brake pads for lightweight vehicles can be classified according to their metal content into three main classes: Non-Asbestos Organic (NAO), low-metallic (low-met), and semi-metallic. NAO pads are characterized by the absence of steel and by a non-ferrous metal content lower than 20 wt.%. They generate low noise during the braking action and low emissions. These brake pads are mainly sold in the US and Asian markets. The European market, on the other hand, prefers low-met materials. They have an overall steel fiber content lower than 20 wt.% and are characterized by a good pedal feeling and more noisy behavior during the braking action. Finally, semi-metallic pads have an overall metal content of around 50 wt.%

Regardless of the type of friction materials, the frictional, wear, and emission performance is largely determined by the characteristics of the friction layers that develop on the disc and pad surfaces.

2.2 Environmental Aspects Related to the Brake Particle Emissions

Recent years have seen increasing attention on air quality and on strategies to mitigate the PM in the environment. PM originates from three main sources: industry, domestic activities and road traffic. Traffic-related emissions are of two types, exhaust, e.g. tailpipe emissions, and non-exhaust. The latter generates from tire and brake wear processes and their resuspension.

Exhaust and non-exhaust emissions are approximately equal, according to the review study [5], and brake emissions can account for 21 % of the total traffic-related sources. It is estimated that approximately 40–50% of the brake wear becomes PM, and the rest deposits on the road and the wheel and brake components [6][7][8]. The brake emission factor is typically in the range of 4-10 mg/km per vehicle [9][6].

PM emissions can be classified into primary and secondary emissions. Primary emissions are directly introduced into the atmosphere from combustion or wear processes, while secondary emissions are generated in the atmosphere from the chemical reactions of compounds, such as NO_x, NH₃, SO₂ and volatile organic compounds (VOCs).

According to their size, PM is typically classified into PM₁₀, PM_{2.5} and PM_{0.1} or into coarse, fine and ultrafine particles. The two classifications are slightly different. PM₁₀, PM_{2.5} and PM_{0.1} comprise the particles with an aerodynamic diameter lower respectively of 10 μm, 2.5 μm and 0.1 μm. Whereas coarse, fine and ultrafine particles identify the size ranges respectively of 10-2.5 μm, 1-0.1 μm and below 0.1 μm.

A typical mass distribution of PM in urban areas is characterized by several modes or peaks. The main modes are the coarse and accumulation modes. The coarse mode comprises relatively big particles originating from mechanical wear processes, while both primary emissions from mechanical processes and the condensation and coalescence of compounds into fine particles pertain to the accumulation mode.

The particle size is a particularly important factor as determines the capability to penetrate the human body. The coarse particles are mostly captured in the nose and throat. PM_{2.5} can penetrate deeply into the lung, irritating the alveolar wall and causing oxidative stresses[10][11]. The most hazardous particles are the ultrafine particles displaying higher penetration and residence time. Other important factors that determine the toxicity of inhaled particles are their chemical composition, surface reactivity and agglomeration state. [12][13].

The health impact depends on the specific environment of the compounds, their stoichiometry and the potential reactions, during the braking processes. Asbestos is a well-known ingredient that was removed for its negative health impact. Some metals also are toxic, such as Ni, B, As, Hg, V, Ca, Pb, Cr and Cu. Most metallic elements are emitted as oxides or sulfates. Some metals, however, are emitted in the metallic form, due to their limited reactivity and tendency to oxidize [14]. Metallic copper was progressively reduced from the brake pad formulations over the last years because it was found harmful to different aquatic species [15][16][17]. Iron is the main element of the cast iron disc and it can form different

oxides. A large amount of magnetite (Fe_3O_4) is generated during the tribo-oxidative wear of the cast iron disc. The hazard of magnetite has not been fully assessed yet, although it was generally considered harmful to human health [18].

Finally, gaseous species, such as VOC, may result in ultrafine particle emissions from the complex processes that involve the incomplete decomposition of the organic compounds of the brake pads [19].

2.3 Lab-scale testing of Brake Material

The testing of brake materials can be done both on the field, where real vehicles are employed, and, in a more controlled environment, the laboratory. Tests on the field require, first of all, real vehicles, special instrumentations, and highly specialized personnel, thus they are very expensive. In general tests on the field are useful to assess the overall performance of brake systems and vehicles [1].

Brake dynamometers are typically employed to assess the efficiency of a brake system. The disc is connected to a rotor driven by an electric motor and real components of the caliper-pad systems of a vehicle's corner. Dynamometers usually control the inertia, rotating speed, system pressure or vehicle deceleration, and initial braking disc temperature to simulate brake actions. A type of dynamometer is a reduced scale, like the one used in this work, meaning that they have samples of reduced size. Mechanical similitude usually enables the simulation of comparable conditions with a reference vehicle [20][21].

Regarding the evaluation of emissions, several researchers focused on the design of systems for emission measurements on dynamometers [22][23][24], testing already existing braking cycles [7] and developing new ones [25], such as Los Angeles City Traffic (LACT) [24] and SAE J 2707 [26]. Studies focused on emission measurements directly from a vehicle on the field [27]. recently the Euro7 regulation [5] extended the limit also to non-exhaust emissions. Regarding the brake particle emissions, the limit of PM10 is 7 mg/kg per vehicle PM10 until 2034 to be more than halved, to 3 mg/kg per vehicle from 2035 [28]. The testing procedure is the Worldwide Harmonised Light-Duty Vehicles Test Procedure (WLTP) [29].

Tribometer and Pin on Disc (PoD) set-ups are largely used for the research of materials, especially in the early phase of material design. A pin is held in sliding contact at constant sliding velocity and load. These tests usually last in the range of hours and are suitable for understanding the wear mechanism and assessing tribological behaviors. Many PoD studies focused also on the measurement the emissions [30].

Chapter III

Wear processes in Brake Materials

3.1 Wear mechanisms General Concepts

The wear processes acting at the mating surfaces of brake pads and discs are several and complex due to the heterogeneity of the materials and the nature of the environmental and working conditions. Although this complexity, the wear processes can be comprehensively explained in terms of four wear mechanisms: adhesive wear, abrasive wear, tribo-oxidative and wear by fatigue. Depending on the brake material formulations and the braking conditions, the actual active wear processes in brake materials are the combination of the first three mentioned mechanisms.

For a good comprehension of the wear processes, it is important to consider the contact situation between two surfaces. The actual contact occurs only at the surfaces' asperities, thus the real area of contact is only a fraction of the nominal area. The real area of contact depends both on surface parameters and material properties, which determine the nature of the contact. Regarding the material properties, the tangential force that the two surfaces exert is proportional to the capability to resist processes such as plastic deformation or fracture [31]. In this view, the wear behavior becomes a paramount aspect to control the frictional behavior.

Plasticity and brittleness indexes take into account only the material properties. They are defined as the ratio of $\frac{E}{\sigma_y}$ and $\frac{\sigma_y}{K_{IC}}$ respectively, where E is the elastic modulus, σ_y is the yield strength and K_{IC} is the fracture toughness of the material. In the case of brittle materials, such as ceramics, the presence of microcracks become an important aspect according to the fracture mechanics theory. Thus, an elastic contact is easy for ceramics (high value of $\frac{\sigma_y}{K_{IC}}$) and plastic contact is rather easy for metals (high value of $\frac{E}{\sigma_y}$), whereas polymers do not provide easily elastic or plastic contact as they generally have low yield strength and low toughness. [32]. The plasticity index, Ψ , by Greenwood and Williamson [33] takes into account also the surface parameters in Eq. 3.1:

$$\Psi = \frac{E^*}{H} \sqrt{\frac{\sigma_S}{R_S}} \quad (\text{Eq. 3.1})$$

where E^* proportional to the modulus of elasticity of the two materials, H is the hardness of the softest material, σ_S and R_S are the standard deviation of the asperity height distribution and the asperity radius respectively. For Ψ lower than 0.60 the contact is elastic, for Ψ lower than 1 the plastic contact prevails. The effect of low surface roughness is shifting the contact towards elastic conditions. In practice, metals maintain a plastic contact for the high σ_y , while

ceramics and polymers experience mixed contact. According to the nature of the contact, the relationships for the estimation of the real contact area A_r , have a different formulation; in the case of plastic contact (pl.c.) and elastic contact (el.c.):

$$A_r^{pl.c.} \propto \frac{F_N}{\sigma_y} \quad (\text{Eq. 3.2})$$

$$A_r^{el.c.} \propto \frac{F_N}{E^* \sqrt{R_S}} \quad (\text{Eq. 3.3})$$

Since friction materials contain a large number of different constituents, the contact scenario is particularly complex, the asperities experience elastic, plastic or mixed conditions, depending on the nature of the asperity. The combination of contact-sliding conditions and the interaction with the brake materials determine the change in the wear mechanisms. As mentioned for brake materials the wear process is ascribable to an adhesive interaction, abrasive interaction, and to tribo-oxidation, thus their deeper insights will be represented in the following sections.

3.2 Adhesive interaction

The tangential forces between two bodies in contact may be due to mechanical, chemical, or physical interactions at the asperities. Chemical or adhesive forces arise from the formation of weak van der Waals bonds. Surfaces in the ambient environment undergo natural contaminations of compounds with low-surface energy, such as water and organic compounds, due to the reduction in the free surface energy of the system reducing the adhesion of the surfaces. The evaluation of the adhesive forces is generally expressed through the concept of the work of adhesion per unit area, W_{12} . It represents the energy that must be theoretically supplied to separate two surfaces 1 and 2 in contact. W_{12} can be expressed in terms of the surface energy of the two interfaces, γ_1 , and γ_2 , and when they are in contact, γ_{12} , as in Eq.3.4.

$$W_{12} = \gamma_1 + \gamma_2 - \gamma_{12} = c (\gamma_1 + \gamma_2) \quad (\text{Eq. 3.4})$$

Surface energies, γ , for metals, ceramics and polymers are respectively 1-3 J/m², 0.1-0.5 J/m² for ceramics and 0.1 J/ m² [34]. According to Rabinowitz [35], the work of adhesion can be expressed with the concept of compatibility, between the two surfaces. The work of adhesion is proportional to the compatibility parameter as in the third term in Eq. 3.4. c is 1 in contact with the same metals. The compatibility between two different metals is high when the mutual solubility of the two metals is higher than 1% and is capable of forming intermetallic compounds. In this case, the compatibility parameter, c , has a value of approx. of 0.5. Two metals are considered incompatible if their solubility is lower 0.1 %, in this case, c is approx. 0.1. For ceramics c ranges from 0.35-0.6 respectively for incompatible (oxides of different metals) and compatible ceramics (oxides of the same metal). For polymers, c ranges

between 0.8-0.95. Finally, when materials of different natures are placed in contact c is approx. 0.1.

In many tribological processes, material transfer as a thin film is generally observed in both the mating surfaces, the overall effect of the transfer is the increase of the compatibility as the materials achieve closer compositions.

The adhesive, frictional, force, F_f can be described by the relationship:

$$F_f \propto \tau_f A_r \quad (\text{Eq. 3.5})$$

Where is τ_f shear stress is required to separate asperities in contact and A_r is the real area of contact. The friction coefficient, defined as the ratio between the frictional force and the applied nominal force is presented for plastic contact (Eq. 3.6) and elastic (Eq. 3.7):

$$\mu^{\text{pl.c}} \propto \frac{F_f}{F_N} \propto \frac{\tau_f A_r}{\sigma_y A_r} \propto \frac{W_{12}}{\sigma_y} \quad (\text{Eq. 3.6})$$

$$\mu^{\text{el.c}} \propto \frac{W_{12}}{E^* \sqrt{R_S}} \quad (\text{Eq. 3.7})$$

According to this relationship, the A_r is proportional to the load and A_r is higher for soft materials, σ_y low. Once the applied load exceeds the value at which all the surface in contact yield plastic conditions, the area of contact achieve its maximum value, hence a further increase in the applied load determines a decrease in the friction coefficient. During the operating conditions, the actual value W_{12} , cannot be estimated, and its measure in controlled conditions is not trivial. According to Rabinowicz [36], for solids, in the absence of phase variations, the work of adhesion is not much influenced by temperature, while near the melting point, it can drop by two orders of magnitude. On the other hand, the experimental measurements by Yamamoto and Nakajima [37] adhesive forces were found to increase with temperature with an Arrhenius relation due to the higher activation rate of van der Waals forces.

In the case of elastic contact, surface topography plays a huger role than in the case of plastic contact. As mentioned, since friction materials are heterogeneous materials, applying these concepts, even with a rule of mixture, is not trivial. However, the relevant takeaway from the adhesive interaction is the influence of the work of adhesion of the different materials and its proportionality to the compatibility and mechanical properties as they determine the area of contact.

Moreover, according to Rabinowicz [38] the elastic and adhesive properties of the materials drive the size of the wear particles. A loose particle becomes an actual fragment when the elastic energy stored in the particle exceeds a value proportional to the work of adhesion between the particle and the surface. The critical diameter of the loose particle, d_c , is proportional to the material properties according to Eq. 3.8:

$$d_c \propto \frac{E W_{12}}{\sigma_y^2} \quad (\text{Eq. 3.8})$$

This equation is in agreement with several experimental observations. Metals display the most wear fraction in the coarse particles in the range of 10-100 micrometers. On the other hand, ceramics and hard metals have a lower critical diameter as they have high strength parameters and comparatively low surface energies. The sliding of metals at a relatively high contact temperature, still far from the melting point of the material, promotes the detachment of large fragments. On the other hand, the particle generation shifts towards finer distribution for tribological couples characterized by low work of adhesion W_{12} .

3.3 Abrasive interaction

Another type of interaction that can occur when two bodies are in contact and mutual sliding is abrasive interaction. As the adhesive interaction, also this interaction is characterized by large surface plastic deformations: a hard body exerts a plowing or grooving action on the surface of a softer body.

Depending on the degree of motion of the abrasive particles on the interface between the two materials, two main types of abrasive interaction are defined: *two-body* or *three-body* interactions. In the so-called *two-body* interaction, the abrasive particles are strongly bonded to the abrading body. The two materials are likely to experience an abrasive interaction when the difference in their hardness is about 20–30 %. For this reason, the abrasive particles are typically ceramic particles, whose hardness is in the range of 1000-3000 kg/m². The hardness of metals is very dependent on the content of alloying elements and the heat treatments. Heat-treated steels have relatively high values, below 1000 kg/m², and Aluminum alloys are typically below 400 kg/m². Rabinowicz [39] explained the two-body interaction with a simplified approach: a hard particle, of a conical shape, determines a frictional force as a result of the resistance generating the groove. Contrary to adhesion, this interaction does not imply a relationship with the compatibility between the mating surfaces. The nominal force and the frictional, lateral, force are both proportional to the yield stress of the softest material and the extension of the plastically deformed area of contact by the groove action, respectively the base area of the cone, A_b , and the lateral areal of the cone, A_l . With these considerations, the friction coefficient can be rewritten as in Eq. 3.9.

$$\mu \propto \frac{F_f}{F_N} \propto \frac{\sigma_y A_l}{\sigma_y A_b} \propto \sqrt{1 + \frac{h}{r}} \propto \sqrt{1 + f(\theta)} \quad (\text{Eq.3.9})$$

The influence of the shape of the particle can be expressed in terms of angularity, through the angular attack θ defined as the ratio between the height (h) and radius (r) of the ideal cone. The higher the angularity of the particle, the higher is the abrasive contribution. Regarding particle size, increasing the size of a particle usually increases the wear of the counterface

disc [40]. This suggests that big particles have a higher carrying capacity as the contact is more likely to occur on a particle that engages a higher volume fraction on the surface. A higher local load represents a higher probability to achieve the local plastic conditions and generate the groove on the counterface disc. Moreover, in brake pads, relatively big abrasive particles, above approx. 100 μm , can act like primary plateaus promoting the formation of secondary plateaus [41]. In two-body abrasion, the wear of the surface is proportional to the size of the abrasive particle and load and is less affected by the sliding velocity [40]. The friction coefficient usually increases with the applied load, as an effect of the angular attack of the particles. When a certain depth, depending on the particle sizes, is achieved the friction coefficient is less sensitive to an increase in the load as a disproportional increase in the lateral area of contact [42]. In brake materials, usually, the effect of the load is different as hard particles are pressed into the matrix, thus a lower portion of the particle contributes to the abrasion at increasing loads [43]. In general, the addition of abrasives in brake pads has the effect of increasing the friction coefficient and the wear of the disc [14].

An important physical property that influences the abrasive interaction is fracture toughness, as it drives the damage mechanisms of materials. For instance, particles, such as quartz and magnesia particles, with a low fracture toughness displayed a decrease in the frictional force at higher applied loads owing to the progressive fracture or blunting, of the asperities [43].

The second type is the *three-body* interaction, where the hard is confined at the interface with the possibility of motion, typically rolling. In three-body abrasion conditions, lower friction coefficient and wear rate are expected because the contact between the abrasive particle and the surface is sliding rather than rolling.

In *three-body* abrasion, the scenario is complex: the degree of motion of the particles depends on their bonding to the material's surface, the shape of the particles, and the topography of the surfaces. In addition, different sliding conditions can have a significant influence on the type of abrasive interaction. For instance, the applied load can vary the mean distance between the two surfaces, decreasing the possibility of movement of the particles, hence promoting the *two-body* interaction [44]. The sliding speed increases the energy of the particles and their mobility promoting the *third-body* on the second-body abrasion. In addition, third-body abrasion can occur when the bodies have comparable hardness and the particles are not able to remain fixed in either of the two bodies. In brake materials depending on the application, abrasive interactions towards the counterface disc are controlled as the iron from the counterface disc form the secondary plateaus. Moreover, abrasive particles embed into the secondary plateaus promote a type of two-body abrasion acting at the microscale [45].

3.4 Third body concept

In the previous section, a third body was related to an abrasive interaction, hence the negative effect on the wear of the softest body. On the other hand, the concept of the *third body* by Godet [46] has positive effects on friction and wear behaviors of the surfaces in contact. This third body represents an interface between the two bodies composed of particles detached from the sliding surfaces. According to this concept [47], the third body embodies several functions that can explain peculiar wear and frictional behaviors of mating surfaces. The third body has the capability of carrying the load and accommodating the velocity through the motion and compaction of the particles. As a barrier between the two bodies, it generally decreases the wear of the system. Moreover, this concept considers the particles flow dynamic results in the emitted particles from the tribosystem. According to Eq. 3.10, the mass of the third body M_B , decrease or increase whether the flow of the emitted particles, Q_e , is respectively higher or lower than the flow of the particles wearing from the two bodies, Q_w .

$$\frac{dM_B}{dt} = Q_w - Q_e \quad (\text{Eq 3.10})$$

Q_w and Q_e depend on the wear rate, thus the sliding conditions, and how the particles interact with the nature and topography of the surfaces. The high capability of the surface to trap the particles and the capability of the particles to agglomerate and bond with the substrate means high dwell time on the surface, resulting in a better protective action of the third body and a reduction in the particle leaving the tribosystem as emissions.

The particles forming the third body usually have a mixed composition between the two bodies in contact as a consequence of a process of mechanical mixing. The contact conditions of local pressure, and temperature combined with the working environment will give rise to physical-chemical processes which result in further variation in the composition. Tribo-oxidation is one of these and is the main process occurring at the interface, it will be discussed in the next section.

3.5 Tribo-oxidative wear

Most metals are thermodynamically unstable in the air reducing their surface energy by reacting with oxygen to form oxides. The oxides develop in layers providing a protective action from the environment, and when sliding under load they may reduce the wear of the two bodies in contact acting as a *third body*. During sliding, the wear particles are progressively oxidized and compacted into layers, generally called *friction layers*. The layers have high defect density, due to mechanical milling, and are reactive owing to the high specific surface area. Then, two competitive processes are the breakdown and the consolidation of the friction layers. Once a very compacted layer is formed, it is often referred

to as 'glaze'[48]. On the other hand, if the layers are not very well compacted, the particles become loose contributing to wear. The flow of the loose particles may also increase the wear by the mechanism of three-body abrasion.

Jiang, Stott, and Stack [49] described the condition of the detachment of particles with the relationship:

$$\sigma_a \propto \frac{\gamma_p N_p}{D_p} \quad (\text{Eq. 3.11})$$

Where σ_a is the tensile stress required to detach the number of particles, N_p , of a diameter D_p . γ_p is the surface energy of the particles. The particles of bigger diameter require comparatively lower stress to detach from the agglomerate. Inversely, big particles have a lower probability to be incorporated into the agglomerate. However, the relationship shows the dependency on the particle numbers N_p , which implies a source of material, and, most importantly, the surface energy of the particles, γ_p , which could vary according to the degree of compaction of the friction layer and the former sliding conditions.

As brake discs are usually made of cast iron, it is interesting to understand the tribo-oxidative behavior of steel at different sliding conditions. Stott identified three tribo-oxidative regimes for steels that depend mainly on sliding velocity and temperature [48]. Below 1 m/s, the friction layer is composed of not well-compacted particles mostly of metallic nature. Above 1 m/s and below 250 °C, the friction layers are composed mainly of loosely-compacted particles. However, the intermediate sintering and oxidation conditions allow for the formation of 'glazes' structures. These are the conditions of the so-called *mild wear* named after the mild oxidation conditions rather than the wear rate. In fact, above 10 m/s and 250 °C, the sintering and oxidization rates are high and the friction layers are composed exclusively of 'glaze' structures. The wear mechanism is the spallation of the oxides, where the critical thickness is identified as approx. 10 μm for steels [48]. These are severe oxidation conditions, however, the wear is generally lower due to the protective action of the thick oxide layers. In particular, above 570 °C the high frictional heat might melt locally the oxide. This can be envisaged with the concept of *flash* temperatures: during sliding, the temperature of the asperities is significantly higher than the mean temperature [50]. Above this temperature, the oxidation rate significantly increases because the formation of the FeO phase, rather than Fe₃O₄ phase, is favored and is highly defective, thus it represents a poor barrier to diffusion of reactants.

For brake pads, in general, iron-oxide layers form on the surfaces, the so-called secondary plateaus. However, the wear generally increases with the temperature as the organic binder reaches the degradation temperature and the secondary plateaus might not find a proper substrate [51].

3.6 Bedding process

The tribological response of brake materials is intimately related to the characteristics of the friction layer that develops on the surfaces during braking [52][53][54][55][56]. As the friction layer is not present on the virgin surfaces, the initial performance is significantly different from braking performance in the service conditions. The initial stage of sliding when the friction layer and the surface achieve the service conditions is called bedding or running-in [57][58]. Conformal geometry is attained by the removal of large asperities, plastic deformation, and wear of the constituents of the friction materials and the disc counterface.

The friction layer formation is slightly different in friction materials with and without steel fibers. In the first case, in low-met and semi-metallic friction, the interaction between fibers and hard abrasives with the disc counterface produces wear debris by a mixed adhesion and abrasion mechanism. Of course, wear debris originates from the entire heterogeneous surface of the friction materials. The wear iron debris follows the tribo-oxidative process, previously described for metal surfaces: the iron debris is heavily deformed and oxidized into small particles of Fe-oxide, mainly hematite Fe_2O_3 . As the process of mechanical mixing proceeds, the debris is progressively crushed, deformed and compacted. Fibers or hard particles are favorable locations for the compaction of debris acting as a mechanical support and obstacle to the particle flow. For this, fibers or hard particles are generally referred to as *primary plateaus*, whereas the compacted Fe-oxide layers are called *secondary plateaus* [59].

NAO materials are typical friction materials without large fibers or hard particles. In this case, the picture is different, the surface of NAO materials, due to the absence of large hard particles or fibers is more uniform than in low-met materials. This results in a more evenly distributed contact and not just restricted to specific regions. Typical values of average roughness R_a for NAO materials are reported as approx. $2 \mu\text{m}$, whereas for low-met the R_a is generally higher, around $7 \mu\text{m}$ [60][61].

The size of particles influences the compaction of the secondary plateaus. Secondary plateaus form by the compaction of sub-micrometric particles. Other ingredients of the pad influence the secondary plateaus entering it as inclusions. Soft ingredients may help the consolidation of the layers during the mechanical mixing process. Pad ingredients with a low fracture toughness, such as barite, zircon, alumina, metal sulfides and silicates, are likely to wear into finer particles from commutation-like processes. In addition, the heavy plastic deformation of steel and other ingredients with relatively high fracture toughness allows the formation of nano-structures with increased hardness and reduced fracture toughness [14]. As mentioned in the previous sections, the combinations of these processes enable the paramount capability for braking application of the secondary plateaus to accommodate the shear deformations and velocities.

A deep understanding of the secondary plateaus is fundamental as most of the emitted brake particles originate in the friction layers. Several studies evidenced that brake PM is compatible with the composition of the secondary plateaus [53][54].

As mentioned, during the bedding process, the performance of brake materials and the airborne particulate emissions are different from the typical conditions that are encountered during steady state or service conditions [14][62][59]. Thus, from a testing perspective, the bedding process is a paramount factor as transient conditions should not be considered representative of service conditions. Brake dynamometer testing procedures usually have specific initial sections to stabilize the brake performance through the development of proper friction layers on the mating surfaces. This allows for a proper evaluation of the brake performance in the subsequent sections of the testing procedure. These sections typically adopt mild brake conditions attained through brake stops in the same [26] or different [63][63] braking conditions.

Finally, the stabilization of brake emissions is an important aspect due to the demand for regulation and the relative infancy of the field. In a recent investigation, Matejka et al. [64] studied the evolution of the emission of airborne particles during repeated tests of a modified SAE J 2707 dynamometer cycle. One of the main outputs of this study is the assessment of higher emissions with unused pads when compared to subsequent tests carried out with used pads. Therefore, a certain degree of wear process is required to guarantee the attainment of stable and reliable conditions. The stabilization of emissions was correlated to the stabilization of collected particulate matter and worn surfaces. Hesse et al. [65] confirmed this behavior by observing the emission stabilization after three runs of the WLTP cycle. All these observations are in general agreement with the previous tests of Sanders et al. [7].

Chapter IV

Braking system parameters

4.1 Light and heavy braking conditions

The braking conditions cover a wide range depending on the driving scenarios and individual driving styles. Light braking is typical of urban conditions with decelerations approx. of 1-2 m/s², and intermediate velocity, below 50-80 km/h conforming to speed limits. Heavy braking is characterized by higher intensity, such as in emergency scenarios, with deceleration that can exceed 10 m/s² and high velocity above 120-140 km/h. In extreme conditions, the dissipated power can exceed 80 kW with high temperature rises [59][66]. The contact pressure at the interface and the sliding velocity depend on the design of the vehicle and the braking system. For example, in a segment C passenger car, a brake action with a deceleration of 3 m/s², has a contact pressure of approx. 1 MPa, whereas the sliding velocity is approx. 4 m/s at 40 km/h. It is important to point out that light and heavy braking conditions derive from driving scenarios and should not be confused with the mild and severe tribological conditions at the interfaces, which were explained in the previous sections.

The main factors affecting the braking performance are contact pressure, sliding velocity and disc temperature. In dynamometer testing, the sliding velocity and contact pressure are controllable, hence they are independent variables. Disc temperature can be considered partially a derivative variable because it depends on the braking power, however, the initial braking disc temperature can be set. Of course, the thermal history depends on the braking parameters of the previous brake stops, hence this is limited control. In urban driving conditions, the disc temperature typically remains below 140 °C [29]. However, in racing applications, downhill, or depending on the driving styles, the disc temperatures easily exceed 500 °C, as testing such conditions is required by specific sessions of well-known procedure SAE J 2522 [63].

Finally, an important factor for brake materials, poorly assessed in literature so far, is the *load history* [66][67]. It becomes significant especially when the braking conditions cause a significant variation in the overall state of the surface, such as the development of wide layers of *glazes* or, inversely, large damage to the friction layer.

4.2 Influence on the frictional, wear and emission behaviors

The material's performance is determined by the mechanical properties, e.g., stiffness and strength, and the surface conditions, i.e., the characteristics of the friction layers on the disc and pad surfaces. As mentioned, the friction layer on the pad materials depends both on its ingredients, the wear of the counterface disc, and the braking conditions.

Regarding the braking conditions, as mentioned, they consist of different combinations of the braking parameters: contact pressure, sliding velocity and disc temperature. On the assessment of their influence on brake performance, Wahlström et al. [68] studied contact pressure and sliding velocity maps of the friction and wear and emission behaviors of a low-met friction material sliding against a cast iron counter face. The study was on PoD, where the material response was evaluated at steady-state conditions. The friction coefficient, wear rate and emission rate decreased at increasing pressure and velocity. The decrease of friction coefficient with the applied pressure and velocity is a common result across several studies [61][69]. It can be explained in terms of a disproportionately lower increase of contact area compared to the increase of applied load [70][71], and because the thickness of the friction layer increased being easier to shear [68][72].

On dynamometer testing, the influence of braking parameters on the friction coefficient was provided by models by Ostermayer [73] and Ricciardi et al. [74], in association with experimental maps [21]. In the study by Ricciardi et al., the friction coefficient displayed nonlinear behaviors with pressure, velocity and temperature. The friction coefficient first increased at relatively low values of the input variables, whereas it stabilized, at higher values of pressure and disc temperature, and decreased at higher values of velocity. The Authors explained the increase in the friction coefficient with the increase of extension of the secondary plateaus due to the increased pressure and temperature during braking. In this study, the friction coefficient showed the highest sensitivity to temperature than pressure and velocity. A similar increasing trend of the friction coefficient with temperature is generally observed also in PoD tests [75][76]. This behavior is, in part, ascribable to the softening of the matrix and the consequent higher degree of compenetration of the mating surfaces. The softening is confirmed by the decrease of the storage modulus around 200 °C in dynamic mechanical analysis (DMA) [76]. This explains the slight increase in wear rate with the temperature up to 250-400°C. In fact, this temperature range represents a *critical temperature* for wear [14], above which the wear rate increase by at least one order of magnitude [51][71]. Cristol-Bulthé et al. [51] associated the variation of wear behavior, involving the degradation of the phenolic resin. The degradation of the phenolic resin usually ranges between 370-500 °C causing loss of density and cohesion of the matrix activating a higher third body source. The surface of the friction materials in these conditions was characterized by deep lowlands with emerging and large load-bearing fibers and a scarce

presence of secondary plateaus. Similar surface characteristics were also observed by Verma et al. in high-temperature tests [77].

Regarding the emissions, a *critical transition temperature* for emissions was first identified by Nosko and Olofsson [78]. Above 200 °C, the ultrafine fraction dominates the particle number and can contribute up to 60 % of the volume fraction. Alemani et al. [79] evidenced that the particle number above 170–190 °C of disc temperature intensified by 2-4 orders of magnitude regardless of the other braking conditions of contact pressure and sliding velocity. In dynamometer testing the transition temperature was identified between the same temperature range and of the same order of magnitude during WLTP [29] cycle by Vojtišek-Lom *et al.* [80], in the Los Angeles City Traffic (LACT) by Farwick zum Hagen *et al.* [24] and Mathissen et al. [27] and modified SAE J 2707 cycle by Perricone et al. [81]. Perricone et al. [22] and Niemann et al. [82] observed that the occurrence of peaks in the emissions due to the ultrafine fraction is strictly related to the surface conditions, i.e. available organic material, and the load history.

On the influence of the braking parameters on emissions in typical urban driving conditions, Hagino et al. [83] described the effect of contact pressure and sliding speed of regular deceleration brake stops. Niemann et al. proposed a model with pressure-velocity-temperature maps from drag brake stops [67]. The recent studies on dynamometer tests by Liu et al. [84] and Men et al. [85] identified that the dissipated energy and initial vehicle speed are the most important factors determining brake emissions.

Chapter V

Experimental setup, Materials and Testing procedures

The first part of this Chapter, section 5.1 deals with the characteristics of the sub-scale dynamometer and the measurement systems for wear and emission evaluation. Section 5.2 provides information on the materials used in the experimental part of the work. Finally, the braking cycles adopted in the experimental part of the work will be explained in section 5.3.

5.1 Sub-scale dynamometer

5.1.1 Scaling

The sub-scale dynamometer used in this work (Fig. 5.1) is the LINK® model 1200. Reduced-scale machines usually work following scaling relationships [20]. This sub-scale dynamometer is based on a mechanical similitude to guarantee the same sliding velocity, contact pressure, and specific energy to a reference vehicle. The equations in Table 5.1 describe the similitude with a D-segment passenger car. For further information please refer to [21]. The samples have a rectangular geometry, size 12 mm x 30 mm, and were cut from a commercial pad. The counterface disc has a diameter of 120 mm and a thickness of 6 mm. They are shown in Fig. 5. 2.



Fig. 5.1: LINK® model 1200 at the University of Trento.



Fig.5.2: samples used at the sub-scale dynamometer: coupons of friction materials and disc.

Table 5.1: important settings for the subscale dynamometer and actual values for a D-segment passenger car.

	Rotating speed	Pressure	Inertia	Effective radius [mm]	Friction area [cm²]	Inertia [kg m²]
Vehicle	$\omega^V = \frac{v_{vehicle}}{R_{wheel}}$	$\bar{p}_{syst} = \frac{I^V \bar{\alpha}^V}{(A_{pad}^V R_{eff}^V)}$	$I^V = M_{corner} R_{wheel}^2$	136.5	178	110
Sub-scale	$\omega^S = \omega^V \frac{R_{eff}^V}{R_{eff}^S}$	$p_n = \bar{p}_{syst} \frac{A_{piston}^V}{A_{pad}^V}$	$I^S = I^V \left(\frac{R_{eff}^S}{R_{eff}^V} \right)^2 \frac{A_{pad}^S}{A_{pad}^V}$	$50 (\approx \frac{R_{eff}^V}{3})$	$7.2 (\approx \frac{A_{pad}^V}{30})$	$0.66 (\approx \frac{I^V}{150})$

5.1.2 Linear Variable Differential Transformer measurements for wear evaluation

In general, in tribological tests, obtaining wear-related information requires several efforts. A methodology that shortens the required tests and provides reliable results has huge potential from a testing perspective. With this in mind, the signal of displacement from the embedded LVDT was studied to obtain wear evaluation of specific sections, without interrupting the tests, of a given brake cycle. Several wear-related information allows for the study of the relationships between wear and friction, and wear and emissions. These tribological relationships are not yet well understood for brake friction materials, and they represent a paramount aspect in the design of friction materials.

The validation process can be structured into two main steps:

1. Reliability of the measurement system;
2. Comparison of thickness variation measured by LVDT and reference micrometer gauge measurements.

First, the reliability of the LVDT system was studied in three steps:

1. repeated static measurement (no sliding) to assess the repeatability in ideal conditions;
2. comparison of the compressive behavior from the embedded LVDT system and laboratory compressive tests.

These approaches are described in the published study [21]. The repeatability of the thickness variation values associated with the LVDT piston displacement measurement was evaluated by measuring the piston displacement in 30 tests without sliding (speed=0), at a simulated brake pressure of 30 bar. The mean value in time is considered the significant feature for displacement measurement. The standard deviation of the 30 measurements was found to be lower than 0.5 μm .

Typical signals of the piston displacement are shown in Fig 5.3 for different simulated brake pressure at the velocity ranging from 80 to 30 km/h. Regarding the compressive behavior, a good agreement was found comparing the piston displacements obtained at different pressures in static conditions (no sliding), and Fig. 5.4, which confirms the reliability of the measurements of the piston displacements. To check for the validity of this approach, separate tests of 100 brake events were conducted at 30 bar and with an initial vehicle velocity of 80 km/h. The wear thickness variation was obtained as the difference between the mean of the signal of the LVDT displacement during the 1st and 100th brake stops and it was also measured with a micrometer gauge. The value obtained with this procedure was found to be approximately 80-90% of the measured value. The wear estimated by LVDT is lower than the wear measured by the micrometer gauge due to the uncertainties coming from both the measurement systems and the sample geometry. Other sources of uncertainty may arise from trapped particles on the surfaces and the expansion of the materials. These uncertainties are hard to quantify individually. Particles or clusters

should not be bigger than a few μm . Thus, 10 brake stops were considered a sound number to have enough wear (more than $10\ \mu\text{m}$ for the mildest conditions in Section 6.2) to rule out the contribution to the wear of the system. Regarding the thermal expansion of the materials, the control of the brake stops at $100\ ^\circ\text{C}$ of disc temperature should allow for similar material conditions before braking, hence the effect of thermal expansion on the material is not avoidable but constant. Dilatometer tests of the materials and a thermal model of the system should be designed to quantify the uncertainty arising from the thermal expansion. Both uncertainties contribute to an underestimation of the wear of the system, thus they agree with the lower measurement by LVDT than the micrometer gauge. In general, the agreement between the two measurements can be considered relatively good for this field.

In Section 6.2-3, the LVDT is used to obtain wear results of the system wear. Due to the difference in the density and the sliding area between the pad and disc materials, the thickness variation of the pad was found to be at least 20 times higher than the depth of the wear track on the disc. In this regard, as the wear of the system depends on the contribution of the pad and disc wear, the measures by LVDT are affected by the relative wear resistance of the pad-disc system.

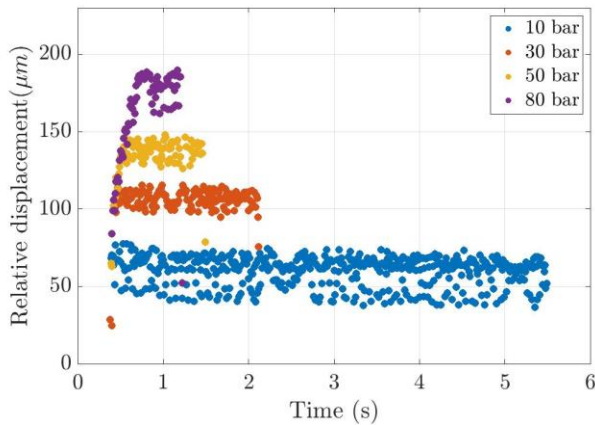


Fig. 5.3: Piston displacements obtained at 10, 30, 50, and 80 bar at vehicle velocity ranging from 80 to 40 km/h.

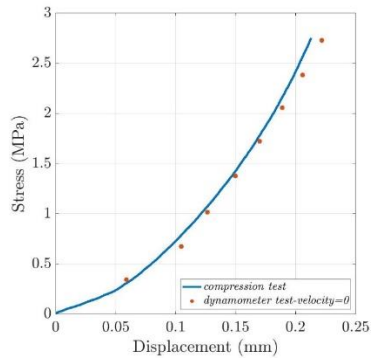


Fig. 5.4: Comparison of the piston displacements at different contact pressures and the displacements obtained with laboratory compression tests at room temperature. The compression tests were carried out using an Instron universal testing machine (Instron 5969) at a cross-head speed of approximately 30 mm/min.

5.1.3 Design of the system for emission measurements

Several instruments for emission measurement are available, based on different working principles, particle size range of interest, and time resolution. In this research, the emitted airborne particles were measured in terms of number (PN) with a TSI® Optical Particle Sizer (OPS). The OPS measured the particle number concentrations up to 3000 particles/cm³ and in the size range 0.3–10 µm, divided into 16 channels. The sampling rate of OPS was 1 L/min with a frequency of 1 Hz. The evolution of particles emitted was then obtained after synchronizing the acquisition of the dynamometer data with those of the OPS using a Matlab® script. In this work, emissions are usually expressed as a mean concentration, where the average was done over 15 s of the OPS signals. At its inlet the OPS is connected to a diluter of factor 10, it dilutes the particle number concentration guaranteeing measurements within the limit of the OPS. An impactor is used for the PM evaluation. It is a Dekati® PM10 Impactor, airborne particles with aerodynamic diameter below 10 µm were collected in three different stages: below 1 µm, 1-2.5 µm, and 2.5-10 µm. The sampling rate of the impactor is 10 L/min. The particles collect on aluminum filters are weighed before and after the tests using an analytical balance with repeatability up to 0.5 mg. The collected particles can be characterized by elemental composition and morphological analysis. The scheme of the experimental set-up for the emission measurement system is shown in Fig.5.5. A HEPA filter is placed downstream the fan. The chamber's volume is approx. 45 L. The input airflow velocity was set up to approx. 1.1 ± 0.1 m/s with a flowmeter at the center of the outlet entry section, leading to the airflow of approx. 0.8 m³/min. The exchange rate was 18 times/min, similar to [23]. The nozzle's diameters at the sampling point were chosen to guarantee isokinetic conditions [86] considering the pumping flow of the OPS and impactor, according to Eq. 5.1 plotted in Fig. 5.6 for the pumping flow of the OPS and I10. The nozzle at the sampling point for the OPS and impactor have diameters respectively of 4.3 and 13 mm (Eq. 5.2).

$$Q_{IN} = Q_{OPS} \rightarrow A v_{air} = Q_{OPS} \rightarrow d^2 \frac{\pi}{4} = \frac{Q_{OPS}}{v_{air}} \quad (\text{Eq. 5.1})$$

$$d_{OPS} = \sqrt{\frac{4 Q_{OPS}}{\pi v_{air}}} \quad (\text{Eq. 5.2})$$

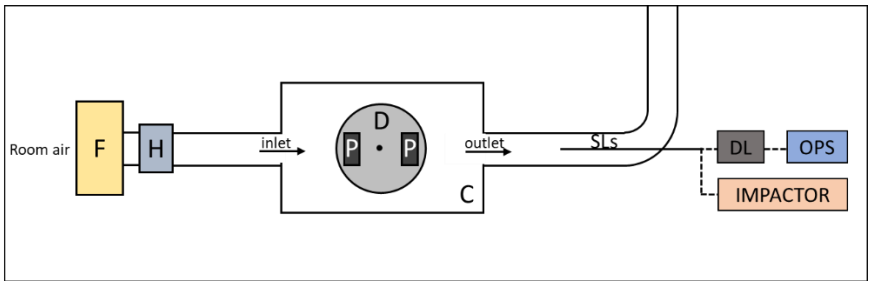


Fig. 5.5: Scheme of the experimental setup. F: fan; H: HEPA filter; C: Chamber; D: disc; P: pad; DL: diluter, SLs: sampling lines; OPS: TSI® OPS, and the impactor.

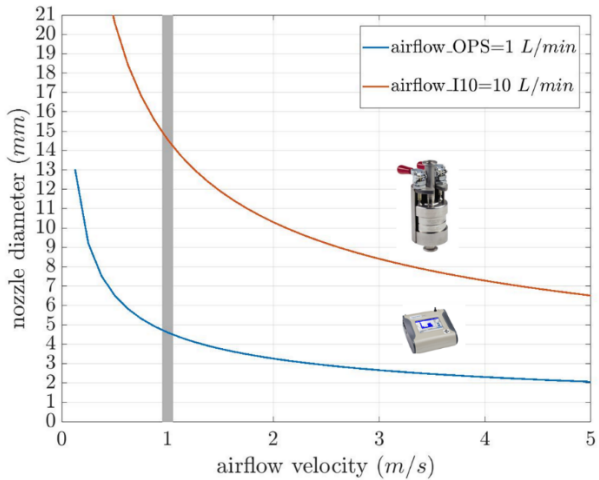


Fig. 5.6: Nozzle diameter as a function of air velocity to match isokinetic conditions with the pumping flow of the OPS and I10. The shaded box refers to these set-up conditions.

5.2 Materials

Table 5.2 gives the tested materials with the respective braking cycles. The braking cycles will be explained in detail in Section 5.3. LM is the reference low-met friction material for all the braking cycles. In Sections 5.2.1 and 5.2.2, the elemental compositions will be provided respectively for the LM and NAO. They were tested with the *Reduced Cycle*. Section 6.2 is dedicated to their comparison, in terms of frictional, wear and emission behaviors. Other modifications of LM (*LM-2, LM-3, LM-4, LM-5, LM-6*) and other NAO materials (*NAO-2, NAO-3*) were tested with the *Reduced Cycle*, but their composition could not be provided for confidential reasons. In these tests, the counterface disc is made of pearlitic grey cast iron with 235 HV10 of hardness. Two test repetitions for each material were done. Section 6.2 will provide the results regarding the relationship between specific wear rates and emission factors for the tested materials. How the specific wear rate and the emissions factors were obtained for the *Reduced Cycle* will be explained in Section 5.3.2. Section 6.2 includes also the results related to a brake couple consisting of Cu-less low-met friction material (*LM-C*) sliding against a cermet-coated disc, whose material information is provided in Section 5.2.3. This latter brake couple was tested with the *pvT-friction Map Brake Cycle* (see Section 5.3.4) to assess the brake performance under severe sliding conditions.

Table 5.2: Summary of materials and braking cycles

	<i>Friction material</i>	<i>Disc</i>	<i>Braking Cycle</i>
<i>LM</i>	Reference Cu-free low-met	Cast-iron	<i>Bedding SAE J 2707; Reduced Cycle; Modified J 2522; pvT-friction Map Brake Cycle.</i>
<i>LM-2:6</i>	Modifications of LM	Cast-iron	<i>Reduced Cycle;</i>
<i>NAO</i>	NAO	Cast-iron	<i>Reduced Cycle; Modified J 2522;</i>
<i>LM-C</i>	Cu-less low-met	Cermet-coated	<i>Reduced Cycle; pvT-friction Map Brake Cycle.</i>

5.2.1 Reference Cu-free low-met friction material

As mentioned, LM is the reference material for all the studies. Its composition measured by energy dispersive X-ray spectroscopy (EDXS) is given in Table 5.3 as the mean value of full-frame measurements in five different regions of the pad. Fig. 5.7 shows the microstructure of the material, with the indication of the main constituents by EDXS mapping: steel fibers, silicates, graphite, vermiculite, tin and iron sulfides, zinc powder, aluminum and magnesium oxides.

Table 5.3: Elemental composition by EDXS of the Cu-free friction (C content not included in the analysis).

Element	wt.%
O	22.3 ± 1.2
Mg	9.6 ± 0.7
Al	8.2 ± 0.5
Si	3.8 ± 0.5
S	8.7 ± 0.3
Ca	4.0 ± 0.4
Cr	2.5 ± 0.3
Fe	18.6 ± 2.1
Zn	12.8 ± 0.8
Sn	9.5 ± 0.8

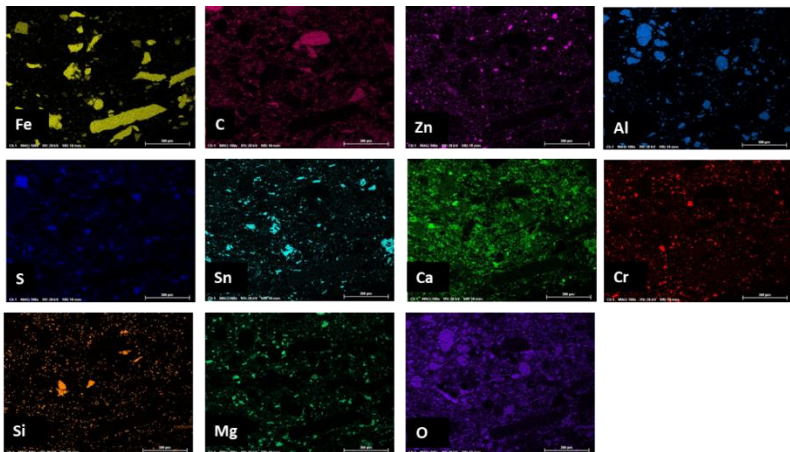
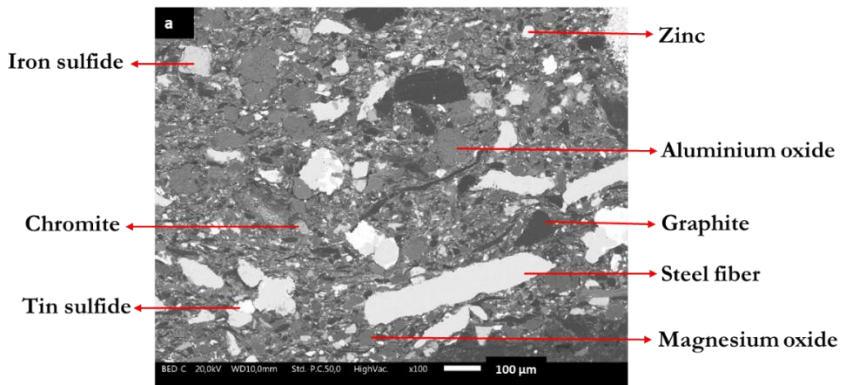


Fig. 5.7: SEM micrographs of the microstructure of the virgin of LM (the reference low-met friction material).

5.2.2 NAO friction material

The elemental composition and the microstructure of the tested NAO materials are provided respectively in Table 5.4 and Fig. 5.8.

Table 5.4: Elemental composition of the NAO friction material, as obtained from EDXS (in weight%). The carbon content was not included in the analysis.

Element	wt.%
O	36.5
Fe	0.9
Zn	-
Mg	2.6
Sn	5.2
S	3.9
Al	2.7
Ca	5.0
Si	5.4
Zr	19.3
Ti	10.0
F	3.3
Na	1.7

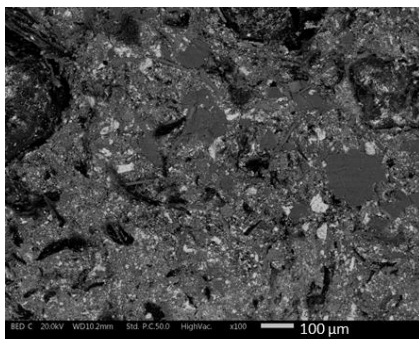


Fig. 5.8: SEM micrographs of the microstructure of the starting NAO friction material.

5.2.3 Cu-less low-met friction material and cermet-coated disc

The elemental composition by EDXS and the microstructure of the friction materials are given respectively in Table 5.5 Fig. 5.9, whereas Table 5.6 provides information about the powder of WC–FeCrAlY coating and carbide particle size. For further information on the coating, please refer to Federici et al. [87].

Table 5.5: Elemental composition of the Cu-less low-met friction material, as obtained from EDXS (in weight %). The carbon content was not included in the analysis.

Element	wt. %
O	14.4
Fe	15.9
Cu	9.7
Zn	5.4
Mg	9.2
Sn	6.6
S	4.9
Al	7.4
Ca	3.7
Si	3.0
Cr	1.9
F	4.0
K	0.5
P	0.6

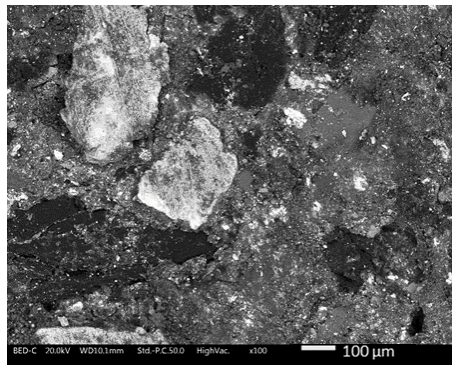


Fig. 5.9: SEM micrographs of the microstructure of the starting Cu-less low met friction material.

Table 5.6: Nominal chemical composition of starting powder of WC–FeCrAlY coating and carbide particle size from [87].

Powder Carbide	Phase	particle size (μm)	Powder particle size (μm)	Metallic matrix-nominal composition
WC– FeCrAlY	83 wt.% WC	1–5	15-45	12 wt.% Fe 3.5 wt.% Cr 1 wt.% Al 0.5 wt.% Y

5.3 Braking Cycle

5.3.1 Bedding of SAE J 2707

As it will be seen in section 6.1, the first study focused on the bedding of the reference low-met friction material. For this study, the bedding of SAE J 2702 was used. This bedding consists of 100 repeated brake stops in the same braking conditions. To better observe the evolution of the emissions, the brake stops were increased to 500 applications. The brake stops are identical and in deceleration mode. The brake stops range from 50 km/h (approx. 4.5 m/s) to 5 km/h with a deceleration of 2.45 m/s². The brake stops have an initial disc temperature of 100 °C. During the brake stops the contact pressure and the maximum disc temperature during braking stabilized respectively around 0.6 MPa and 120 °C. The vehicle characteristics simulated in this braking cycle were typical of a C-segment passenger car.

5.3.2 Reduced Cycle

A consistent part of this experimental work focused on the development of a braking cycle to study the influence of contact pressure and velocity on the friction, wear and emission behavior of brake materials. We developed a simple brake cycle, consisting of initial bedding, followed by randomized brake stop blocks at specific $p-v$ (pressure and velocity) conditions, for this called $p-v$ blocks, and *reference blocks*. A *reference block* was inserted between two subsequent $p-v$ blocks to restore similar conditions on the mating surfaces, and, hence, to have a reliable evaluation of the tribological and emission behaviors in each block. The brake cycle consists of a full factorial design with 2 variables and 4 levels, where the role of reference blocks is similar to center points in the design of experiments [88]. In addition,

before each *pv-block* at high velocity (120 and 160 km/h), a cleaning phase was done to decrease the following increase of emission due only to the rotation at the high speed of the rotor [24]. The cleaning consists of acceleration of the rotor to a vehicle speed of 160 km/h keeping it for approx. 20 s.

The *pv-blocks* have initial vehicle speeds of 40, 80, 120 and 160 km/h, with a velocity variation of 35 km/h, and the simulated brake pressure is 20, 50, 80, 110 bar. All the brake stops started at 100°C of the initial disc temperature. For the bedding and *reference blocks*, the velocity range is 80-30 km/h and a simulated brake pressure of 30 bar. To have a reference to contact pressure, 30 bar corresponds to approx. 1 MPa of contact pressure, and 40 km/h to 4 m/s. The main characteristics of the cycle are reported in Table 5.7. with this cycle, the simulated vehicle was typical of the D-segment passenger car.

Table 5.7: main characteristic of the section of the Reduced Cycle

	Brake pressure (bar)	Initial vehicle speed (km/h)	# brake stops/block	# of blocks
Bedding	30	80	250	1
pv-block	20-110	40-160	10	16
Reference block	30	80	6	16

The braking parameters were chosen to allow a broad comparison in terms of frictional response with the *p-v sensitivity* section of the SAE J 2522 procedure. Regarding the comparison with the *WLTP cycle* for emission evaluations, it should be noted that the *WLTP cycle* has, on average, lower pressures, disc temperatures and velocities. Although these differences, the braking parameters of both the *WLTP cycle* and the *Reduced Cycle* can be considered mild braking conditions.

Section 6.2 will show the results related to the *Reduced Cycle*. the results are presented as a comparison of the reference low-met material (LM) and the NAO material and they were published in [89]. In addition, Section 6.3 will provide the specific wear rate and the emission factor related to the whole cycle for several modifications of the LM, the NAO and the LM-C friction materials. Herewith, the applied methodology to obtain these factors will be explained. The specific wear rates, K_a , were computed by modifying the Archard law [90] for brake stops, originally used for stationary sliding conditions:

$$K_a = \frac{V}{F_N s} = \frac{dT h A_{pad}}{\sum s_i F_{Ni}} = \frac{dT h}{\sum s_i v_i} = \frac{dM/\rho}{\sum s_i F_{Ni}} \quad (\text{Eq. 5.3})$$

Where V is the worn volume, which can be subdivided into the thickness variation, dTh , and area, A_{pad} , of the pads. The second term is usually used to obtain the K_a for stationary PoD

conditions, whereas the third and fourth terms are re-written for dynamometer testing considering respectively the sum of the product of the nominal force, F_N , and contact pressure, p_i , for the sliding distance, s_i , of each brake stop in the braking cycle. The fourth term is expressed in terms of mass loss, dM , and density, ρ . The densities were 7.5 and 13 g/cm³ respectively for cast-iron and coated disc.

The *emission factors* usually depend on the braking cycle because emissions depend on the braking parameters and other characteristics of the brake system and the system for emission measurement as they are defined in terms of vehicle driving distance. The reference is made to the *WLTP cycle*, in which the driving distance is fixed. The stopping distance in the *WLTP cycle* was computed from the motion equations and it is approx. of 14.48 km. Then, depending on the vehicle characteristics (specific rolling radius and effective radius) the sliding distance change from vehicle to vehicle. To compute the *emission factor* for the *Reduced Cycle* maintaining a broad comparison with the *WLTP cycle*, the driving distance was obtained by rescaling the driving distance of the *WLTP cycle*, d_{WLTP} , for the ratio between the sliding distances in the *Reduced Cycle*, s_{RD} , and *WLTP cycle*, s_{WLTP} , according to Eq. 5.4. The two sliding distances were respectively 15 and 5.38 km, and the driving distance for the *WLTP cycle* is approx. 192 km. Then, the emission factors, EF , were obtained with Eq. 5.5:

$$d_{RC} = d_{WLTP} \frac{s_{RC}}{s_{WLTP}} \quad (\text{Eq. 5.4})$$

$$EF = \frac{PM_{10}}{d_{RC}} 4 = \frac{PM_{10}}{s_{RC}} 0.028 * 3 \quad (\text{Eq. 5.5})$$

Where PM_{10} is the mass obtained by the filters of the impactor at the end of the test rescaled by the ratio of the airflow in the channel, 850 m³/min, and the pumping flow of the impactor, 10/min. This factor is approx. 85 times. Finally, factor 3 in Eq. 5.5, converts the vehicle corner into the whole vehicle, considering the variation between the front and rear axles. The *emission factors* obtained in this way are based on the hypothesis expressed by Eq. 5.4. However, as it will be discussed in Section 6.3, from a practical point of view, we found these evaluations very useful as they are in the expected range of 2-10 mg/vehicle/km [5].

5.3.3 Modified SAE J 2522

SAE J 2522, called also as *AK-Master*, is a well-known standard procedure to characterize brake performance. In this section, we propose a modified version of this testing procedure to provide an extensive evaluation of the brake couples with additional information on the emission and wear behavior, not only on the brake performance, or frictional behavior, as the original procedure. The relevance of keeping the reference with this standard procedure is due to the potential comparison to historical datasets from full-scale dynamometers, as well as the robustness of the methodology.

As mentioned, the thickness variations at different groups of sections of the braking cycle were obtained from the LVDT measurements as described in section 5.1.2. The emissions were measured with the OPS following the procedure of Section 5.1.3. The vehicle characteristics simulated in this braking cycle are typical of a D-segment passenger car.

The modifications consisted of:

- a longer bedding procedure to obtain stable conditions for the evaluation of emissions. 7 steps (instead of 2) of bedding for a total of 224 brake stops to achieve stable conditions for the emissions.
- Using the LVDT measurements for wear evaluation of specific sections. The groups of sections were chosen as described in Figure 5.10.
- The addition of *reference blocks*, after each pressure-speed sensitivity block. Plus, the tested simulated brake pressures were 4 instead of 8, respectively: 10, 20, 40 and 80 bar. The cumulative particle number was considered as representative output for the emission evaluation. They were evaluated when stable conditions were attained, i.e., after the longer bedding (see the first point). Then, the cumulative particle number are the sum of 3 additional steps of bedding and the pv-blocks at 40, 80 and 120 km/h and the respective reference blocks. The velocities of 160 and 200 km/h were not accounted for to maintain broad comparability with the WLTP cycle, in which the maximum velocity is approx. 150 km/h. The particle number is obtained with Eq. 5.6:

$$PN = \sum_a^b DF r_{\text{flow}} Q_{\text{air}} C(t) = DF r_{\text{flow}} Q_{\text{air}} \sum_a^b C(t) \quad (\text{Eq. 5.6})$$

Where DF is the dilution factor of 10, Q_{air} is the airflow, and $C(t)$ is the time-series of total concentration as measured from the OPS, and r_{flow} . Point a is the beginning of the steady state and b is the end of the reference block after PV-block at 120 km/h.

- The addition of a more severe *Fade* section. Section *Fade 2* was substituted with a more severe braking condition for performance evaluation at high temperatures. This new section consists of 5 brake stops, the first brake stop has an initial disc temperature of 60°C, while the last brake stop has an initial disc temperature of 450°C. The velocity ranges from 225 to 80 km/h with a brake deceleration of 6.8. m/s². After these 5 brake

stops, a severe brake stop starts at 520 °C from a velocity of 225 to 0 km/h with a deceleration of 10 m/s².

The sections of this brake cycle are summarized in Fig. 5.10. The parts of the cycle used to get the emission evaluation and wear of the specific sections are respectively highlighted in green and red. The brake stop number is also reported.

Modified AK-Master

Section	# brake stops/step	# step	Total brake stops	
Mu green	30	1	30	
Bedding	32	7	224	Emissions
Bedding2	32	3	96	
RefBlock	5	1	5	Wear I
PV40	4	1	4	
RefBlock*	5	1	5	
PV80	4	1	4	
RefBlock*	5	1	5	
PV120	4	1	4	
RefBlock*	5	1	6	
PV160	4	1	4	
RefBlock*	8	1	6	
PV200	4	1	4	
RefBlock	8	1	6	Wear II
Cold application	1	1	1	
Motorway_1	1	1	1	
Motorway_2	1	1	1	
RefBlock	18	1	18	Wear III
Fade 1	15	1	15	
RefBlock	18	1	18	
PV80_2	4	1	4	Wear IV
Increasing Temp	9	1	9	
PV80 Hot	4	1	4	
RefBlock	18	1	18	
Fade 2 (Fade BL) 1	5	1	5	
Fade 2 (Fade BL) 2	1	1	1	
RefBlock	30	1	30	

Fig. 5.10: Modified AK-Master. In green are the subsections for the emission evaluation, and in red are the subsections for the wear evaluation.

5.3.4 pvT-friction Map Brake Cycle

The brake cycle used for the evaluation of frictional behavior under mild and severe sliding conditions was a Brembo internal testing procedure. A study on this braking cycle was already published [91]. Herewith this braking cycle will be referred as to *pvT-friction Map Cycle*. Three initial velocities are tested: 80, 140, and 200 km/h respectively. The velocity range is fixed, it is 75 km/h. The brake pressure ranges from 2 to 14 MPa. The brake cycle is divided into two main parts. The first, *Low-Temperature*, with initial disc temperatures (T) between 50 to 250 °C, and the second, *High-Temperature*, with T between 250 to 650 °C. The separate testing temperature below and above 250 °C represents an important design choice of the experiment. The separation into these two groups was a design choice based on the degradation temperature of the phenolic resin, which starts from 300 °C, as described in Section 4.2. Furthermore, the sliding surfaces at high temperatures usually develop significantly different characteristics compared to mild sliding conditions below 200-300 °C [14]. Another important aspect of the design of this brake cycle is the *preferential order* of the brake stops. In a given brake block, first, velocity and pressure are fixed, and the initial temperatures are changed in increasing order. In the following brake block, the velocity is still fixed but the pressure is increased, and the initial temperatures are changed in decreasing order. The *preferential order* in the brake stops might influence the frictional response, and this hypothesis should be investigated in further studies. The vehicle characteristics simulated in this braking cycle are typical of a D-segment passenger car.

Table 5.8: braking parameters in the *Low-Temperature* and *High-Temperature* sections of the *pvT-friction Maps Brake Cycle*.

	Brake pressure (bar)	Initial vehicle speed (km/h)	Initial disc temperature (°C)
Low temperature	2, 4, 6, 8, 10, 12, 14	70, 140, 200	50, 100, 150, 200, 250
High temperature	2, 4, 6, 8, 10, 12, 14	70, 140, 200	250, 300, 350, 400, 450, 500, 550

To assess the variation and correlation of the friction coefficient with the braking parameters, we obtained respectively the relative standard deviation (*RSD*) and Spearman's coefficient (r_s). Significant changes in these coefficients might underlie variation in the wear mechanism acting at the surfaces. The *Spearman's coefficient* is suggested when the relationship between the two variables is not linear, it is given in Eq. 5.7 for the friction coefficient and brake pressure, as an example:

$$r_{\mu p} = 1 - \frac{6}{N(N^2-1)} \sum_{i=1}^N \frac{(R_{\mu i} - R_{p i})^2}{\sigma_{\mu} \sigma_p} \quad (\text{Eq. 5.7})$$

Where N is the number of elements in the considered sample. σ_{μ} and σ_p are the respective standard deviation of the friction coefficient and the brake pressure. $R_{\mu i}$ is the i -th rank of the μ variable corresponding to the i -th element ranked in decreasing order of the sample. Correspondingly, $R_{p i}$ is the i -th rank of pressure (p), or another variable. $r_{\mu p}$ is obtained for all the combinations of v and T , thus the number of $r_{\mu p}$ will be vT times. For a specific combination of v and T the values of friction coefficient are ranked in decreasing order and associated to the $R_{\mu i}$, in the same way, the pressure is ranked $R_{p i}$ in decreasing order. Of course, the rank for pressures, or the other input variables, are fixed as the experimental points are defined by the design of the experiment. Then, $r_{\mu p}$ is the value between -1 and +1: closer the values to +1 (-1), the two variables are more positively (negatively) correlated.

The relative standard deviation is obtained as the ratio of the standard deviation by the mean of the considered values. The considerations of how the samples were grouped to obtain $r_{\mu p}$ were applied also to the $RSD_{\mu x}$, where x is an input variable, with Eq. 5.8:

$$RSD_{\mu p} = \frac{1}{N-1} \sqrt{\sum_{i=1}^N \frac{(\mu_i - \bar{\mu})^2}{\bar{\mu}}} \quad (\text{Eq. 5.8})$$

The distribution of the RSD and r values depends both on the intimate relationships of the friction coefficient with the considered parameter and the design of the experiment as history influences these types of materials [59].

Chapter VI

Results and discussion

The experimental part of the thesis consisted of the development of new testing methodologies or the modification of standard testing procedures to study the frictional, wear and emission behaviors of brake materials and better understand the relationships among these behaviors. As mentioned in Chapter 1, the results of the experimental part are divided into five sections. The aim of the study for each experimental part is summarized in Table 6.1.

Table 6.1: Summary of the sections of the experimental part with applied braking cycle, tested materials and aim of the study.

Section	Study	Materials	Brake Cycle	Aim
6.1	<i>Bedding process of a low-met friction material</i>	- LM	<i>Bedding of SAE J 2707</i>	<ul style="list-style-type: none"> - <i>Definition of steady states for frictional, wear and emission behaviors;</i> - <i>Identification of relationships between states and surface characteristics.</i>
6.2	<i>Influence of contact pressure and velocity on the brake behavior and fine particulate matter emissions of a low-met and NAO friction material</i>	- LM - NAO	<i>Reduced Cycle</i>	<ul style="list-style-type: none"> - <i>Development of a methodology to study the influence of pressure and velocity on frictional, wear and emission behaviors of brake materials;</i> - <i>Study variability of frictional and emission behaviors;</i> - <i>Highlighting the differences between low-met and NAO friction materials</i> - <i>Correlation between observed behaviors and surface characteristics.</i>
6.3	<i>Relationship between specific wear rate and emission factor of brake materials</i>	- LM-2 - LM-3 - LM-4 - LM-5 - LM-6 - NAO - NAO-2 - NAO-3 - FM-C	<i>Reduced Cycle</i>	<ul style="list-style-type: none"> - <i>Obtaining emission factor</i> - <i>Relating the emission factors with the material wear;</i> - <i>Correlation between observed behaviors and surface characteristics.</i>

6.4	<i>Development of a Modified AK-Master Braking Cycle for frictional, wear and emission evaluations of brake materials</i>	- LM - NAO	<i>Modified SAE J 25 22</i>	<ul style="list-style-type: none"> - Addition of emission and wear evaluations to the friction characterization in the SAE j 2522 - Testing more severe fade conditions - Highlighting the differences between low-met and NAO friction materials
6.5	<i>Brake performance at mild and severe sliding conditions of conventional cast iron and cermet-coated discs</i>	- FM - FM-C	<i>pvT-friction Map Cycle</i>	<ul style="list-style-type: none"> - Develop a methodology to study the influence of pressure, velocity and temperature on the frictional behavior of brake materials; - Highlight the differences between cast-iron and coated discs - Correlation between observed behaviors and surface characteristics.

6.1 Bedding process of a low-met friction material

As mentioned in Section 3.6, tribological tests usually comprise an initial part, called bedding, in which the sliding surfaces acquire the service conditions, i.e., they develop a good degree of geometrical conformity and the characteristic friction layer. At the end of the bedding section, the tribological characteristics achieve a good degree of stability. Due to the relatively recent studies on the emissions for brake materials, it is important to investigate how the emission achieves stability from pristine conditions.

This study focuses on the evolution of the frictional, wear and emission behaviors of the reference LM friction material during the bedding process. The bedding procedure is SAE J 2707 and was described in Section 5.3.1. SEM and EDXS characterizations of the worn surfaces, airborne particulate matter and non-airborne particulate matter were done to correlate the observed behaviors to the respective surface characteristics (Section 6.1.2). The study identified steady states for the frictional, wear, and, in particular, emission behaviors. The frictional stabilization correlated to the stabilization of the extension of the secondary plateaus, whereas the wear and emission stabilization correlated to the achievement of stable composition in the PM and a high degree of compaction of the secondary plateaus. These aspects are important from a testing perspective, as they ensure the representativeness of the following sections in the testing methodology. The considerations concerning the required number of brake stops to attain emission stabilization were taken into account to set proper bedding for the *Reduced Cycle* (Section 5.3.2) and the *Modified AK-Master* (Section 5.3.3)

6.1.1 Evolution of the friction coefficient, wear rate and emissions

During the brake stops the contact pressure and the maximum disc temperature during braking stabilized respectively around 0.6 MPa and 120 °C [92]. Observing the evolution of the friction coefficient with the brake stop number, in Fig. 6.1.2, we can individuate two distinct stages. In the first, from the beginning up to approx. 150 stops, the friction coefficient increases from an initial value of 0.2-0.25 to approx. 0.44. In the second stage, which begins after about 150 stops, the average friction coefficient does not change appreciably in the following brake stops.

Fig. 6.1.3 shows the evolution of the system depth of wear with the brake stops as obtained by the LVDT measurement. The wear increases in an almost linear manner, with an average wear rate of approx. of 0.37 mm per stop. The slope of the curve, which represents the wear rate, is lower at the beginning of the test, i.e., in the first 100-150 stops, and at the end of the test, after approx. 350-400 stops. The specific wear coefficient, K_a , was calculated as a function of the number of brake stops, n , using the 6.1, to obtain a better picture of the wear evolution:

$$K_a(n) = \frac{\Delta d(n)}{p_c(n) s_{slid}(n)} \quad (6.1)$$

where:

- $\Delta d(n)$ is the depth of wear after n-brake stop. It is obtained as a difference between the displacement after n-brake stop and the displacement after the first brake stop;
- $p_c(n)$ is the mean contact pressure during n-brake stop;
- s_{slid} is the cumulative sliding distance up to the n-brake stop.

The evolution of K_a with n is plotted in Fig 6.1.4, where three stages can be distinguished. Herewith, the first stage is called *run-in*. K_a first slowly increases with n, then increases almost linearly up to approx. 150 brake stops. The second stage, indicated with the *transition stage*, displays K_a increasing but with a continuously reduced rate, which tends to a steady-state value after approx. 350 brake stops. Finally, the third stage denoted as the *steady state*, is characterized by a K_a -value in the range of $2 \cdot 10^{-14} \text{ m}^2/\text{N}$ and it is maintained up to the end of the test. Values in this range are typical of the mild wear conditions for friction materials [14].

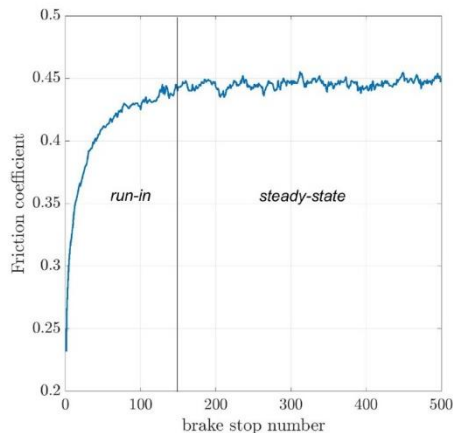


Fig. 6.1.2: Evolution of the friction coefficient with the brake stops.

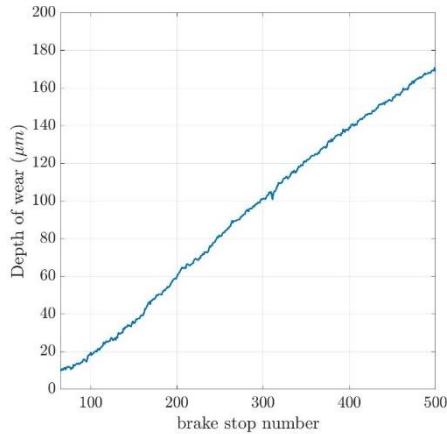


Fig. 6.1.3: Evolution of the depth of wear of the friction material-disc system with the brake stops.

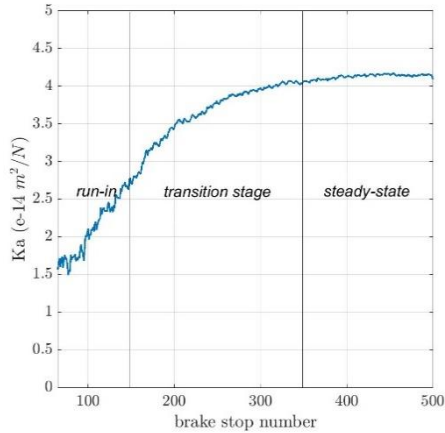


Fig. 6.1.4: Evolution of the specific wear rate, K_a , of the pad-disc system with the brake stops.

Fig. 6.1.5 shows the evolution with time of the total particle concentration during selected brake stops. After reaching a maximum in approx. 6-8 seconds, the emissions decrease. The maximum value of the total concentration of emissions increases the first 150 brake stops, then they decrease approx. up to the 300th brake stop, after which they stabilize for the rest of the test. To better observe this behavior, the mean concentrations per brake stop were calculated and are displayed in Fig. 6.1.6 as a function of the number of brake

stops. Comparing the frictional (Fig. 6.1.2), wear (6.1.4) behavior and emission (6.1.6) behaviors, we can say that, first, the friction coefficient reaches a steady state after 150 brake stops. Whereas the specific wear rate reaches a steady state after 350 brake stops, and therefore a 'transition stage' is present between stop numbers 150 and 350. In the evolution of the specific wear rate, three stages named "run-in", "transition stage", and "steady-state" can be recognized. During the run-in stage, the average concentration of airborne particles increases with the brake stops, up to a maximum value. Between approx. 150 and approx. 350 brake stops, i.e., in the transition stage, the concentration of airborne particles decreases and reaches an equilibrium value of approx. 300 particles/cm³ in the steady state stage.

Finally, the particle size distribution is provided in Fig. 6.1.7. As the concentration changes as a function of the brake stop particle size distribution is expressed as a fraction of the total number concentration (%N/brake) for different brake stops. It is seen that most of the particles have a diameter in the fine size range, of approx. 0.4 μm, in agreement with the published data [14]. Two small peaks pertain to the size range 1-2 μm. From Fig. 6.1.7, the fraction of fine particles with an average size of 0.4 μm increases with the brake stop number. On the contrary, coarse particles, with a size range of 1-2 μm, are observed to decrease slowly but continuously with the brake stop number.

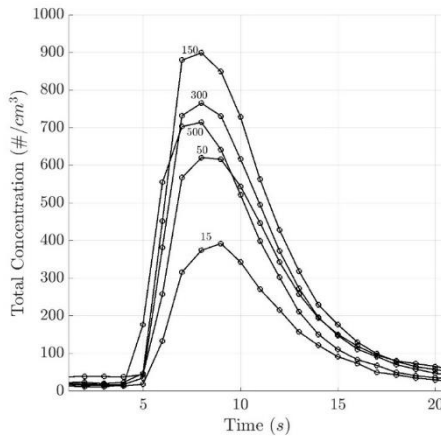


Fig. 6.1.5: Evolution with the time of the total concentration of airborne particles for selected brake stops.

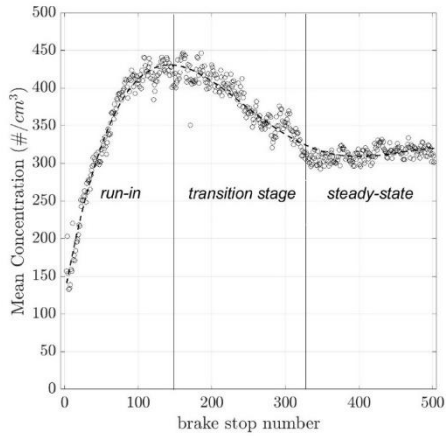


Fig. 6.1.6: Mean concentration of airborne particles per brake stop as a function of the number of stops.

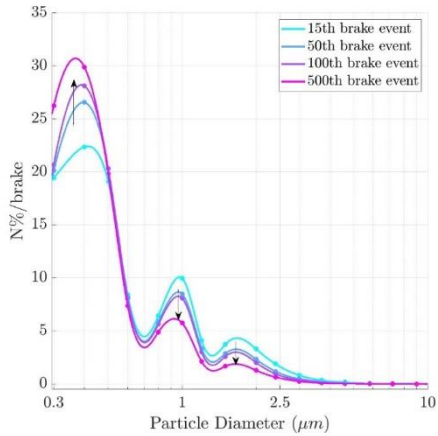


Fig. 6.1.7: Particle size distribution, expressed as number percentage per stop, at different brake stops.

6.1.2 Characterization

6.1.2.1 Worn surfaces

The SEM-EDXS analysis of the worn surfaces aimed at characterizing the degree of compaction and the extension of the secondary plateaus.

Fig. 6.1.8 displays the SEM observations of the worn surfaces of the friction material after the warm-up stage (a), during the run-in (b), transition (c), and steady state (d) stages. In Fig. 6.1.10, SEM observations at higher magnification of the worn surface of the friction material are provided at the same stages. Fig 6.1.10 shows observations by electron backscattering (BS) mode on the left, which provides information on the elemental composition (heavier elements are brighter), and by secondary electron (SE) mode for a better topography inspection. As mentioned in section 2.1, the primary plateaus are the plastically deformed steel fibers, they are the structures white in the observations. Whereas, the secondary plateaus appear grey as they are mainly composed of wear fragments, mainly iron oxide being, progressively compacted. This was confirmed by EDXS point analysis (Table 6.1.1 and Fig.6.1.11).

Regarding the extension of the secondary plateau, passing from observations a to c of Fig. 6.1.8, their extension is observed to increase. To better understand the evolution of their extension with the brake stops, the coverage factor was obtained as explained in the procedure [93]. The coverage factor is an indicator of the surface in contact, it was calculated as the percentage of secondary plateaus with respect to the total area. The coverage factor is plotted in Fig. 6.1.9. It increases markedly in passing from the warm-up stage to the transition stage, whereas, from this stage, it remains rather constant.

Regarding the degree of compaction, the high magnification observations (Fig. 6.10). In the case of run-in (Fig. 6.1.10-a), the secondary plateaus do not seem to be well-formed, presenting only small compacted regions. Instead, in the transition stage, the formation of secondary plateaus is evident, featuring much more compacted regions (Fig. 6.1.10-b). This aspect is even more marked in the friction layers at the steady state (Fig. 6.1.10-c).

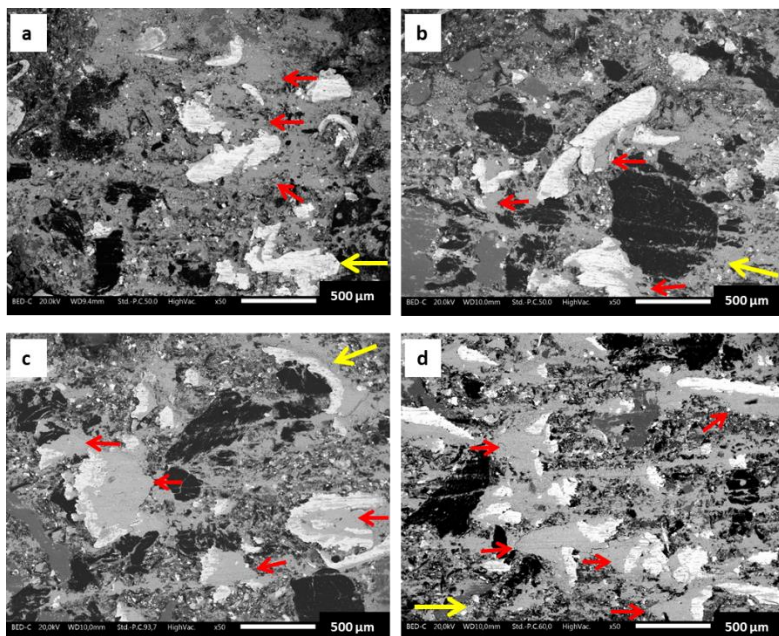


Fig. 6.1.8: Low magnification backscattered SEM observations of the worn surfaces of the friction material after (a) warm-up, (b) run-in stage, (c) transition stage, and (d) at steady state. The yellow arrows indicate the sliding direction.

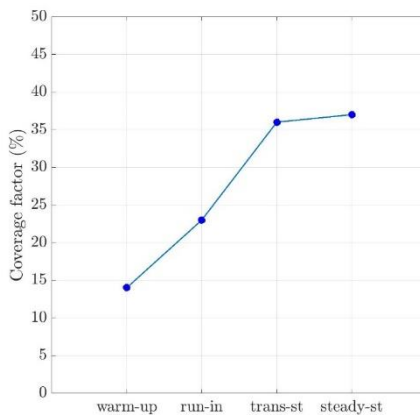


Fig. 6.1.9: Coverage factor at the different stages of bedding.

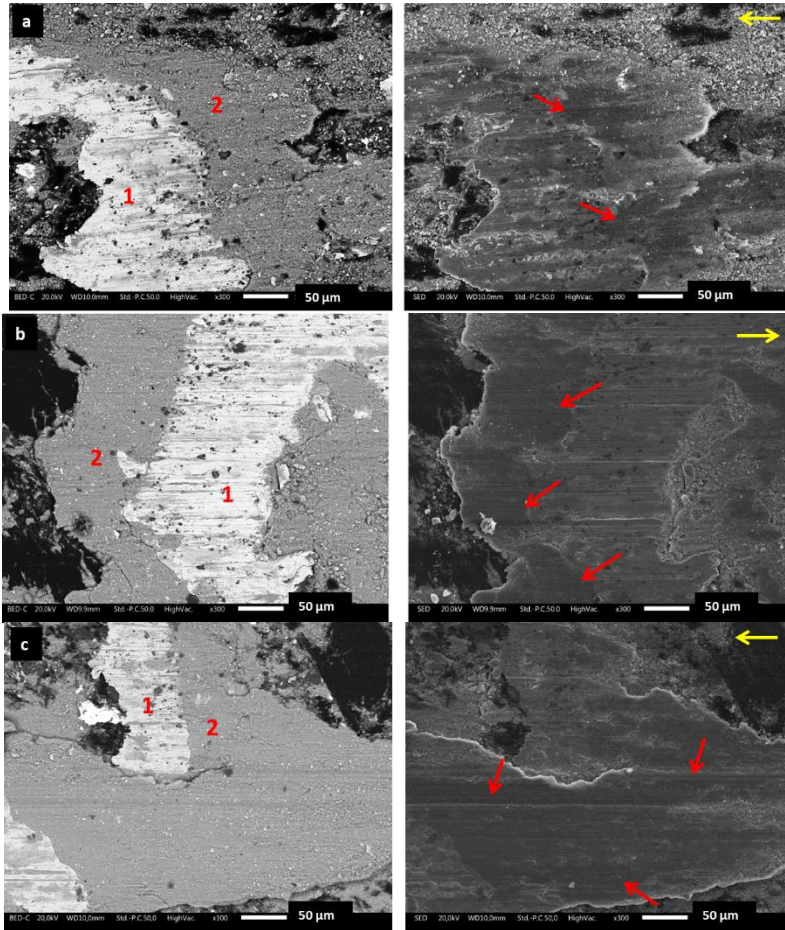


Fig. 6.1.10: SEM micrographs of the worn surface of the friction material during the (a) run-in stage, (b) in the transition stage, and (c) at steady state. On the left: backscattered electrons images, showing the primary (1) and secondary (2) plateaus. On the right are secondary electron observations, in which the red arrows highlight some more compacted regions of the secondary plateaus. The yellow arrows indicate the sliding direction.

Further information on the characteristics of the secondary plateaus and their compactness was obtained through a point EDXS analysis of their composition. Table 6.1.1 and Fig. 6.1.11 show the obtained elemental composition after the warm-up, the run-in stage, the transition stage and the steady state. The EDXS analysis (Table 6.1.2) confirms that the plateaus contain the same elements as the virgin materials (Table 6.1.1), but in different

concentrations. The detected high concentration of iron indicates the contribution from the counterface disc wear. In addition, the iron content increases with the brake stop number. On the other hand, it is interesting that the oxygen content does not change with the brake stop number, featuring a value of approx. 26 %. On this aspect, we should notice that when the content of the pad ingredients having oxygen, such as alumina, magnesium oxide, and chromite, increase or decrease in the secondary plateaus, also the oxygen content should respectively increase or decrease. Thus, as the iron content increase, the constant nature of oxygen with the brake stop number must be attributed to the pick up of some oxygen from the surrounding environment, that interacts with iron forming Fe-oxides. This is the typical process of tribo-oxidative wear of ferrous alloys [48]. The actual fraction of iron and iron oxides in the secondary plateaus was not determined, however, these considerations allow us to safely conclude that the fraction of iron and Fe-oxides in the plateaus increased with the brake stops, i.e., in passing from the stages between the warm-up stage and the steady state stage.

Finally, to have a complete picture of worn surfaces, including the mechanisms acting at the counterface of the friction material, Fig. 6.1.12 shows the worn cast-iron disc surfaces after the run-in stage (a) and in the steady state stage (b). The worn surface after the run-in stage displays scratches oriented in the sliding direction typical of abrasive wear. Part of the scratches can also be ascribed to the machining process of the disc. However, in the steady state stage, the disc surface does not present such abrasive scratches, instead, extensive surface plastic deformations are present on the disc surface.

Table 6.1.1: Elemental composition of the secondary plateaus after the warm-up, run-in, and transition stage at steady state. The carbon content was not considered.

Element (wt.%)	Warm-up	Run-in stage	Transition stage	steady state
Fe	48.2 ± 1.0	53.2 ± 2.2	59.2 ± 0.9	61.9 ± 1.3
O	25.9 ± 2.6	27.3 ± 0.6	25.5 ± 0.6	27.6 ± 1.0
Zn	4.7 ± 1.2	4.4 ± 1.2	3.4 ± 0.1	2.2 ± 0.9
Mg	3.8 ± 1.1	3.4 ± 0.8	2.5 ± 0.4	1.6 ± 0.4
Si	2.6 ± 0.5	2.0 ± 0.1	2.0 ± 0.1	1.3 ± 0.3
Sn	3.6 ± 1.6	2.7 ± 0.6	2.1 ± 0.1	1.7 ± 0.6
Al	6.1 ± 2.8	2.5 ± 0.5	2.1 ± 0.2	1.7 ± 0.7
S	2.7 ± 0.9	2.4 ± 0.4	1.8 ± 0.2	1.2 ± 0.4
Ca	1.3 ± 0.8	1.4 ± 0.3	0.5 ± 0.1	0.4 ± 0.2
Cr	0.9 ± 0.0	0.7 ± 0.1	0.6 ± 0.1	0.6 ± 0.1

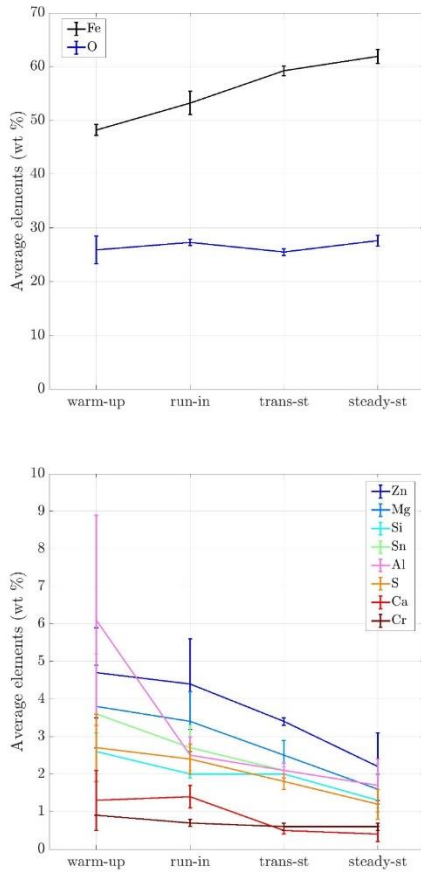


Fig. 6.1.11: Elemental composition of the secondary plateaus after the warm-up, run-in, and transition stage (trans-st) at steady state (steady-st). The carbon content is not considered.

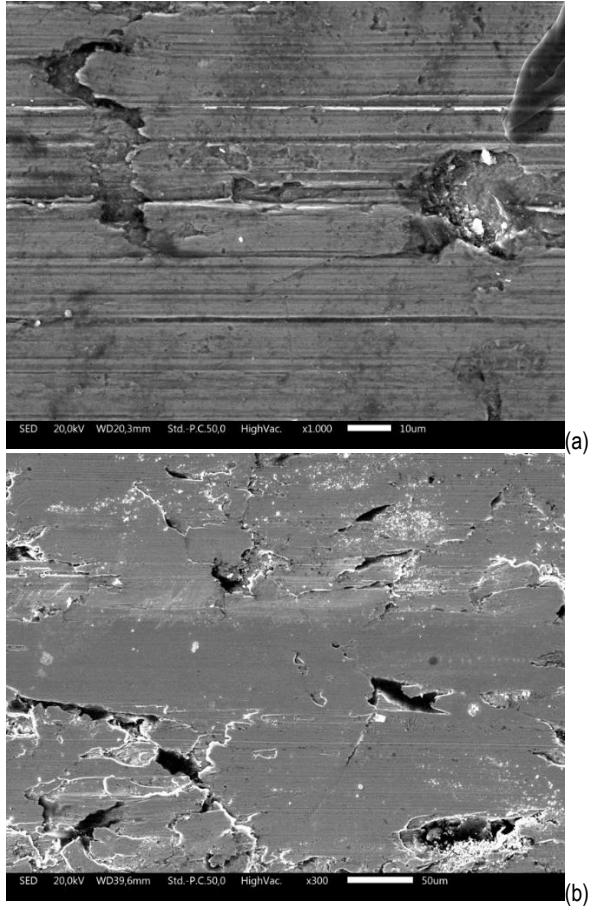


Fig. 6.1.12: SEM micrographs of the worn-out surface of the cast iron disc in the (a) run-in stage and in the (b) steady state stage.

6.1.2.2 Airborne particles

As mentioned, during the tests PM was collected with the impactor. Fig. 6.1.13 shows the SEM observations of airborne particulate emissions in the size range of 10 – 2.5 μm for the identified stages: the run-in stage (a), the transient stage (b), and at the steady state (c). Some particles have flake-shaped particles of a size up to approx. 5 μm , nearly equiaxed, other particles are irregular in shape and much smaller in size.

The composition of the airborne particles in the size range 2.5–1 μm was obtained by full-frame EDXS elemental composition (Table 6.1.2 and Fig. 6.1.14). By comparing Table 6.1.2 and Fig. 6.1.14 with Table 6.1.1 and Fig. 6.1.11, the particle composition appears very similar to the composition of the secondary plateaus (comparing). This result is in agreement with [94], confirming that the emitted particles originate mainly from the disruption of the secondary plateaus. In addition, no marked differences were detected from the same analysis of the airborne particles in the size range 2.5–1 μm , therefore these results are not reported.

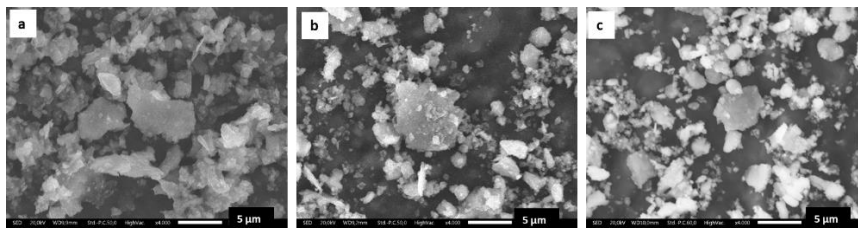


Fig. 6.1.13. SEM micrographs of the airborne particles with an aerodynamic diameter in the range 10–2.5 μm were collected during the (a) run-in, (b) transient stage, and at (c) steady state.

Table 6.1.2: Elemental composition of the airborne particles size range 2.5–1 μm collected during the run-in stage, in the transient stage, and at steady state. The carbon content was not considered.

Element (wt.%)	Run-in stage	Transient stage	At steady state
Fe	55.6 \pm 0.8	62.7 \pm 2.2	62.8 \pm 2.0
O	23.5 \pm 2.3	25.9 \pm 2.5	24.4 \pm 2.2
Zn	3.7 \pm 0.8	2.6 \pm 0.0	2.5 \pm 0.1
Mg	4.1 \pm 0.1	2.3 \pm 0.1	2.3 \pm 0.0
Si	1.5 \pm 0.1	1.4 \pm 0.0	1.6 \pm 0.1
Sn	3.5 \pm 0.6	2.0 \pm 0.1	2.1 \pm 0.2
Al	3.0 \pm 0.3	1.9 \pm 0.1	1.9 \pm 0.0
S	2.3 \pm 0.3	1.9 \pm 0.2	1.0 \pm 0.7
Ca	2.3 \pm 0.1	0.7 \pm 0.2	1.7 \pm 0.9
Cr	0.7 \pm 0.2	0.5 \pm 0.0	0.5 \pm 0.0

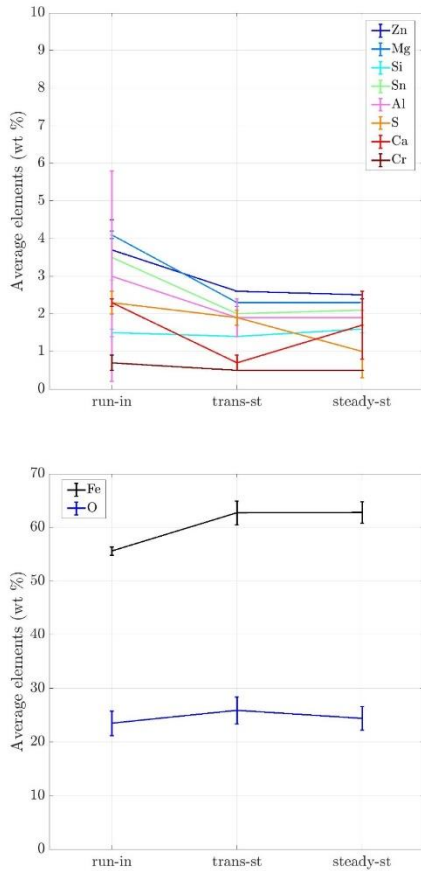


Fig. 6.1.14: Elemental composition of the airborne particles collected during the run-in stage in the transient stage (trans-st) and at steady state (steady-st). The carbon content was not considered.

6.1.2.3 Non-airborne particles

Non-airborne particles are also produced during the tests. They were collected on Aluminum foils placed on the floor of the dynamometer chambers. Fig.6.1.15 shows these typical particles of a flake-like morphology of a size range between 20 and 10 μm . Marks “1” and “2” in the picture indicate the areas analyzed with the EDXS. The elemental composition by EDXS is shown in Table 6.1.3, it is very similar to the composition of the secondary plateaus (see Table 6.1.1), confirming that these particles are large fragments of friction layer removed during braking.

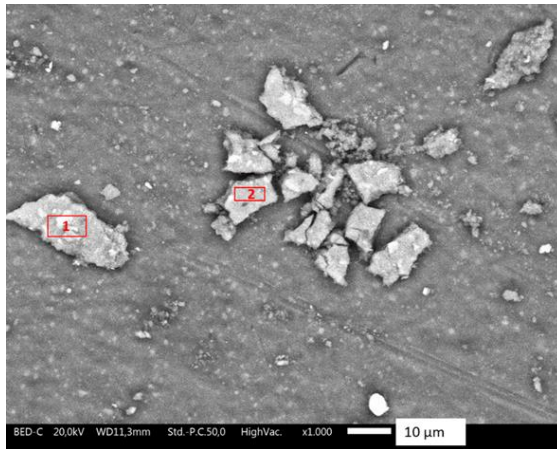


Fig 6.1.15: SEM image of non-airborne particles collected during the whole test.

Table 6.1.3: EDXS elemental composition of the non-airborne particles shown in Fig. 6.1.14. The carbon content was not considered.

Element (wt.%)	Area 1	Area 2
Fe	59.30	59.38
O	26.53	25.06
Zn	2.66	2.23
Mg	2.18	2.33
Si	1.38	1.30
Sn	2.08	2.28
Al	3.07	4.90
S	1.61	1.50
Cr	0.61	0.58
Mn	0.58	0.43

6.1.3 Main wear mechanisms

In this section, the evolution during the bedding process of the frictional, wear and emission behaviors, and relative steady state regimes, will be interpreted as the friction layer attains surface stabilization in terms of extension, degree of compaction and composition.

The frictional behavior is the first to achieve stable conditions. The coefficient increases during the first 150 brake stops (Fig. 6.1.2), the run-in stage, from a value of 0.2 to a steady state value of 0.45. This value is typical for the type of materials [95]. The increase in the friction coefficient is ascribable to the formation of the friction layer [57]. The two main structures of the friction layer are the primary and secondary plateaus. As already mentioned, the primary plateaus are heavily plastically deformed steel fibers, against which wear fragments, from the pad and, especially, from the disc, compact forming the secondary plateaus. Since large plastic deformations are involved, the iron fragments are small in size and very defective at the surface [9], thus favoring the oxidation of the particles [48]. The analysis of the secondary plateaus on the coverage factor (Fig. 6.1.9) and compositional analysis (Fig.6.1.11) suggest that the stabilization of the friction layer in terms of iron content and extension determines the establishment of a steady state for frictional behavior. The extension of the secondary plateaus is strictly related to the area of contact, whereas the composition contributes to the tangential shear that the surface can exert. Both factors are paramount in the determination of the tangential force, and therefore the friction coefficient [95][96].

Regarding the wear behavior during the bedding process, the wear conditions are typical of mild wear, with K_a in the range of $4 \cdot 10^{-14} \text{ m}^2/\text{N}$ and a relatively low temperature as the maximum disc temperature was approx. $120 \text{ }^\circ\text{C}$. In these conditions wear is a result of the dynamic formation and disruption of the secondary plateaus. However, at the beginning of sliding, during the run-in of approx. the 50 brake stops (Fig. 6.1.4), the wear rate is low and slowly increases. This behavior is probably due to the high amount of wear fragments remaining entrapped at the surface to form the secondary plateaus.

Once the particle and fragments leave the tribological system in the mentioned dynamic process, the particle emissions increase accordingly with the increase of the wear rate. Of course, the wear and emission behaviors are strongly interrelated. During the run-in, they depend on the increase of the contact area of contact due to the formation of the friction layer. At the end of the run-in stage, although wear continues to increase, the emissions start decreasing (Fig. 6.1.6), and we are at the transition stage. Observing Fig. 6.1.10 high magnification SEM observations, we can explain this phenomenon in terms of variation in the degree of compaction of the secondary plateaus. The degree of compaction appears rather low in the run-in stage increasing in the transition and steady-state stages.

The observed friction layer has typical characteristics of the friction layers that form during the tribo-oxidative wear of ferrous alloys [1]. Such friction layers were first described by Stott [48] and the main concepts were explained in Section 3.5. In prolonged dry sliding, the agglomerated iron oxides tend to progressively sinter together to form very compacted and smooth layers, denoted as 'glazes'. They increase the wear resistance and favor the

formation of large flake-like fragments. In broad agreement with this, are the observations of non-airborne particles that were collected at the end of the test in Fig. 6.1.15. the fact that the wear rate is higher in the steady state than in the run-in and that the emission decrease in the steady state supports that a higher percentage of the fragments leave the tribological system, without being detected, thus, as non-airborne particles.

Compaction is rather a sintering process, thus it is more intense when particles of the same composition are in contact [97], such as in the case of iron oxides in tribo-oxidative wear. The stabilization in the degree of compaction of the secondary plateaus is well-correlated to the compositional stabilization of the iron oxide content in the secondary plateaus (Fig. 6.1.11). The glazes are the results of repeated contact stresses in the agglomerated particles and cumulative wear of the cast iron counterface with the increase in the number of brake stops during the test. favoring the formation of the glazes. Finally, the formation of these structures is responsible for the stabilization of the wear rate and the drop in the particle emissions during the transient stage and shift to a wear mechanism that favors the detachment of large flake-like fragments.

6.2 Influence of contact pressure and velocity on the brake behavior and fine particulate matter emissions of a low-met and NAO friction material

As mentioned in Section 4.2, the frictional, wear and emission behaviors are strictly related to the friction layer that develops at the disc-pad interfaces. The characteristics of the friction layer are determined by the combinations of the friction material formulations and the braking parameters.

In this study, the influence of pressure and velocity on the frictional, wear and emission behaviors of the reference low-met and NAO materials is investigated (Section 6.2.3). The adopted braking cycle was the *Reduced Cycle* (see Section 5.3.2). In the braking cycle, to reduce the *history effects* and restore the surface conditions, *reference blocks* were interposed after each *pv-block*. Cumulative distribution functions were used to provide information on the variability of the friction coefficient and emission during the steady state of the bedding and the *reference blocks* (Section 6.2.2). In Section 6.2.3, the frictional, wear and emission behaviors are described as a function of pressure and velocity. The NAO material displayed a higher friction coefficient, lower wear and emission than the low-met material. The characterization of the worn surfaces after tests at specific *pv* conditions is presented in Section 6.2.4. The characterization was done to relate surface characteristics to the observed behaviors. Finally, as discussed in Section 6.2.5, the differences in the observed behaviors between the low-met and NAO friction materials are based on the different natures of the friction layers. The NAO material is characterized by a uniform and more extended friction layer. The applied methodology identified specific wear mechanisms for the two types of materials.

6.2.1 Bedding

Fig. 6.2.1 displays emissions as mean concentrations during the 250 brake stop of the bedding procedure for the low-met and the NAO material under study. The emissions increase during the initial part of the procedure until they reach a steady state. The steady state conditions are reached approx. after 100 and 200 brake stops respectively for the low-met and the NAO materials. The NAO material features lower emissions a lower peak of emissions and the steady state is achieved later than the low-met material. Figure 6.2.2 shows the cumulative distribution functions of the emissions associated with the emission peak (15-75 brake stops) and the steady state conditions (200-250 stops). They give along the y-axis the probability of having equal or lower emissions at the corresponding x-value. In the steady state, the emissions are lower both in terms of mean value and scatter (the slope of the curve).

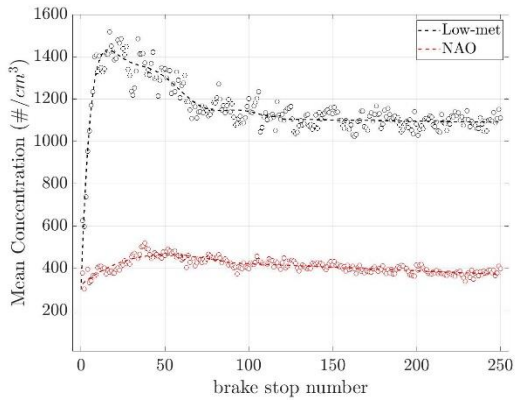


Figure 6.2.1: Mean concentration of airborne particles per brake stop as a function of the number of stops during the bedding procedure.

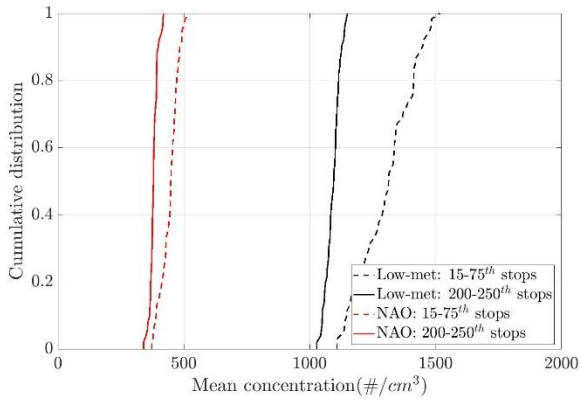


Fig. 6.2.2: Cumulative distribution function of the mean PM concentration at the beginning and the steady state of bedding for the low-met and NAO material (see figure legend).

6.2.2 Reference Blocks

As mentioned in Section 5.3.2, the reference blocks were carried out after each p-v block to pristine the surface conditions. Fig.6.2.3 and Fig.6.2.3 display the cumulative distribution functions of the average friction coefficient and the average emissions at the first brake stops and the last two stops of all the reference blocks. For comparison, in the distributions are included the values associated with steady conditions of the bedding.

By comparing the first and the last brake stops of the reference blocks for both the low-met and the NAO materials and low-met materials, the friction coefficient tends to steady-state conditions. Some differences are clear between the two materials. The NAO material has a friction coefficient that is lower than in the steady state and increases with the brake stop number during the reference blocks. On the other hand, for the low-met material, the friction coefficient can be both higher and lower during the reference block as compared to the steady-state conditions. Regarding the general variability, the scatter associated with the reference blocks is higher than that for the steady state of bedding.

Regarding the variability of the emissions, the scatter during the reference blocks is higher than the scatter recorded during the steady state of bedding. Moreover, the scatter changes during the reference block. In passing from the beginning to the end of the block, the scatter decreases by a factor of 5 to 3 for the low-met material and by a factor of 3 to 2 for the NAO material. This is an indication that the mating surfaces are progressively adapting to new braking parameters. Comparing the scatter of the two materials, it is clear that the NAO material displayed a lower variability in the reference blocks.

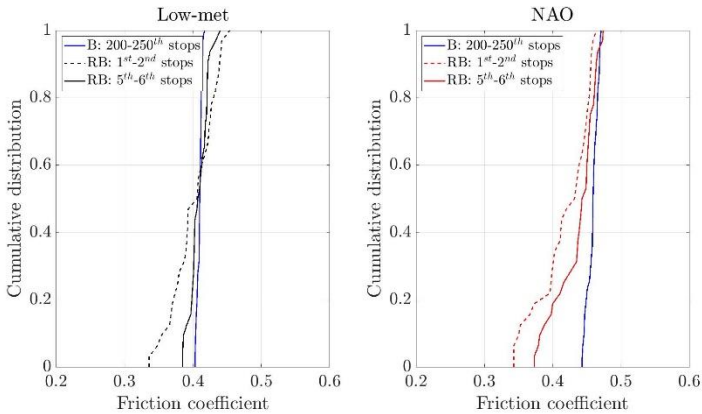


Fig.6.2.3: cumulative distribution function of friction coefficient distribution at the steady state and for the reference stops in during the 1st and 2nd and the 5th and 6th brake stops.

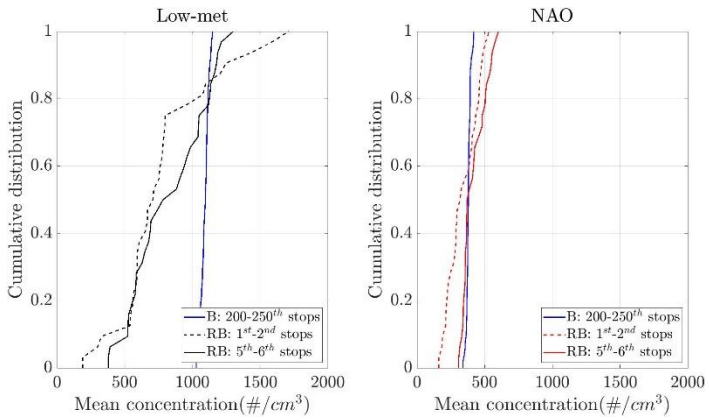


Fig.6.2.4: cumulative distribution function of the mean concentration at the steady state (B) and for the reference stops (RB) during the 1st and 2nd and the 5th and 6th brake stops.

6.2.3 pv-blocks

6.2.3.1 Contact temperature

The contact temperature is a factor that is usually considered in tribological processes. The disc temperature increases during braking. In Fig.6.2.5, the maximum disc temperatures are displayed as maps for the two friction materials. For the tested braking parameters, the temperatures increase with the contact pressure and, especially, initial sliding velocity. The NAO material displayed higher disc temperatures because of the slightly higher friction coefficient and, especially, the lower thermal conductivity as the metal content is much lower than in the low-met material.

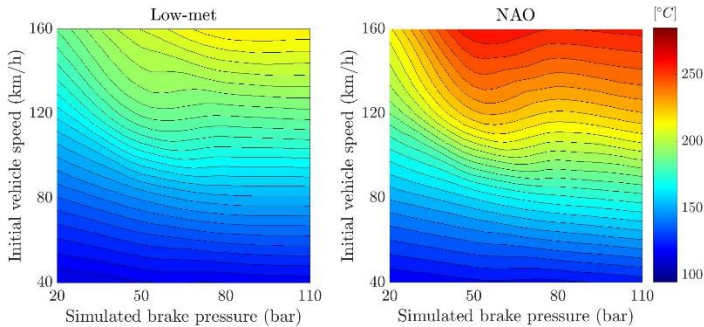


Fig. 6.2.5: Map of maximum disc temperature.

6.2.3.2 Friction coefficient

The values of the friction coefficient are depicted in Fig 6.2.6 for the 10 repeated brake stops at 110 bar of system pressure and three different velocities: 40, 80 and 160 km/h. Different behaviors are observed for both materials at different velocities. The friction coefficients increase and decrease with the brake stop number respectively at low (40 km/h) and high (160 km/h). Whereas at 80 km/h, the behavior is intermediate, the friction coefficient is rather almost constant for the low-met material, and it shows a slight increase for the NAO material.

To map the frictional behavior, the average friction coefficients to the last three stops were chosen as representative values for each p-v condition as their display lower variability and are plotted in Fig. 6.2.7. The friction coefficient is higher at the low velocity (40 km/h) and pressure (20 bar), being rather stable at the other tested velocities and pressures. Interestingly, the NAO material features, on average, a higher friction coefficient.

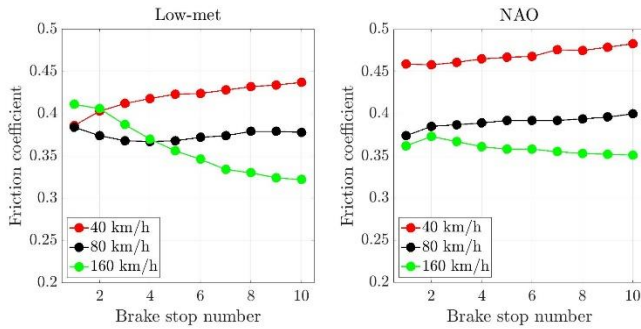


Fig.6.2.6 Evolution of the average friction coefficient of the Low-met and NAO friction materials over the 10 brake stops of the p-v blocks at 40, 80 and 160 km/h of initial speed and 110 bar pressure.

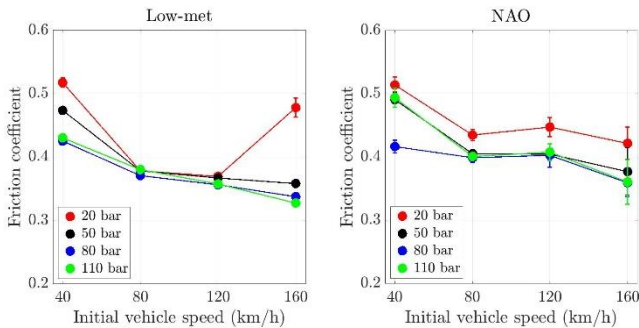


Fig. 6.2.7 Friction coefficient as a function of initial vehicle speed at different simulated brake pressure for the two wear systems.

6.2.3.3 Wear rate

The wear rate can be described by the depth of wear expressed as system wear (pad + wear), as explained in Section 5.1.2. The evolution of the depth of wear is displayed in Fig. 6.2.8. Then, the depth of wear/brake stop is obtained by dividing the depth of wear by 10, the number of brake stop per pv-block. These values are reported in Fig. 6.2.9. The wear rate is low and not much affected by pressure and velocity at low velocity (40 km/h), while at high velocity (120 and 160 km/h) the wear rate is much more influenced by both pressure and velocity. The values of mass losses of the disc and friction materials related to the entire

braking cycle are shown in Table 6.2.1. The cumulative wear of NAO material was lower than the low-met material.

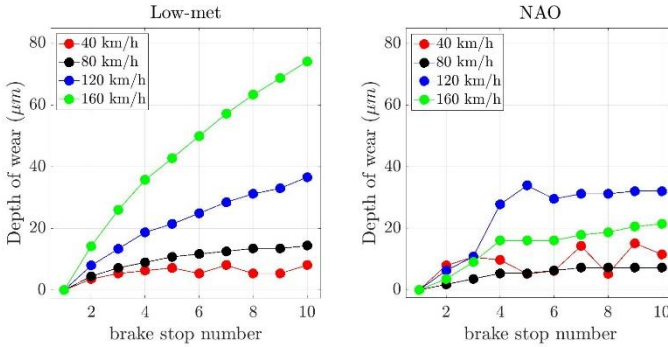


Fig. 6.2.8: Evolution of the displacement with respect to the first brake stop for the blocks measured in the low-met and NAO friction materials, tested at 40, 80, 120 and 160 km/h of initial velocity and 110 bar pressure.

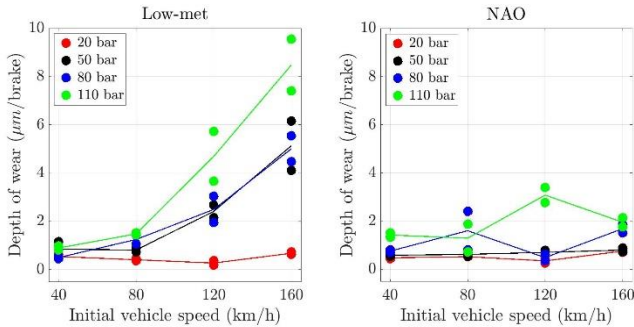


Fig. 6.2.9: Wear rate as depth of wear as a function of initial vehicle speed at different simulated brake pressures measured in the low-met and NAO friction materials.

Table 6.2.1: mass loss of the disc and the pad after the test.

Mass loss (g)	Low-met	NAO
Disc	0.59 ±0.00	0.11 ±0.00
Pad	0.42 ±0.02	0.22 ±0.02

6.2.3.4 Emissions

Fig. 6.2.10 shows the total particle concentration during the brake stops respectively at 50 bar at 80 km/h and 160 km/h for the low-met and NAO materials. As described in Section 6.3.1, the total particle concentrations increase up to a peak at approx. 7 s, then they decrease to the background level in approx. 20 s. From these signals, the mean values were obtained and plotted in Fig. 6.2.11, for consecutive brake stops at 40 and 160 km/h of initial velocity and 110 bar of simulated brake pressure.

The emissions showed different stability in repeated brake stops according to the velocity. The behavior was rather stable in the 10 consecutive brake events at low and intermediate velocities (40 and 80 km/h). On the other hand, at high velocities (120 and 160 km/h), the emissions decreased with the brake stops. This decrease is more marked for the low-met material. From the first brake stop to the last brake stops of a pv-block at high velocity, the emissions can decrease by 25-35 %. Because of this high variability at high velocity in the first brake stops, the average of the last three values was chosen as representative to map the emissions. The same choice was applied to the friction coefficient in Section 6.2.3.2.

The emissions are plotted in Fig. 6.2.12 The initial velocity has a markedly higher influence than the pressure on the emissions. The emissions at high velocities are three orders of magnitude higher than those at the lowest velocities.

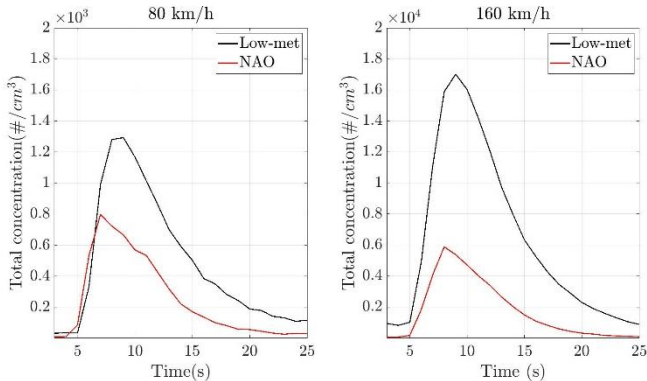


Fig. 6.2.10: Total concentration for the 10 brake stops at 80 km/h and 160 km/h and 50 bar for couplings involving the low-met and NAO materials.

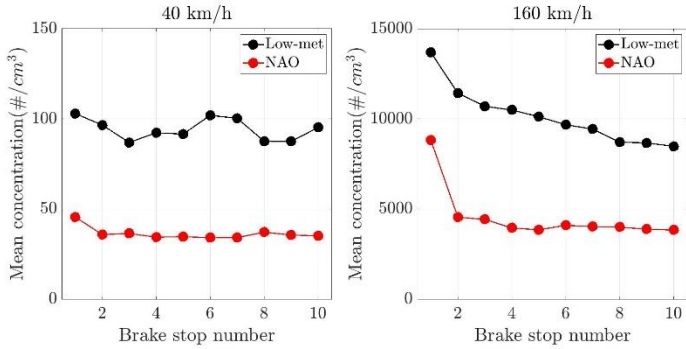


Fig. 6.2.11: Mean particle concentration for consecutive brake stops with an applied pressure of 110 bar starting from an initial speed of 40 km/h (a) and 160 km/h (b) for couplings involving the low-met and NAO friction materials.

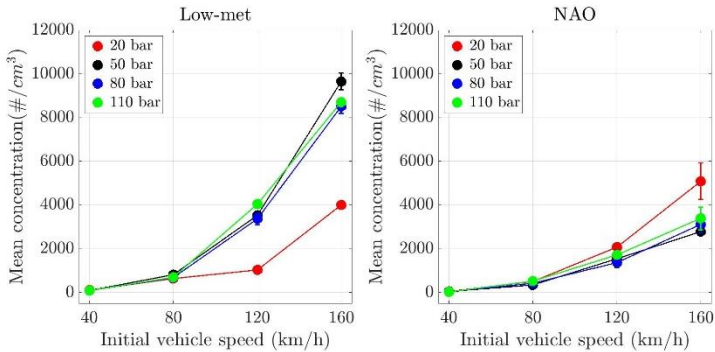


Fig. 6.2.12: Mean particle concentration ($\#/cm^3$ /brake stop) as a function of initial vehicle speed for different simulated brake pressures, as indicated in the plot legends.

6.2.4 Characterization of the worn surfaces

The analysis of the worn surfaces aimed to understand how the different conditions of pressure and velocity modified the characteristics of the friction layers with respect to the conditions attained after bedding (Fig.6.2.13) regarding the frictional behavior, reference is made to Fig. 6.2.6: the friction coefficient increases at the low velocity and decreases at the high velocity. For this reason, the analysis was restricted to the p-v conditions of 40 km/h 160 km/h at 110 bar. New specimens were used for these tests, which consisted of the bedding procedure and the specific p-v condition. Plus, for the high-velocity condition, an additional test of one-stop only was done.

The worn surface of the NAO after bedding and the low-met materials are depicted in Fig. 6.2.13 as BSE micrographs. As mentioned in Section 6.3.2.1., primary and secondary plateaus can be distinguished on the friction layer of the low-met material. The surface of the NAO material is characterized by a uniform and spread friction layer since no hard constituents are present to act as primary plateaus. As mentioned in 6.3.2.1, the coverage factor can be used as an indicator of the extension of the area of contact during sliding. In agreement with the more spread friction layer, the coverage factors after bedding conditions resulted in approx. 40 % and 55% of the total surface respectively for the low-met and the NAO materials. Regarding the composition of the worn surfaces, EDXS analysis in Fig. 6.2.14 reveals that the low-met material had a higher iron content of the secondary plateaus approx.. 65 wt.%, higher than the NA of approx. 35 wt.%.

Fig. 6.2.15 shows BSE micrographs of the worn surfaces after the pv-block at low and high velocities (10 brake stops at 110 bar and 40 and 160 km/h respectively). Fig. 6.2.16 depicts high magnification BSE observations of the worn surfaces of the two materials after the first and the tenth stops at high velocity.

Regarding the friction layer of the low-met materials, after the low-velocity test, the worn surface of the low-met materials is characterized by well compacted and uniform friction layer. the secondary plateaus display a good degree of compaction. On the other hand, observing Fig. 6.2.16, at high velocity after the first brake stop, the secondary plateaus look extended but less compacted, but after 10 brake stops the secondary plateaus are scarce, meaning that the severe braking conditions damaged the friction layer. The coverage factor (Fig. 6.2.16) confirms the higher extension of secondary plateaus, more than 50 %, found after the 1st brake stop than the extension after the 10th brake stops at the same braking conditions. Although the coverage factor at the 10th stop, at different velocities, increases with the velocity, it is important to notice they display reduced compaction of the secondary plateaus.

The NAO material exhibited a different picture with respect to the low-met material. Regarding the extension of the friction layer, the NAO material did not exhibit significant variation between low and high velocities (Fig. 6.2.17). Whereas, the friction layer appeared significantly more compacted after the test at high velocity.

Regarding the compositional analysis (Fig. 6.2.18), they confirmed that the NAO materials displayed a friction layer of a lower content of iron oxide than the secondary plateaus of the low-met material for each test condition.

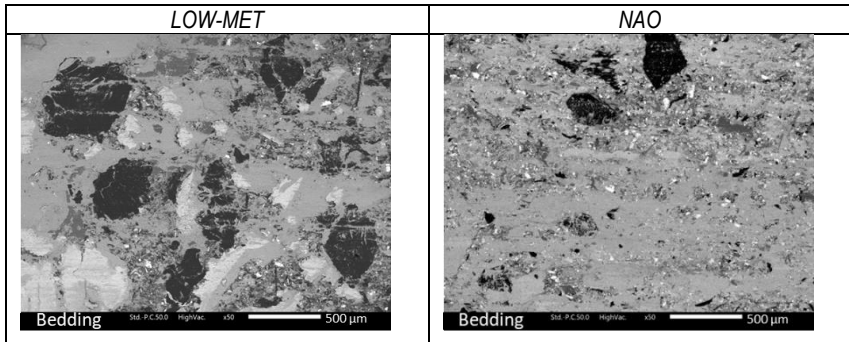


Fig. 6.2.13: Backscattered electrons micrographs of the low-met and NAO materials' surfaces after the bedding procedure.

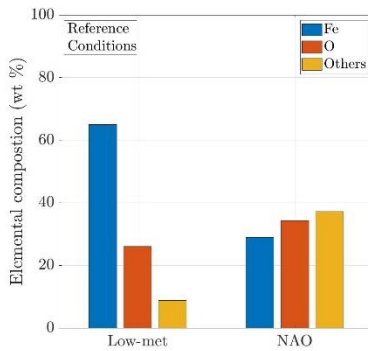


Fig. 6.2.14: Elemental composition of the friction layers forming on the low-met and NAO material at the reference conditions (after the bedding procedure). Reference to Fe and O and other elements.

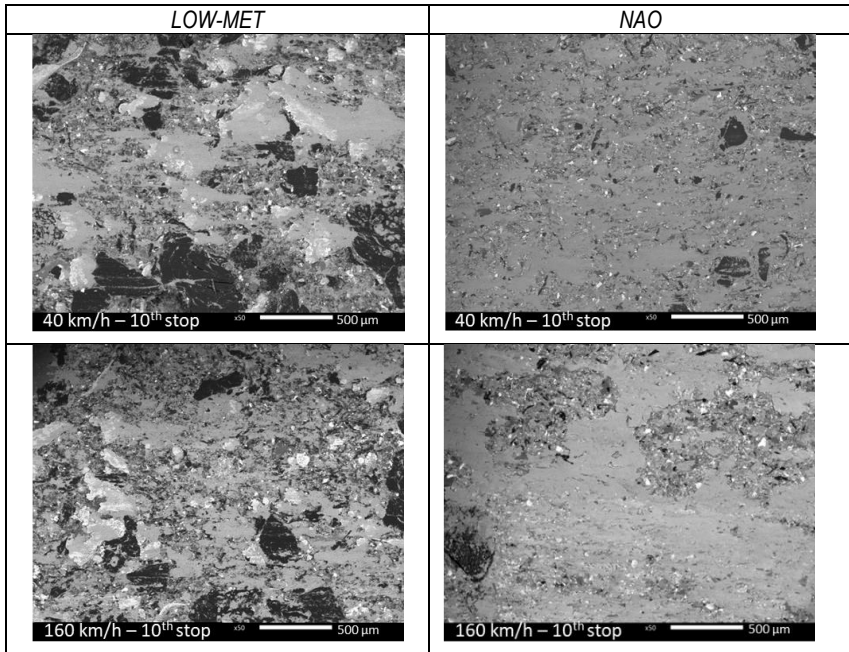


Fig. 6.2.15: Backscattered electrons micrographs of the low-met and NAO materials' surfaces after respectively 10 brake stops at 40 km/h and 160 km/h and 110 bar

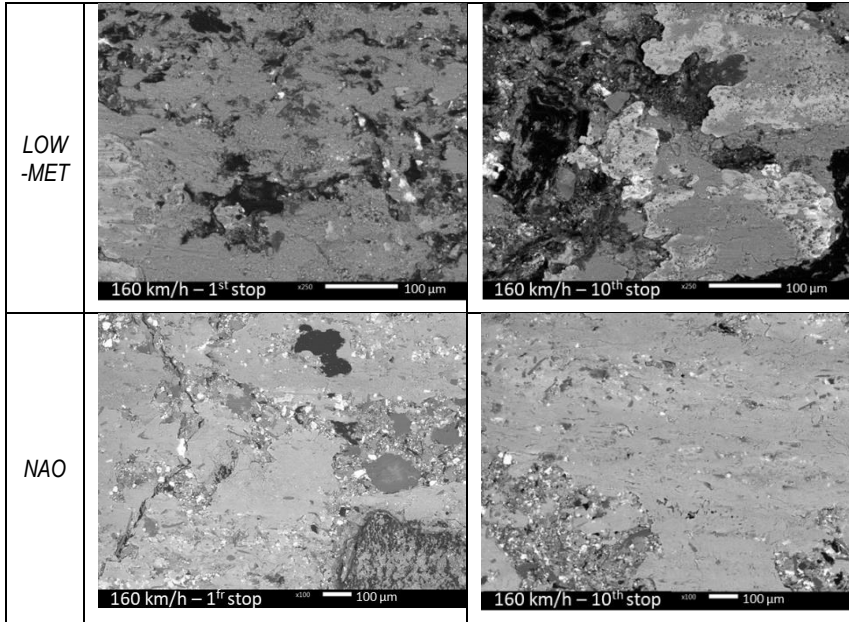


Fig. 6.2.16: Backscattered electrons micrographs at high magnification of the low-met and NAO worn surfaces after 1 (left) and 10 (right) brake stops at 160 km/h 110 bar.

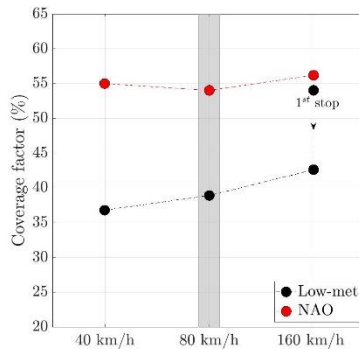


Fig. 6.2.17: Coverage factor of the friction material samples after the block at 40 km/h, the bedding (the grey strip), whose initial velocity is 80 km/h, and the block at 160 km/h. The unstable condition of the surface of the low-met material at the 1st brake stop at 160 km/h is also depicted (1st stop).

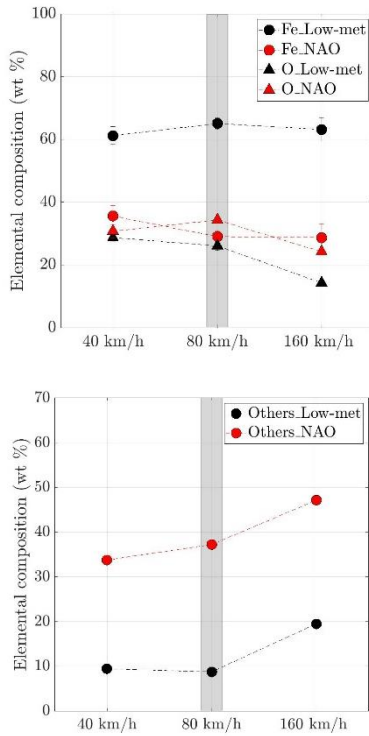


Fig. 6.2.18. Elemental composition of the secondary plateaus for the low-met and the NAO material after the block at 40 km/h, the bedding (the grey strip), whose initial velocity is 80 km/h, and the block at 160 km/h. Reference to Fe and O (top) and other elements (bottom)

6.2.5 Main wear mechanisms

This section describes the development of a testing methodology to assess the frictional, wear and emission behaviors of brake materials. The braking cycle was designed to allow the identification of relevant wear mechanisms. This section is dedicated to, first, recalling briefly the design of the brake cycle and, second, understanding the relationships between the braking condition and wear mechanisms. The study is focused on highlighting the differences between a low-met and a NAO friction material, which are the two most common types of friction materials.

The brake cycle, called *Reduced Cycle*, consisted of three parts: bedding, pv-blocks and reference blocks. The pv-blocks were used to map the frictional, wear and emission behaviors as a function of pressure and velocity. The methodology proposed two solutions to reduce the transitional effects induced by the various braking parameters in the pv-blocks. First, the p-v blocks were randomized. Second, reference blocks, featuring mild braking conditions, were conducted after each the pv-block to pristine to the same surface conditions, before the following pv-block. To discuss the stability of the friction and emission behaviors at reference and after different braking conditions, cumulative distribution functions were used. Fig. 6.2.3 and 6.2.4 show that during the reference blocks, the friction coefficient and the emissions reduce their variability tending to values typical of the steady state. For a correct and reproducible evaluation of the different brake parameters, the initial conditions of each p-v block should be ideally identical. In this regard, the cumulative distribution functions are a useful tool to qualify the general conditions during the braking cycle. The variability of the emissions at the end of the reference blocks is relatively low, whereas, as concerns the friction coefficient, the number of brake stops in the reference cycle was adequate.

Regarding the frictional behavior in the pv-blocks, a slight increase at low velocity and a decrease at higher velocity were observed during the repeated brake stops (Fig. 6.2.6). This behavior was more marked for the low-met than the NAO material. At the end of each p-v block (Fig. 6.2.7), for both materials, the friction coefficient decreased with pressure and velocity. The decrease of the friction coefficient with velocity and pressure is a general phenomenon, already observed in [21][61].

The friction coefficient is less sensitive to different pressure and velocity for the NAO than for the low-met material. The more uniform extension and compaction of the friction layer of the NAO material provided higher stability (Fig 6.2.15 and 6.2.17) This is in agreement with the dependence of adhesion on the contact area [21][32].

For the low-met material sliding at high velocity, the friction coefficient increased in the first brake stops, then markedly decreased (Fig. 6.2.6). This is a friction instability and seems to be well correlated to the damage of the secondary plateaus, observed in Fig 6.2.16, and to the variation of the contact area of the secondary plateaus (Fig. 6.2.17). Regarding this, Kim et al. observed a similar phenomenon in a material containing steel fibers, the friction coefficient decreased with increasing velocity [98], suggesting that it was triggered by the decrease in the contact area of the secondary plateaus. In our case for the low-met material, although the coverage factor is slightly higher at higher velocity. The compaction of

the secondary plateaus is significantly lower. In fact, a good degree of compaction of the secondary plateaus should promote the frictional force, since the cohesive forces among the particles forming the secondary plateaus are stronger [48][47].

Other observations in agreement with damage of the secondary plateaus due to particular braking conditions are provided by the study Verma et al. [77] and Cristol-Bulthé et al. [51] [23]. The first Authors [77] observed an increase in the wear rate associated due to reduced capability of forming stable secondary plateaus for disc temperatures in the range of 170-200 °C. Starting from these temperatures, locally on the surface of the friction material, the temperature can activate the degradation processes of the binder [14]. This reduced the capability of the substrate to retain debris on the surface, hence hindering the formation of stable and resistant secondary plateaus. The study by Cristol-Bulthé et al. [51] noticed deeper lowlands and scarcer secondary plateaus on the surface of friction material with the progressive degradation of the organic binder. Although the PoD testing conditions and the subscale dynamometer are different, we think that the contribution of high peak temperatures, with the high mechanical stresses, hindered the capability of formation of compacted secondary plateaus for the low-met material.

The wear rate of the friction materials is inherently related to the rate of formation and disruption of the friction layer. The higher wear rate of the disc of the low-met material is ascribable to the presence of fibers and a generally larger amount of abrasives. The steel fibers in the low-met materials act in a twofold manner. First, they exert strong adhesion towards the disc contributing to its wear. Second, steel fibers represent preferential sites, for the forming of secondary plateaus, where the particles pile up and get compacted. In this case, indeed, the fibers indirectly through the secondary plateaus, have an important protective action [49][99]. The relatively lower extension of the friction layer, approx. 55% and 40 % for the NAO and low-met respectively, are also in agreement with the higher wear of the low-met materials, as a higher surface fraction not covered by secondary plateaus is in direct contact with the disc. In addition, few and thick contact areas are more liable to disruption [72]. The observations by Kim et al. [98] are in agreement with this behavior: large local contact pressure are more likely to cause instability in the secondary plateaus. At low velocity, the wear rates of the low-met and NAO materials are comparable. At high velocity, the wear rate increases slightly for the NAO and more importantly for the low-met material. The friction layer at high velocity appears thicker and more compact for the NAO material (Fig. 6.2.15). Indeed, the higher wear rate has a positive effect on the NAO material as the friction layer achieves rapidly stable conditions protecting the bulk material. In fact, for the NAO material, the wear rate displayed just a slight increase, approximately linear, with the velocity (Fig. 6.2.9), compared to the wear rate of the low-met material, which significantly increases with the velocity with an approximately quadratic relationship (Fig. 6.2.12).

Regarding the sensitivity of the wear rate to pressure and velocity, the wear rate of the low-met material increases with pressure at high velocity, whereas at low velocity, the pressure displays a lower influence. On the other hand, for the NAO material, the effect of velocity on wear rate is lower compared to the low-met material and pressure has a higher influence than the velocity. As the severity of the wear rate increases with the velocity, both

materials displayed a composition of the friction layer richer of pad constituents (Fig. 6.2.18). For the tested braking conditions, the calculated K_a was $2-8 \cdot 10^{-14} \text{ m}^2/\text{N}$, typical values in the range of mild wear conditions [14].

For both materials, the mean concentration of emitted airborne particles can be described by a cubic relationship on the velocity, in agreement with trends reported in the literature [67]vnnieman. From high to low velocity, the emission changes by approximately two orders of magnitude. The pressure has a slight and non-monotonous effect on the particle emissions. Men et al. suggested that the intensity of braking action has two opposite impacts on the emissions. Although high braking intensity can increase the instantaneous particle concentration, this does not imply higher emissions as the high intensity also shortens the brake duration [85]. Thus, the influence of pressure is a combination of instantaneous concentration rise and braking duration. The velocity increases both the braking duration, for the higher braking energy, and the wear rate. These are the two main factors determining the dominating influence of velocity on particle emissions.

In particular, for the low-met material, the emissions decreased with repeated brake stops. Park et al. [60] found higher emissions in friction materials containing steel fibers compared to fiber-free materials, like NAO materials. The Authors highlighted the role of the surface morphology in the emission behaviors: surfaces characterized by deep lowlands, displayed higher emissions than widespread and smooth surfaces, typical of NAO materials. A widespread and well-compacted friction layer represents an obstacle to the particles' mobility, reducing the number of particles leaving the surface. On the other hand, the low-met material displayed higher emissions when the secondary plateaus, acting like a reservoir of particles, are not able to accommodate the high stresses induced by high velocity [60].

The third-body concept was introduced in Section 3.4, and such phenomena can explain the higher variability of emissions observed in the reference blocks (Fig. 6.2.4): less compacted secondary plateaus mean a higher probability of loose particles, which are easily emitted from the tribo-system involving the low-met material, whereas in the case of the NAO material, the widespread friction layer reduced the release of the particle. The huge differences in the surface characteristics also suggest different friction behaviors acting during the reference blocks. The low values of friction coefficient in Fig. 6.2.3 are related to the reference block that followed high-velocity brake blocks. Comparing Fig. 6.2.16 and Fig. 6.2.11, the NAO material showed a reduction in the compaction of the thickness of the friction layer passing from high to low velocity, whereas the low-met material reacts to new conditions increasing the compaction of the secondary plateaus. Observing Fig. 6.2.3, the restoring of the friction coefficient, or recovery behavior, can be assessed. The two materials display a different nature regarding the recovery behavior. During the reference blocks the low-met material shows values both higher and lower than the values of bedding (blue line), whereas the NAO material shows friction values generally lower compared to the bedding conditions. In addition, the distance between the blue and black is larger after the severe pv-blocks compared to the low-met material (Fig. 6.2.3): suggesting that the NAO material restores the friction coefficient in a larger number of brake stops compared to the low-met material.

Finally, Fig. 6.2.19 is proposed for a concise visualization of the observed relationships between the system wear and friction coefficient, and the system wear and emissions. As seen in Fig. 6.2.9, the NAO material displays a wear rate that is always lower than, say, $4 \mu\text{m}/\text{brake event}$, whereas the low-met material displays a wear rate, as the depth of wear, larger than $4 \mu\text{m}/\text{brake stop}$ at sufficiently high pressure and speed. As known, the friction coefficient is generally proportional to the extension of the secondary plateaus and their Fe-content, since both these effects influence the adhesive interactions between the pad and the disc and relevant contribution to friction [39][95]. With increasing wear rate, the extension of the friction layer decreases because of the increased rate of its disruption. As a consequence, the friction coefficient decreases, and this phenomenon is particularly evident in low-met materials. In the most severe conditions of pressure and velocity, the disruption rate of the friction layer is very intense, and therefore the wear rate is high, and the friction coefficient is low. In addition, the emission of airborne particles is very intense in these conditions, since the emission is generally proportional to the system wear. These mechanisms explain why, observing Fig. 6.2.19, wear rate and friction coefficient and wear rate and emissions show a good degree of correlation for the low-met material. The fact that for the NAO material, these correlations are weak is ascribable to the less variation of the surface characteristics under different braking conditions. In addition, for emissions, the delamination observed in Fig. 6.2.15 and 6.2.16 may suggest a mechanism that favors the detachment of coarse fragments at high velocity. This behavior was described in Section 6.1.2.3: non-airborne particles fall into the ground, hence are not detected by the OPS.

To sum up, under mild sliding conditions the NAO material performed better than the low-met material both in terms of friction, wear and emissions: friction coefficient was more stable and lower emissions and wear rate. However, as we will see in Section 6.4.1, it is important to consider the brake materials and the desired performance as low-met materials are preferable in terms of frictional and wear response under severe braking conditions.

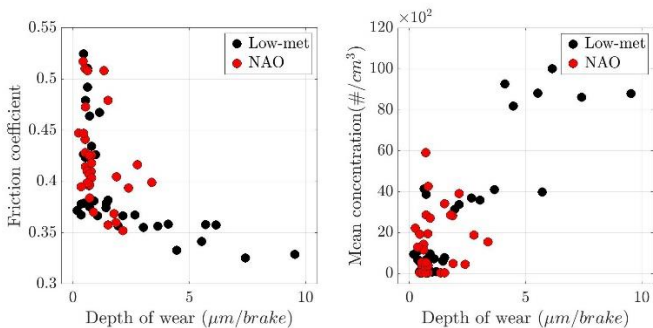


Fig. 6.2.19: Evolution of the friction coefficient and the average concentration of the airborne emitted particles as a function of the wear rate for the two friction materials (see figure's legend).

6.3 Relationship between specific wear rate and emission factor of brake materials

With the braking cycle developed in Section 5.3.2, the *Reduced Cycle*, the reference low-met material, the NAO, whose results were presented as a comparison in Section 6.2, and other eight materials were tested. The specific wear rate, K_a , and emission factors, EF , were obtained with Eq. 5.3 and 5.5 as explained in Section 5.3.2. This study evidences an interesting relationship between the specific wear rate and the emission factor. Reference is made to the Euro 7 regulation. The materials respect the limit of 7 mg/km/vehicle within the limit imposed within 2034 by Euro 7. However, only one low-met material respected the limit of 3 mg/km/vehicle, suggesting that further efforts are required to improve the emission behavior of low-met materials. Whereas the NAO and the coated disc respect the limit of 3 mg/km/vehicle confirming to be good strategies to reduce PM. Table 6.3.1 shows the mass (dM) and volume (dV) loss of the pad and disc materials, PM10, the sliding distance and the sum of sF-products for tested materials with the *Reduced Cycle*. The volume loss of the pad was computed by multiplying the area of the pad 4 by the thickness variation and the volume loss of the discs dividing the mass loss by the disc density.

Table 6.3.1: Mass (dM) and volume (dV) loss of the pad and disc materials, PM10, sliding distance and the sum of sF-products for tested materials with the *Reduced Cycle*.

	dM_{PAD} (mg)	dV_{PAD} (mm ³)	dM_{disc} (mg)	dV_{disc} (mm ³)	PM10 (mg)	SLIDING (km)	$\sum siFi$ (105 ⁵ Nm)
LM	450±40	270±	580±10	77±2	6.6±1.2	16.0±0.2	118.8±0.7
LM-2	510±7	284±	520±60	69±8	4.4±2.0	18.0±0.6	134.1±4.2
LM-3	445±55	355±150	860±30	114±4	7.5±1.2	17.2±0.3	120.0±2.2
LM-4	650±70	542±31	530±50	83±6	8.2±0.2	12.8±	85.3±0.1
LM-5	830±50	399±39	590±100	87±13	9.45±0.28	12.4±	82.9±1.0
LM-6	840±280	399±157	730±0.15	84±6	8.85±1.77	12.5±	82.2±1.4
NAO	240±60	122±12	100±5	14	2.0	15.7±0.3	111.9±0.7
NAO-2	423±43	203±11	59±8	8±1	8.4±0.4	16.5±0.6	115.4±4.7
NAO-3	339±57	191±7	32±10	4±1	3.9±0.35	16.3±0.9	116.6±7.8
LM-C	350	245	18	1	1.8±0.2	15.3±0.2	111.6±1.0

6.3.1 Specific wear rate

The specific wear rate for the disc and the pad were obtained for the pad and the disc using Eq. 5.3. and are reported in Table 6.3.2 and Fig. 6.3.1 showing a relatively good correlation (see Table 6.3.4).

Table 6.3.2: Specific wear rate of the disc and the pad for the tested materials.

	<i>LM</i>	<i>LM-2</i>	<i>LM-3</i>	<i>LM-4</i>	<i>LM-5</i>	<i>LM-6</i>
K_{aPAD} ($10^{-14}m^2/N$)	2.73±0.01	2.12±0.04	3.58±1.6	6.36±0.35	4.81±0.42	4.83±0.30
K_{aDISC} ($10^{-14}m^2/N$)	0.67±0.01	0.53±0.08	9.9±0.05	1.02±0.08	1.09±0.15	1.06±0.23
	<i>NAO</i>	<i>NAO-2</i>	<i>NAO-3</i>	<i>LM-C</i>		
K_{aPAD} ($10^{-14}m^2/N$)	1.09±0.09	1.76±0.14	1.64±0.09	2.20		
K_{aDISC} ($10^{-14}m^2/N$)	0.1±0.00	0.07±0.01	0.04±0.02	0.003		

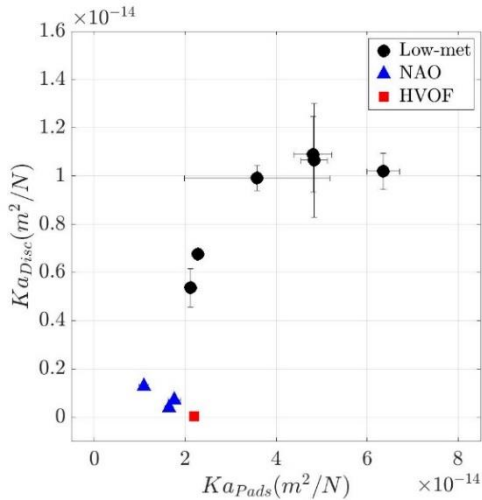


Fig.6.3.1: Specific wear rate of the disc and the pad for the tested materials.

6.3.2 Emission factors

The emission factors for the tested materials are reported in Table 6.3.3. Fig. 6.3.2-4 show the $K_{aDisc-EM}$, $K_{aPad-EM}$ and $K_{aSystem-EM}$ relationships. Reference is made to Euro 7 limitations (horizontal line) indicating the suggested values of K_a (vertical lines) of the pad to respect the imposed limits. The low met materials already respect the limit of 3 mg/km/veh. imposed by Euro7 limitation. The low-met material range between 3 and 6 mg/km/veh, thus only the limitation before 2034 is respect.

For low-met materials the emission factors show a good correlation with the specific wear rate of the pad and the disc. The graphs suggest that K_{aDisc} , K_{aPad} and $K_{aSystem}$ respectively of 0.8, 3 and 4 10^{-14} m²/N are value to consider to respect the limit of 3 mg/km/veh.

Regarding the relationship between the EF and K_{aDisc} , K_{aPad} and $K_{aSystem}$, Table 6.3.4 shows the Pearson's correlation coefficients for to the groups of materials low-met, low-met + NAO, low-met + NAO + LM-C (HVOF disc).

Table 6.3.3: Emission factors for the tested materials.

	<i>LM</i>	<i>LM-2</i>	<i>LM-3</i>	<i>LM-4</i>	<i>LM-5</i>	<i>LM-6</i>
<i>EF</i> (mg/km/veh.)	2.92±1.12	1.75±1.2	3.08±0.31	5.15±0.45	5.25±1.02	4.8±1.45
	<i>NAO</i>	<i>NAO-2</i>	<i>NAO-3</i>	<i>LM-C</i>		
<i>EF</i> (mg/km/veh.)	0.89	1.22±0.17	0.82±0.15	0.84		

Table 6.3.4: Pearson's correlation coefficient between K_{aDisc} - K_{aPad} , $K_{aPad-EM}$, $K_{aDisc-EM}$, and $K_{aSystem-EM}$

	K_{aDisc} - K_{aPad}	$K_{aPad-EM}$	$K_{aDisc-EM}$	$K_{aSystem-EM}$
<i>LM</i>	0.9	0.77	0.85	0.80
<i>LM + NAO</i>	0.86	0.85	0.88	0.87
<i>LM + NAO + HVOF</i>	0.86	0.85	0.91	0.88

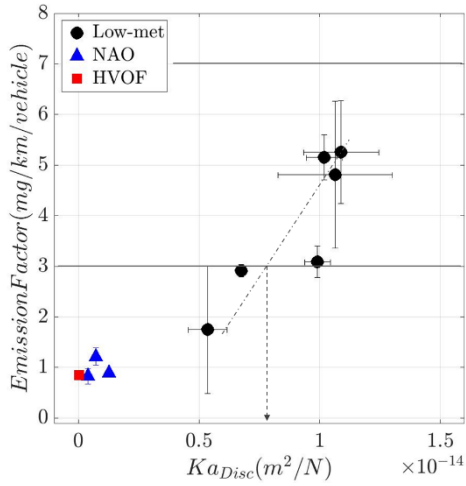


Fig.6.3.2: Emission factors as a function of the specific wear rate of the disc material for the tested material.

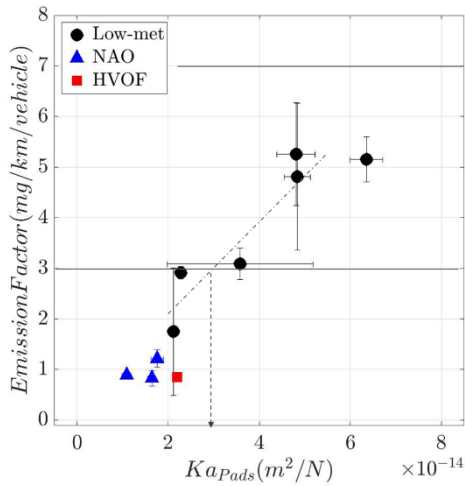


Fig.6.3.3: Emission factors as a function of the specific wear rate of the pad material for the tested material.

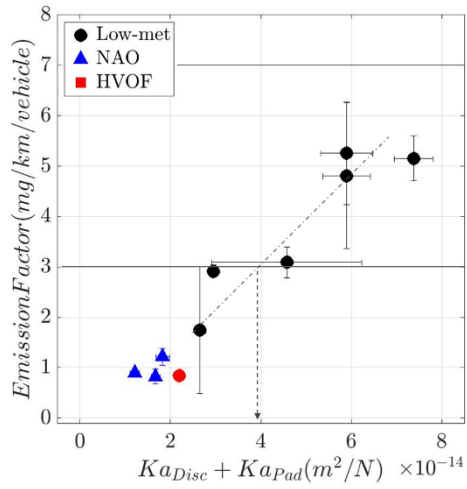
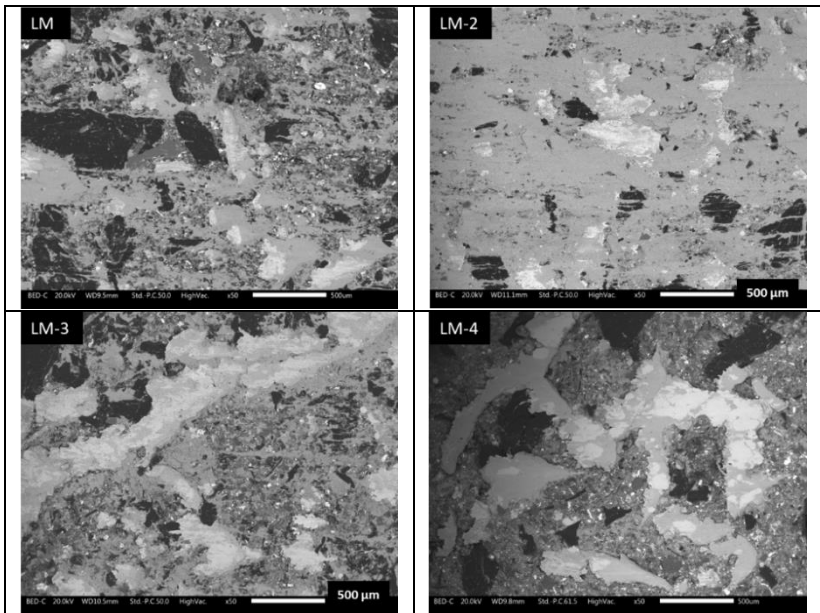


Fig.6.3.4: Emission factors as a function of the system specific wear rate for the tested material.

6.3.3 Characterization of the worn surfaces

SEM observations are depicted in Fig.6.3.5. It is interesting to observe that the *LM-4*, *LM-5*, *LM-6* which are modifications of the *LM* (the reference lo-met material) displayed significantly higher wear of the pad and, especially, of the disc. Accordingly, their emission factors feature high values. From Fig. 6.3.2-4 these materials displayed a scarce presence of secondary plateaus. Hence, the steel fibers, or primary plateaus, represent most of the contact area. As can be observed from Fig. 6.3.5 and considering that these materials have approx. the same content of steel fibers, we can infer that the fibers attained higher plastic deformations compared to the friction material with a higher percentage of secondary plateaus. Thus, the higher emissions observed for these materials can be, at least in part, ascribable to the high adhesion and abrasion interaction of the fibers toward the disc. On the other hand, for the materials featuring lower emissions, the secondary plateaus were more effective in reducing the wear, hence the emissions, acting as a third body (see Section 3.4). A third body of iron oxide, mechanically mixed with pad ingredients, prevents direct contact with the substrate and has lower chemical and mechanical interactions.



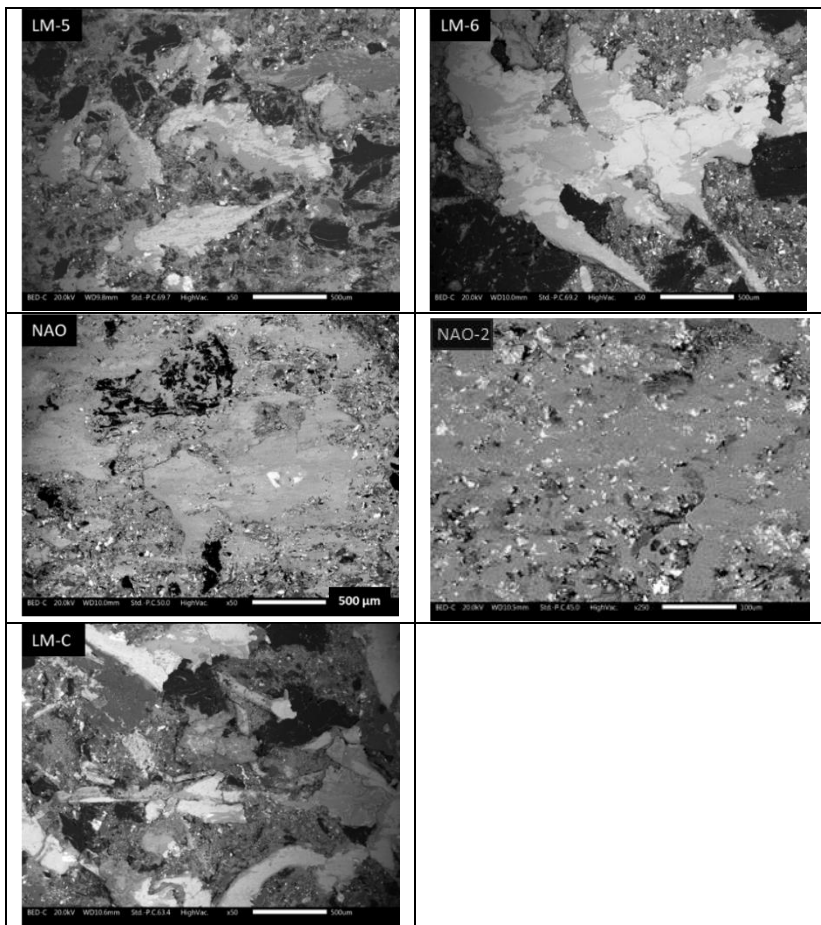


Fig.6.3.5: SEM observations of the worn surfaces of the tested friction materials.

6.4 Development of a Modified AK-Master Braking Cycle for frictional, wear and emission evaluations of brake materials

The modifications applied to the SAE J 2522 testing procedure, also known as *AK-Master*, were explained in Section 5.3.3. As the original procedure is suited for friction characterization only, the modifications were done to include wear and emission evaluations to have a more extensive characterization of brake materials. This study is a comparison between the reference low-met material and the NAO material. Sections 6.4.1-6.4.3 report respectively the results on the friction coefficient, wear and emissions. In agreement with the study in Section 6.2, the NAO material showed a higher friction coefficient, lower emissions and wear than the low-met material under mild conditions. However, as the braking conditions shift to severe conditions, the NAO displayed higher wear higher and a more marked decrease in the friction coefficient.

6.4.1 Friction coefficient

As representative sections for the friction characterization, we considered the speed-pressure sensitivity (Fig. 6.4.1) and the sections for the high-temperature characterization (Fig. 6.4.2).

From the speed-pressure sensitivity sections (Fig. 6.4.1), the NAO material displayed a decrease of the friction coefficient with pressure and velocity, whereas the low-met exhibited a decrease with pressure and velocity up to 120 km/h, from 120 to 200 km/h the friction increased. The NAO material has a higher friction coefficient than the low-met material from 40 to 120 km/h, however, from 120 km/h to 200 km/h the friction coefficient is higher for low-met material. These results are in general agreement with the frictional behavior observed from the Reduced Cycle (Fig. 6.2.7): the NAO displayed higher friction coefficients for all the tested conditions. In Fig. 6.4.1, for the velocity of 160 km/h, the higher friction level of the low-met materials compared to the NAO can be interpreted considering the unstable behavior observed at high velocity (Fig. 6.2.6) and discussed in Section 6.2.5. The low-met material displayed higher values of friction coefficient during the first brake stops during the high-velocity blocks, including the blocks at 160 km/h. This behavior was correlated with a marked increase in the extension of the secondary plateaus, although, with a poor degree of compaction (Fig. 6.2.15-16).

At high temperatures (Fig. 6.4.2), the friction behaviors of the two materials are comparable for the sections Increasing-T and p-500. In the Fade 1 section, the NAO material displayed a slight decrease in the friction coefficient, whereas the low-met material featured a more stable friction coefficient during the 15 brake stops. In the most severe conditions of the Modified Fade 2 section, both materials displayed a significant decrease in the friction

coefficient. The NAO material exhibited a higher decrease in the friction coefficient than the low-met material.

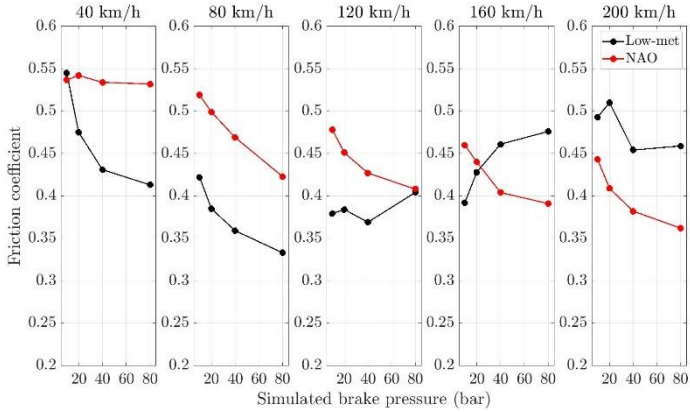


Fig.6.4.1: Friction coefficient of the pv-blocks section.

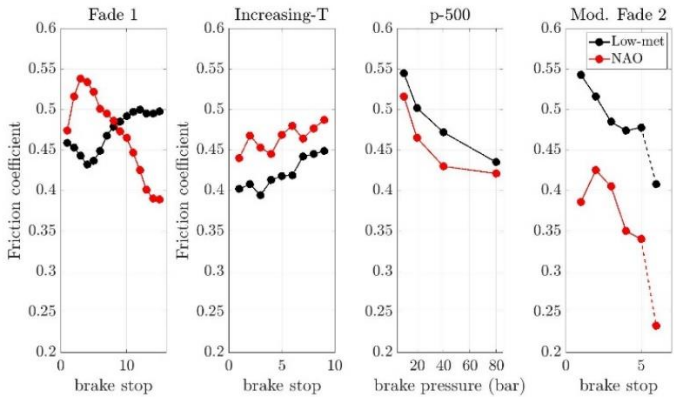


Fig.6.4.2: Friction coefficient of the sections: Fade 1, Increasing T, p-500 and Modified Fade 2

6.4.2 Wear rate

Fig. 6.4.3 shows the specific wear rate with Eq. 5.3 using LVDT measurements. It is interesting to notice that the NAO material has lower wear than the low-met material just for the Section of the *pv-blocks*. These braking conditions are comparable to those of the *Reduced Cycle* (Section 5.3.2), and are typical of mild sliding conditions, as explained in Section 4.1 and Section 6.2.5. Thus, in agreement, with the results in Fig. 6.2.9, the NAO material displays a lower wear rate than the low-met material. The K_a for these conditions is approx. $2.5 \cdot 10^{-14} \text{ m}^2/\text{N}$, and correspond to $1\text{-}8 \text{ }\mu\text{m}/\text{brake stop}$ (Section 6.2.3.3). On the other hand, for the section *Fade 1* and *Modified fade 2* the wear rate of the NAO material is higher than the wear rate of the low-met material. For the low-met material, the friction coefficient is comparable during the *pv-blocks* and *Fade 1*. The braking conditions in these sections have a mean disc temperature of $400 \text{ }^\circ\text{C}$, 8 m/s of initial sliding velocity and 1 MPa of contact pressure. For the NAO the wear rate increases slightly from $1.5 \cdot 10^{-14} \text{ m}^2/\text{N}$ in the *pv-blocks* to $4 \cdot 10^{-14} \text{ m}^2/\text{N}$ in the *Fade 1* sections. In section *Mod. Fade 2*, the wear rates significantly increase to value to values of 10 and $40 \cdot 10^{-14} \text{ m}^2/\text{N}$ for the low-met and NAO met materials respectively. The wear rate is high, and it is approx. 10 times higher than under mild conditions, corresponding to approx. 15 and $90 \text{ }\mu\text{m}/\text{brake stop}$ for the low-met and the NAO materials respectively. The mean disc temperature, the initial sliding velocity and contact pressure are respectively $500 \text{ }^\circ\text{C}$, 22 m/s and 2 MPa . The wear rate is lower for the low-met material because the steel fibers better resisted the mechanical stresses at high temperatures, whereas the oxide layers are very sensitive to thermal stresses [51]. Finally, in *Mod. Fade 2* the high wear rate observed is well-correlated with the decrease in the friction coefficient (Fig.6.4.2).

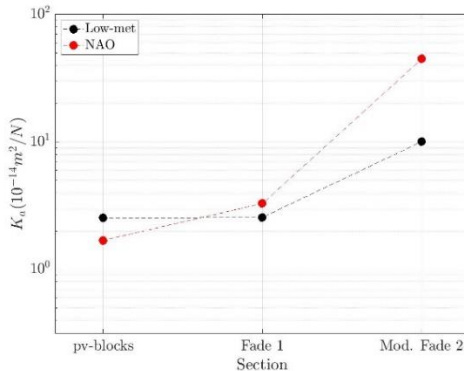


Fig.6.4.3: Specific wear rate of the sections: pv blocks, Increasing-T + p-500 and Modified Fade 2.

6.4.3 Emissions

Fig. 6.4.4 shows the time series of total concentration respectively of the run-in, the steady state of bedding, and the 40, 80 and 120 pv-blocks. The evaluation of emissions was obtained as a sum of the particle number in the section steady state (3 steps of bedding) and the pv-blocks at 40, 80 and 120 km/h with the respective reference blocks. The velocities of 160 and 200 km/h were not accounted for to maintain broad comparability with the WLTP cycle, in which the maximum velocity is approx. 150 km/h. The particle number was obtained with Eq. 5.6. The cumulative particle number of the reference low-met material is approx. $1.45 \cdot 10^{13}$ and is not significantly higher than the respective value for the NAO material. At the end of this bedding procedure, the difference between the reference low-met and NAO materials is significantly less marked than what was observed in the bedding of the *Reduced Cycle*. This difference can be explained both by the different braking conditions of the bedding and that a part of the variation is also ascribable to a different pad of the same friction material.

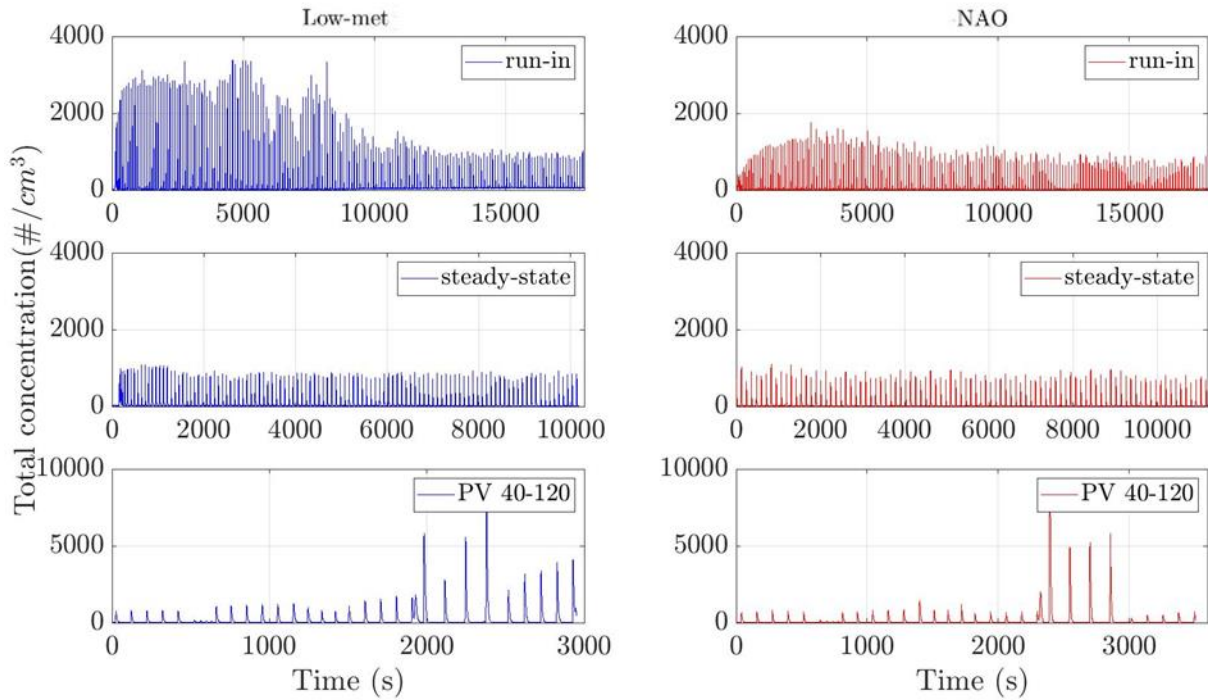


Fig.6.4.4: time series for the NAO and low-met (friction materials in the run-in stage (top) and steady-state of bedding, and PV 40 to PV120 block, with the respective Reference Blocks.

6.5 Brake performance under mild and severe sliding conditions of conventional cast iron and cermet-coated discs

As mentioned in Section 2.1, the deposition of hard coating on the disc surface is a good strategy to reduce brake emissions. The emission factor for the brake coupled with the WC-Fe-Al-Cr cermet-coated disc (Section 5.2.3) is approx. 4 times lower than the brake coupled with conventional cast iron in this study (Section 6.3).

Along with environmental requirements, brake materials demand excellent braking performance. For this, in this Section, we focused on the comparison between the brake performance of a conventional cast-iron and cermet-coated disc. The friction materials *LM* and *LM-C* (see Section 5.2.3) were tested respectively against the conventional cast-iron and cermet-coated discs. The brake performance was studied with an internal Brembo testing procedure, referred to as *pvT-friction Maps Brake Cycle*, to map the friction coefficient as a function of pressure, velocity and temperature (Section 5.3.3). The main contribution of this cycle with respect to the *Reduced Cycle* and *SAE J 2522* is that the braking parameters cover a wider range of conditions, especially in terms of temperatures. As done in the methodology of Sections 6.1.2.1 and 6.2.4, SEM characterizations of the worn surfaces of the disc and, especially, the friction materials after specific tests were done for the interpretation of the wear mechanisms. In addition, specific brake blocks were repeated to have an accurate evaluation of the wear rate for the braking conditions of interest.

The correlation and variation of the friction coefficient with *pvT conditions* are discussed with the distribution of Spearman's coefficient, r , and Relative Standard Deviation (*RSD*). The effect of pressure causes a monotonic decrease in the friction coefficient. The two brake couples showed comparable frictional behavior below 300 °C of initial brake temperature. The effect of temperature is generally to cause an monotonic increase in the friction coefficient and depends on the temperature level. However, for both brake couples, the *fade effect* was found for high vT combinations, above 300 °C and 140 km/h. The *fade effect* was correlated to the primary plateaus being progressively covered at increasing T by a thick layer of iron oxide. Finally, a peculiar behavior, *friction instability*, was observed for the cermet-coated disc above 300 °C and low-intermediate velocity. This was ascribed to the different behavior in forming 'glazes' and to the lower source of iron for tribo-oxidative processes.

6.5.1 Contact temperature

The initial brake temperature (T) ranges from 50 to 650 °C. During each brake stop, the disc temperature increases with time up to a maximum value decreasing afterward. The temperature rise (dT_{max}) during the brake stops are shown in Fig. 6.5.1 according to the testing velocity for the cast iron and the coated discs. The temperature rises are approximately 80, 180 and 250 °C respectively at 90, 140 and 200 km/h of initial vehicle speed. In addition, the temperature rises are slightly lower for the coated disc than for the cast-iron disc.

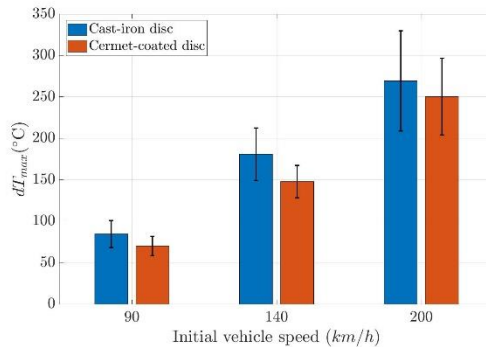


Fig. 6.5.1: The temperature rise (dT_{max}) as mean and standard deviation at the tested velocity for the cast-iron and coated disc.

6.5.2 Friction coefficient

The recorded coefficient of friction changes during each brake. An example is shown in Fig. 6.5.2. Fig. 6.5.2 shows the evolution of the friction coefficient during three brake stops at the different brake pressure, of 2, 6 and 14 MPa, while the other two braking parameters, namely 200 °C of initial brake disc temperature and 90 km/h of initial vehicle speed, are kept constant. Increasing the pressure from 2 MPa to 14 MPa shortens the brake duration by approx. 3 to 10 seconds. At the pressure of 14 MPa, the initial run-in appears more marked, however, the signals reach lower values during the brake event. On the other hand, at the intermediate pressure of 2 and 6 MPa, the friction coefficients gradually increase.

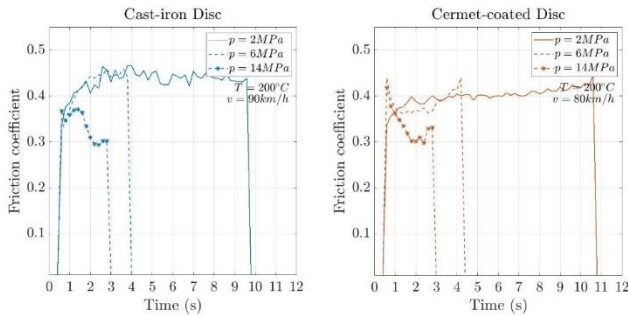


Fig. 6.5.2: Evolution of the friction coefficient during the brake stops at the simulated brake pressure of 2, 6, 14 MPa and 200 °C of initial disc temperature and 90 km/h of initial vehicle speed for the cast iron disc (left) and coated disc (right) brake couples.

The mean values of the friction coefficient are plotted in Fig. 6.5.3-4 for the two tested brake couples. The friction coefficients are divided into two groups: *Low-temperature*, in the first row, and *High-temperature*, in the second row, as explained in Section 5.3.4. In the graphs, the friction coefficient is a function of simulated brake pressure at the different vehicle speeds and the initial disc temperatures for both the brake couples under analysis.

The relationship between the average friction coefficient and the brake pressure is decreasing. The blue lines depict the brake stop of the initial disc temperature of 50 °C and 300 °C respectively in the first and second rows, while the red line the temperatures of 200 °C and 650 °C. These lines suggest that the general relationship with temperature is increasing between 50 and 200 °C for both the brake couples. For the cast-iron disc, this holds also for temperatures between 300-650 °C for the velocity of 90 km/h. However, for the velocity of 140 km/h, the influence of temperature on the average friction coefficient is slightly decreasing, almost negligible, at high pressures. For the coated disc, at 90 and 140 km/h, the friction coefficient shows a high variation of friction coefficient for little variation in the pressure and temperature. For instance, at 4 MPa, the friction coefficient reaches high values above 0.6 at the initial disc temperature of 650 °C, whereas for the higher brake pressure of 6 and 8 MPa, the friction coefficient is decreasing with the temperature. For the initial vehicle velocity of 140 km/h, the friction coefficient displays a decreasing trend with temperature and high fluctuations. For this range of parameters, the friction coefficient may not follow the general behavior, the monotonous decreasing trend with pressure, as the influence of contact temperature has a significantly higher influence on the brake performance. For this reason, this phenomenon will be referred to as *frictional instability*.

Finally, both the brake couples showed a marked decrease in the friction coefficient between 300-650 °C at 200 km/h. This behavior is generally referred to as the *fade effect*. Regarding the influence of velocity, the relationship of the friction coefficient with

the vehicle speed is not defined univocally. This means that monotonous trends of the friction coefficient between 90 and 200 km/h are rare.

These considerations on the relationships of the friction coefficient with the input parameters can be better defined with the Spearman's coefficient, r_μ , (Eq. 5.7) and the relative standard deviation, RSD (Eq. 5.8). The RSD and Spearman's coefficients were computed dividing the data into the two main groups *Low-temperature* and *High-temperature*, following the data visualization proposed in Fig. 6.5.2. The distribution of Spearman's coefficients are depicted respectively in Fig. 6.5.5 for both the brake couple. The Spearman's coefficient for pressure, $r_{\mu p}$, shows that almost 70 % featured values approx. to +1, confirming that for both brake couples, the pressure is negatively correlated. As mentioned, the effect of the velocity is not univocal, in fact, most $r_{\mu v}$ values are around 0. For the cast-iron disc, the correlation with temperature is generally positive, more than 50 % of values are +1. Approx. 20 % of the sample displays values around -1 and most of these are the points at 200km/h and 300-650 °. The coated disc shows a significantly higher frequency of negatively correlated points, around 40 %, as a consequence of the friction instability at 90 and 140 km/h and 300-650 °C.

Regarding the analysis of the variation, the RSD distributions (Fig. 6.5.6) confirm that the pressure is the most influencing parameter for both brake couples. The RSD values of 0.15 and 0.20 for the cast-iron disc and coated disc respectively. The RSD values for velocity are in the range of 0.1 and the distributions appear very sparse for the coated disc. This agrees with the observed friction instability at 90-200 km/h and 300-650 °C. The RSD values for temperature are around 0.5 for both the brake couple with the median slightly lower for the coated disc brake couple.

The distribution of RSD and r_μ were used to assess the degree of variation of the friction coefficient with respect to each input parameter. The values depend on the system and the design of the experiment. The highest variation is found for the pressure, and it is higher for the coated disc. The distribution of RSD for velocity is much sparser from the coated discs, featuring higher variation. The T variation, $RSD_{\mu T}$, is slightly lower for the coated disc.

The analysis with RSD and r coefficient was proposed to avoid the dependency on the model's choice as the main object of the work is to study relationships between the tribological behaviors and surface characteristics, rather than the modeling of the friction behaviors. Although the relationships are complex and not linear, linear regressions are reported in Table 6.5.1 to refer to the results with robust statistical analysis. The data were grouped into *low-* and *high-Temperature*, respectively below and above 300 °C. In general, the outputs of the linear regression are in good agreement with the $RSD-r$ analysis. Observing Table 6.5.1, all the factors results significant at the 5 %, expect the T in the linear regression with of the groups High-temperature ($T > 300^\circ\text{C}$) for both brake couples. Whereas, for temperatures below 300 °C, the effect of v causes an increase in the friction coefficient.

Table 6.5.1: Estimates, standard error of the coefficient (SE), t-statistics (t-stat) and p-value of the linear regressions for the cast iron disc and coated disc and temperature below and above 300 °C.

Cast-iron Disc BC – T<300 °C	Estimate	SE	t-stat	p-value
<i>Intercept</i>	0.39463	0.011588	34.056	5.02E-66
<i>p</i>	-0.0097931	0.00078284	-12.51	5.96E-24
<i>v</i>	0.00036819	6.58E-05	5.5996	1.25E-07
<i>T</i>	0.00019079	3.90E-05	4.8907	2.96E-06
Cast-iron BC – T>300 °C	Estimate	SE	t-stat	p-value
<i>Intercept</i>	0.50453	0.013346	37.805	2.87E-70
<i>p</i>	-0.00968	0.000707	-13.693	1.23E-26
<i>v</i>	-7.34E-06	5.14E-05	-0.14257	0.88686
<i>T</i>	-7.56E-05	2.33E-05	-3.2502	0.001482
Coated Disc BC – T<300 °C	Estimate	SE	t-stat	p-value
<i>Intercept</i>	0.36505	0.01503	24.288	9.77E-51
<i>p</i>	-0.0131	0.001015	-12.911	3.17E-25
<i>v</i>	0.000833	8.41E-05	9.8992	1.20E-17
<i>T</i>	0.000253	4.94E-05	5.1221	1.04E-06
Cast-iron BC – T>300 °C	Estimate	SE	t-stat	p-value
<i>Intercept</i>	0.58033	0.034715	16.717	3.98E-33
<i>p</i>	-0.01227	0.001798	-6.8272	3.78E-10
<i>v</i>	0.000256	0.00013	1.9701	0.051134
<i>T</i>	-0.00023	6.18E-05	-3.7053	0.000321
	Cast-iron Disc BC- T<300 °C	Cast-iron BC- T>300 °C	Coated Disc BC-T<300 °C	Cast-iron BC- T>300 °C
<i>R-squared</i>	0.62	0.64	0.70	0.39

To sum up, the sensitivity of each braking parameter is different according to the brake couple. Both materials display a clear decrease in the friction coefficient with brake pressure for all the tested conditions. Both the brake couples display an increasing trend with the temperature between 50 to 200 °C. The cast iron disc maintains this trend up to 650 °C of initial brake temperature for the initial velocity of 90 and 140 km/h, not at 200 km/h. For both the materials at 200 km/h, the friction coefficient decreases to even lower values than those observed at low initial disc temperatures. Finally, the frictional behavior is strongly dependent on braking temperatures, and the decrease in brake efficiency, the so-called *fade effect*. However, the analysis of the coated disc did not respect the monotonous decreasing trend with pressure at 90 and 140 km/h and 300-650 °C. This peculiar phenomenon was identified as *friction instability*. When the variation in the monotony on an input parameter changes sign, the correlation of the input parameters with the output parameter is not easily defined. The

fade effect and friction instability will be better interpreted with the characterization of the worn surfaces in Section 6.5.4.

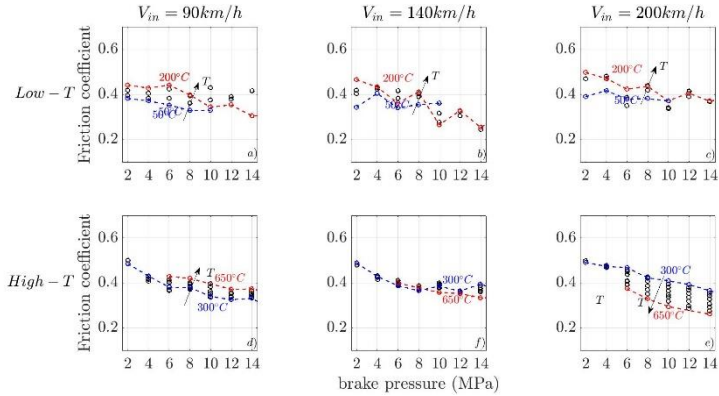


Fig. 6.5.3: Cast iron disc: average friction coefficient as a function of simulated brake pressure at different vehicle speeds for the initial disc temperatures of 50 to 200 °C (first row) and 300 to 650 °C (second row)

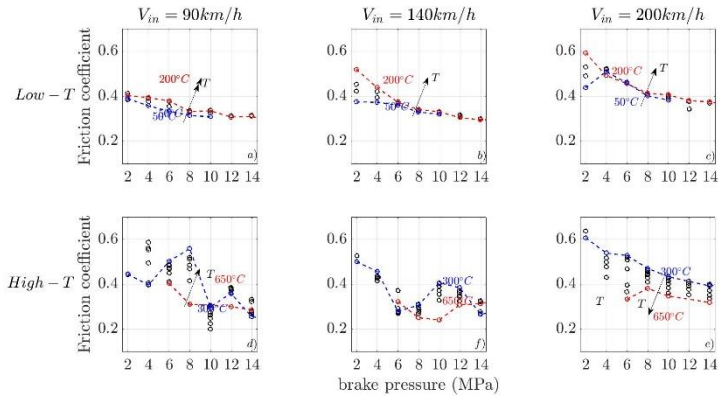


Fig. 6.5.4: Coated disc: average friction coefficient as a function of simulated brake pressure at different vehicle speeds for the initial disc temperatures of 50 to 200 °C (first row) and 300 to 650 °C (second row)

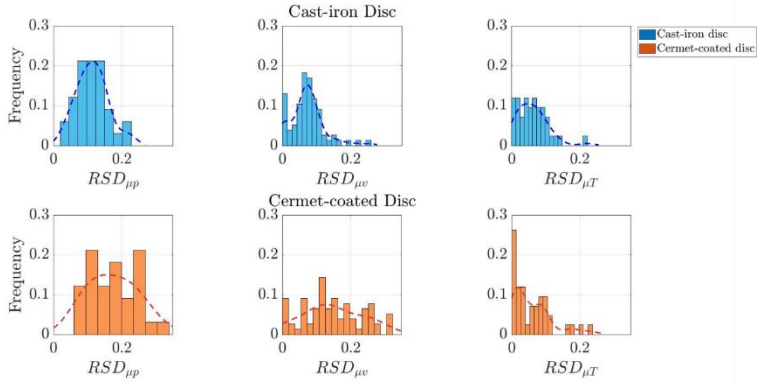


Fig. 6.5.5: Distribution of the relative standard deviations respectively for pressure, velocity and temperature for the cast iron disc (first row), and coated disc (second row).

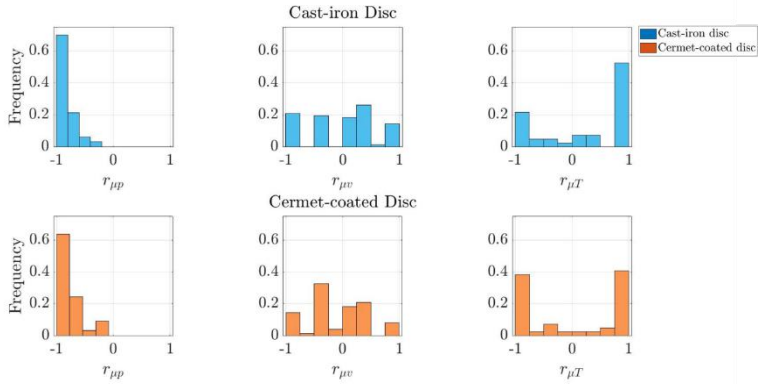


Fig. 6.5.6: Distribution of the Spearman's correlation coefficient for pressure, velocity and temperature for the cast iron disc (first row), and coated disc (second row).

6.5.3 Wear rate

Based on the observed frictional behavior, specific blocks of the applied procedure were repeated with new samples after the bedding procedure in order to evaluate the wear rate under different braking conditions. The specific wear rates, K_a , were computed with Eq. 5.3.

In the brake blocks the velocity and pressure were fixed, while the initial brake temperature ranged between 50-250°C or 300-650 °C. The braking conditions of the blocks are reported as follows:

- **Low-pvT**: $p=2$ MPa, $v=90$ km/h, $T=50-250$ °C;
- **Low-pv & High-T**: $p=4$ MPa, $v=90$ km/h, $T=300-650$ °C;
- **High-pvT**: $p=10$ Mpa, $v=200$ km/h, $T=300-650$ °C.

The wear rates are slightly lower and higher for *FM-C* than the *FM* respectively for the conditions denoted as *Low-pvT* and *Low-pv & High-T higher*, whereas the wear rates increase for both the friction materials passing from the braking conditions of *Low-pvT*, *Low-pv & High-T* and *High-pvT*. At the condition of *Low pvT* the K_a is typical of mild wear, in the range of $2 \cdot 10^{-14}$ m²/N and it is slightly lower for *FM-C*. For the conditions *Low-pv & High-T higher* and *High-pvT* the wear rate is respectively 7-10 10^{-14} m²/N and above $30 \cdot 10^{-14}$ m²/N. it is 4 and 14 times higher than the mild wear of approx. $2 \cdot 10^{-14}$, thus very severe wear was attained under these braking conditions [14].

Regarding the wear of the discs, the cast-iron disc displayed mild wear, in the range of $0.5 \cdot 10^{-14}$ m²/N, for the conditions *Low-pvT* and *Low-pv & High-T*. Whereas for these braking conditions, the wear rate of the coated disc is significantly lower, in the order of 10^{-17} m²/N. Interestingly, the wear rates of the two discs are comparable, under the conditions denoted as *High-pvT*, approx. $3 \cdot 10^{-14}$ m²/N. This wear rate at these braking conditions is significantly higher than at the other braking conditions: approx. 6-7 times for the cast iron disc and 2 orders of magnitude for the coated disc.

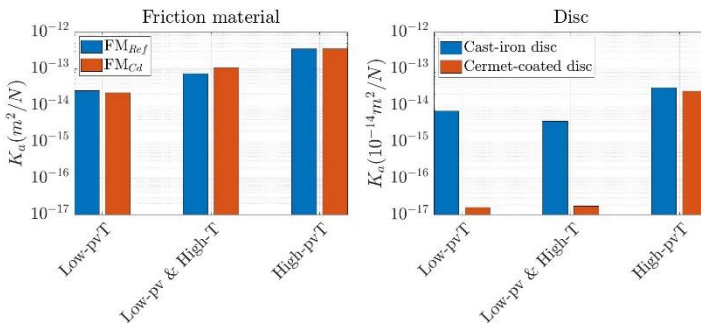


Fig. 6.5.7: wear rate of the friction materials (left) and the discs (right) for the block of *Low-pvT* ($p=2$ MPa, $v=90$ km/h, $T=50-250$ °C), *Low-pv & High-T* ($p=4$ MPa, $v=90$ km/h, $T=300-650$ °C) and *High-pvT*: $p=10$ Mpa, $v=200$ km/h, $T=300-650$ °C)

6.5.4 Characterization of the worn surfaces

6.5.4.1 Friction materials

A-posteriori SEM-EDXS analyses were done in order to understand the relationship between the frictional and wear behaviors with the surface characteristic. Based on the observed frictional behavior, the analyses were restricted to the following p v T conditions or both the brake couples:

- A) **Low- p v T** : $p=2$ MPa, $v=90$ km/h, $T=50^{\circ}\text{C}$;
- B) **Low- p v & Intermediate- T** : $p=2$ MPa, $v=90$ km/h, $T=200^{\circ}\text{C}$;
- C) **Low- p v & High- T** : $p=4$ MPa, $v=90$ km/h, $T=650^{\circ}\text{C}$;
- D) **High- p v & Intermediate- T** : $p=10$ MPa, $v=200$ km/h, $T=300^{\circ}\text{C}$;
- E) **High- p v T** : $p=10$ MPa, $v=200$ km/h, $T=650^{\circ}\text{C}$.

Figures 6.5.8 -10 show the backscattered electrons micrographs of the two friction materials after the test of respectively the brake conditions A-B, C and D-E. In addition, the coverage factors were computed by image analysis according to the methodology explained in Section 6.1.2.1. The coverage factors were obtained from 10 observations for each braking condition, and are reported in Table 6.5.2. Furthermore, Tables 6.5.3 and 6.5.4 report the compositional analysis of the friction layers in specific braking conditions.

Fig. 6.5.8 shows the observations of testing conditions *Low- p v T* (A) and *Low- p v & Intermediate- T* (B). The friction layer of the *FM* is characterized by primary and secondary plateaus. In addition, the black areas in the micrographs are chunks of graphite. For the *FM*, the observations at 50°C are typical of a surface after proper bedding procedures, as those observed in Section 6.1.2. On the other hand, the observation at 200°C , is characterized by a scarcer presence of secondary plateaus. On the surface of the *FM-C*, the brass fibers appear less bright than steel fibers because of the transfer material on them. This surface is characterized by a scarce presence of secondary plateaus, almost negligible, compared to the *FM* at both conditions. Hence, not many differences can be appreciated between the test at 50 and 200°C both at low p v values. However, the coverage factor has a comparable value, around 40 %, but the contact is attained mainly on the steel and brass fibers. For the *FM*, the coverage decreases at the temperature of 200°C for a lower presence of secondary plateaus. For the *FM-C*, instead, the coverage factor does not change, because the surface has a lower presence of secondary plateaus which is not affected by the temperature in this range of braking conditions as occurs for the *FM*. The composition of the secondary plateaus is made determined by the mechanical mixing of wear debris from the friction and the disc materials. As shown in Table 6.5.3, the secondary plateaus of the *FM*, are mainly made of iron, approx. 65 wt.%. Iron in the secondary plateaus originates from the wear of both the disc material and the steel fibers in the friction material.

On the other hand, for the FM-C material, under these conditions, the typically observed secondary plateaus, i.e. the extended regions of compacted iron oxide particles supported by the steel fibers, are negligible. Iron particles are detected mainly on the brass fibers and mixed with other ingredients. For the FM-C, the text will refer to secondary plateaus as this friction layer composed of brass fibers supporting compacted iron particles. In these regions, the Fe-content is approx. 23 wt.%. This difference in the Fe content is mainly ascribable to the low amount of iron in the disc material, which made approx. of 83 wt.% of WC and 13 wt.% of Fe [87]. Thus, the Fe content in these regions of the friction layers is mainly ascribable to the wear of the steel fibers. The content of W, approx. 5 wt.% in the secondary plateaus (Table 6.5.4), confirms that the disc contribution in the formation of the secondary plateaus is low.

Fig. 6.5.9 shows the surfaces of the friction materials after the braking conditions at *Low-pv & High-T* (C). The surface of the FM is characterized by a larger coverage, i.e., 45 %, and a higher presence of secondary plateaus compared to conditions at *Low-pvT* (A and B). On the other hand, the surface of the FM-C is characterized by few but very flat large patches, similar to the surface observed by Cristol-Bulthé et al. [51]. The coverage factor (Table 6.5.2) for these conditions is 30 %. In addition, the EDXS analyses (Table 6.5.4) on this friction layer revealed a large amount of W, above 55 %, meaning that a significant transfer from the disc occurred, being W contained in the disc material only. Comparing the W concentration from EDXS analysis after the conditions at *Low pv & High T* and *High pvT*, in which the W content is approx. 5 % the transfer of the disc material into the friction layer of friction materials is more than 10 times higher.

Regarding the observations in Fig. 6.5.10 after *High-pv & Intermediate-T* (D) and *High-pvT* (E) the surface display drastically different characteristics from conditions at *Low-pvT* (A and B, Fig. 6.5.8). First, secondary plateaus are very compacted glaze layers covering a significant portion of the surface. For these braking conditions, the coverage factors are generally in the 55 % range (Table 6.5.2). For the FM-C, only steel fibers are observable, whereas brass fibers are covered by glaze layers. The iron-oxide particles cover more easily cover the brass fibers compared to steel fibers for their higher ductility and surface energy.

Several cracks are present on the glazes of both friction materials. At this condition, a few graphite particles are still observable, however, almost the whole surface of the FM is covered by glaze layers, featuring a coverage factor of 85 %. The surface of the FM-C features a lower coverage, i.e., 55 % than in *High-pv & Intermediate-T* condition. As shown in the BED and SED observation in Fig. 6.5.10, the surface of the FM-C features large regions with loose particles deposited onto the glaze layers. The high magnification observation of the loose powder shows that the powder has a particle size lower than 1-2 μm . These regions could have determined an underestimation of the coverage factor for these conditions. The compositional analysis of this region is given in Table 6.5.4 and can be compared to the composition of the glaze layers. W content is 30 wt.%, three times higher than in the glaze region, suggesting that for such braking conditions, a variation in the wear mechanism of the coating occurred.

The increase in the intensity of tribo-oxidative processes with the contact temperature contributed to the formation of extended glaze structures, resulting in a high coverage factor. From the EDXS analysis, the nature of the oxide cannot be precisely identified. However, for the tested conditions of Table 6.5.3, the iron content in secondary plateaus is 65 ± 7 wt.% and the Fe/O ratio is 3 ± 0.2 displaying relatively low variation. On the other hand, for *FM-C*, the Fe-content, in the region where iron particles deposit on the brass fibers, has a high variation at the different braking conditions: the Fe-content is 23, 35 and 50 wt.%, respectively for *Low-pvT*, *High-pv* & *Intermediate-T* and *High-pvT*. The Fe content increases with the contact temperatures accompanied by a higher wear rate of the friction material and tribo-oxidative processes of the steel fibers contributing to the formation of large and compacted glazes.

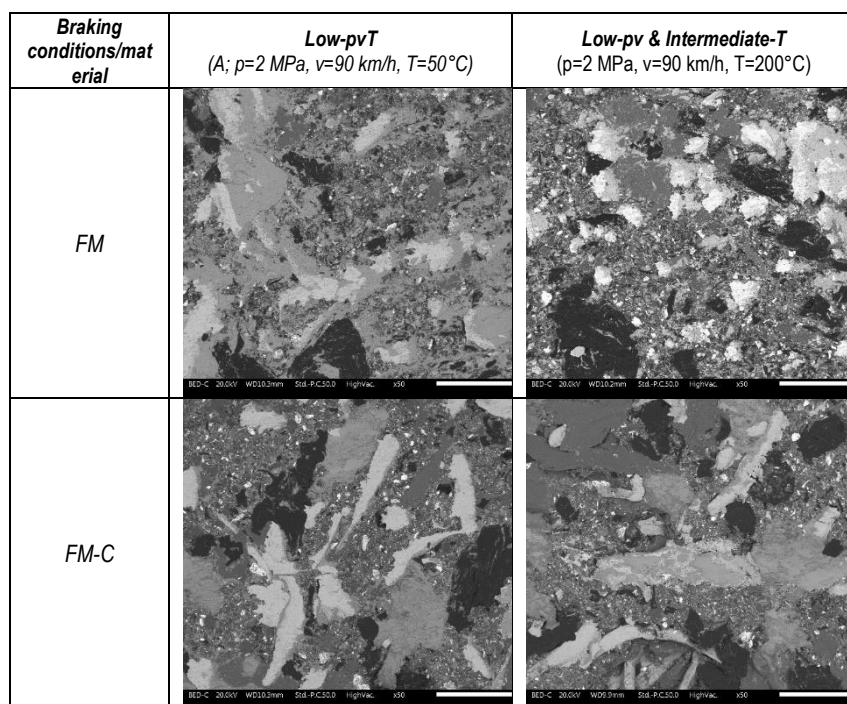


Fig. 6.5.8: Backscattered electrons micrographs of the friction materials *FM* (left) *FM-C* (right) at the braking conditions of *Low-pvT* (A; $p=2$ MPa, $v=90$ km/h, $T=50^\circ\text{C}$) and *Low-pv & Intermediate-T* (B; $p=2$ MPa, $v=90$ km/h, $T=200^\circ\text{C}$).

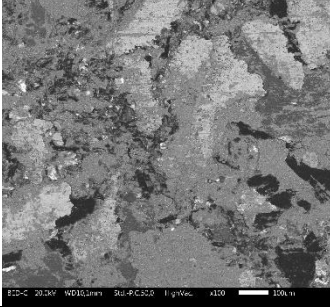
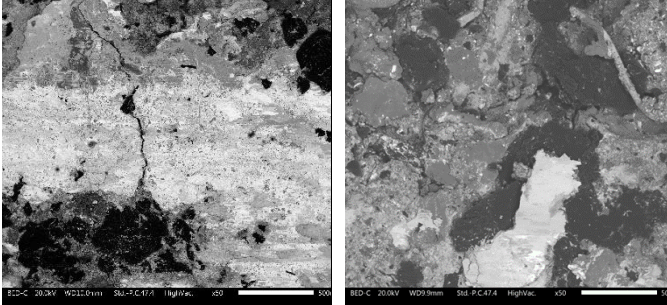
Braking conditions/material	<p style="text-align: center;">Low-pv & High-T (C; p=4 MPa, v=90 km/h, T= 650 °C)</p>	
FM		
FM-C		

Fig. 6.5.9: Backscattered electrons micrographs of the friction materials *FM* (left) *FM-C* (right) at the braking conditions of *Low-pv & High-T* (C; p=40bar, v=90 km/h, T= 650 °C).

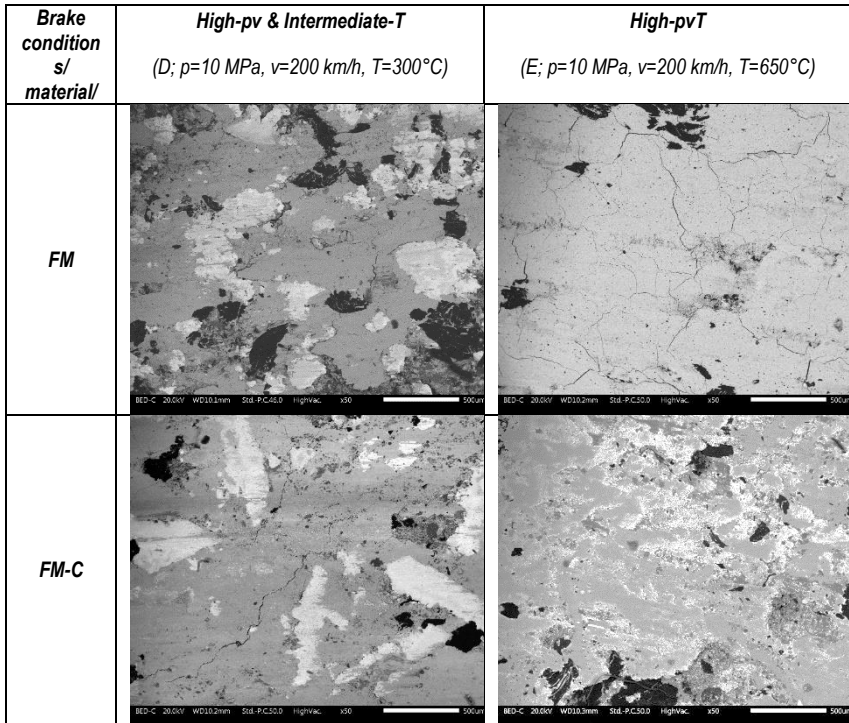


Fig. 6.5.10: Backscattered electrons micrographs of the friction materials *FM* (left) *FM-C* (right) at the braking conditions of *High-pv & Intermediate-T* (D, $p=10\text{ MPa}$, $v=200\text{ km/h}$, $T=300^\circ\text{C}$) and *High-pvT* (E; $p=10\text{ MPa}$, $T=650^\circ\text{C}$, $v=200\text{ km/h}$).

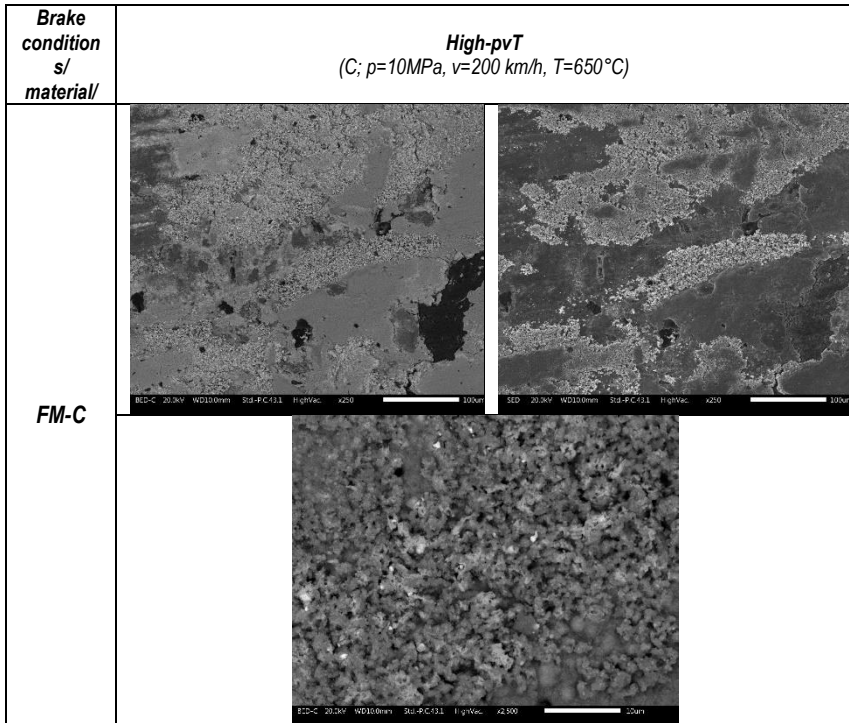


Fig. 6.5.11: Backscattered (left) and secondary (right) electrons micrographs of the *FM-C* after the testing condition *High-pvT* (E , $p=10\text{ MPa}$, $v=200\text{ km/h}$, $T=650^\circ\text{C}$).

Table 6.5.2: Coverage factor for the friction material sliding against the cast-iron disc and coated disc after specific braking conditions.

Brake conditions/ material/	A) Low-pvT	B) Low-pv & Intermetiade-T	C) Low-pv & High-T	D) High-pv & Int-T	E) High-pvT
<i>FM</i>	40 %	30 %	45 %	70 %	85 %
<i>FM-C</i>	40 %	40 %	35 %	70 %	55 %

Table 6.5.3: Elemental composition of the friction layer of *FM* after specific braking conditions as obtained from EDXS (in weight%). The carbon content was not included in the analysis.

Friction material	Braking conditions/ Element	Fe	O	Zn	Sn	Al	Mg	Cr	Si	S
FM	A) Low pvT	67.3	23.5	2.1	1.6	1.4	1.3	0.57	1.2	1.1
	D) High pvT	57.0	18.0	6.4	3.4	3.5	4.0	1.6	1.9	2.8
	E) High pvT	71.4	21.0	2.1	2.6	0.6	0.5	0.5	0.7	0.2

Table 6.5.4: Elemental composition of the friction layer of *FM-C* after specific braking conditions as obtained from EDXS (in weight%). The carbon content was not included in the analysis.

Friction material	Braking conditions/ Element	Fe	W	O	Cu	Zn	Sn	Al	Mg	Ca	Cr
FM-C	A) Low pvT	22.9	5.1	24.7	5.3	4.1	7.2	14.9	6.8	2.3	2.5
	C) Low pv - High T	18.2	55.7	16.4	0.6	0.9	1.5	2.0	6.4	0.5	0.8
	D) High pv & Int. T - glaze region	34.3	4.9	23.7	5.0	2.8	4.2	10.3	6.8	2.2	2.9
	E) High pvT - glaze region	49.7	9.5	27.8	1.9	1.5	4.9	0.8	1.5	0.6	1.4
	E) High pvT - poorly compacted region	26.8	30.5	21.2	2.1	1.8	4.0	5.0	3.2	1.1	2.7

6.5.4.2 Discs

To complete the picture emerging from the investigation conducted on the friction materials and relevant wear products, the SEM observations of the disc surfaces were acquired. They are depicted in Fig.6.5.12-13. The observations were acquired with an SEM after the *Low-pvT* (A) and *High-pvT* (E). The observations after *Low-pvT* show a moderate presence of scratches and material transfer for both disc samples. Regarding the surfaces after *High-pvT* conditions, a significant material transfer can be observed for both materials, confirmed by the elemental composition in Tables 6.5.4-5. The friction layers on the two discs are significantly different. The cast-iron disc presents some cracks, and its friction layers are large and uniformly extended on the surface. These patches are typical of a mild adhesive mechanism and subsequent filling with wear product of both the disc and especially the pad material. On the friction layer of the coated disc, a dark and bright region can be distinguished. The dark regions are small spots with a high content of pad ingredients, compared to the bright region, in which the W content is 70 wt.%.

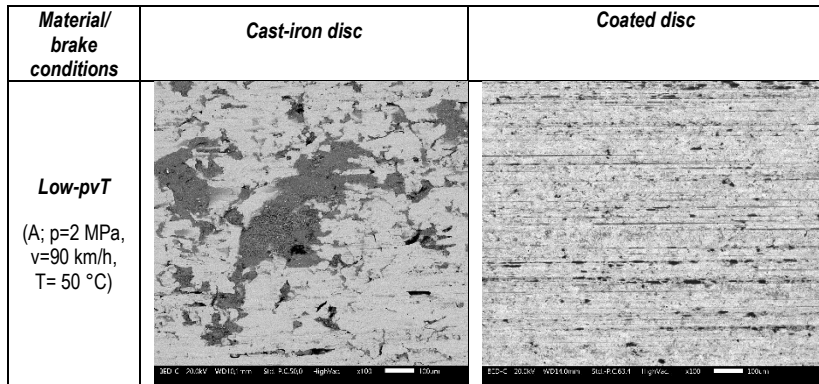


Fig. 6.5.12: Observations by BED micrographs, of the surfaces of the cast-iron and coated disc after the Bedding testing conditions.

Table 6.5.5: Elemental composition of the cast iron disc after *High-pvT* conditions as obtained from EDXS (in weight%). The carbon content was not included in the analysis.

Fe	O	Zn	Si	Sn	Mg	Al	S	Cr	Ca	Mn
56.0	17.3	8.0	4.8	3.4	3.2	2.8	1.9	1.3	0.9	0.3

Table 6.5.6: Elemental composition of the cermet-coated disc after *High-pvT* conditions as obtained from EDXS (in weight%). The carbon content was not included in the analysis.

	Fe	O	W	Cr	Al	Zn	Cu	Sn	Mg	S	Ca	Na
Bright region	7.6	12.4	69.56	5.7	0.9		1.5	1.5	0.3	0.0	0.0	0.4
Dark region	29.1	19.7	21.6	2.3	6.1	2.7	4.9	9.4	2.6	0.7	0.9	0.0

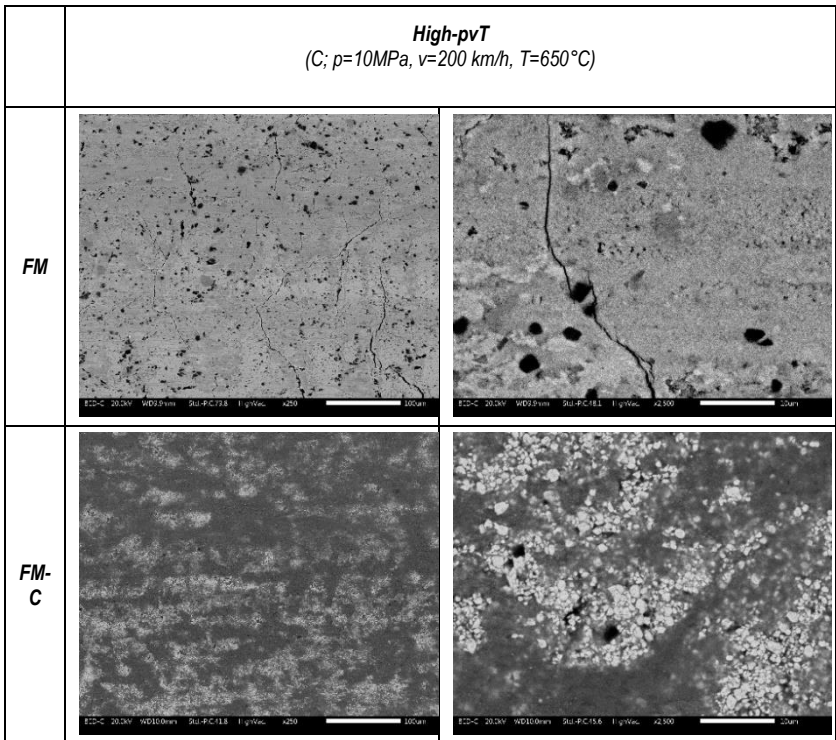


Fig. 6.5.13: BED observations at different magnitudes of the surfaces of the cast-iron and coated disc after braking tests conducted at the testing conditions of *High-pvT*.

6.5.5 Main wear mechanisms

The present study is a comparison between the brake performance of a cermet-coated disc and a conventional cast-iron disc. As described in Section 5.2.3, both discs were coupled with low-met friction materials. The influence of pvT conditions on the brake performance, in terms of friction coefficient, was investigated under mild and severe sliding conditions with an internal Brembo testing procedure. This brake cycle was developed to map the brake performance as a function of pvT . The tests covered a wide range of conditions: 0.7-4.8 MPa of contact pressure, 8-21 m/s of initial sliding speed and 50-650 °C of initial disc temperature, with temperature rises from 50 to above 300 °C (Fig. 6.5.1). An extensive characterization of the worn surfaces of the discs and, especially, the friction materials was done to understand the relationship between the frictional behavior and the surface characteristics. In addition, tests at specific braking conditions provided important information regarding the wear behaviors of the two brake couples. The influence of each braking parameter was described in terms of correlation and variation respectively with Spearman's coefficient, r , and relative standard deviation, RSD . The complex relationship between the pvT parameters and the frictional behavior will be discussed as follows.

The effect of pressure is to cause a decrease in the friction coefficient for both brake couple and all combinations of parameters. This is evident by observing Fig. 6.5.3-4 and, in particular, Spearman's correlation coefficients, Fig. 6.5.5-6, featuring values all negative values, approx. 70 % of the values are -1. Among the braking parameters, the friction coefficient displayed the highest variation (RSD values in Fig. 6.5.5) and pressure is slightly more influential for the coated disc. Decreasing effects of pressure on the friction coefficient are typical observations in large areas of contact: load increases do not correspond to a proportional increase in the contact, hence the friction coefficient decreases [69][100]. In addition, pressure contributes to the formation of wear particles into the secondary plateaus by two actions. First, higher pressure favors the compaction of wear particles. Second, increasing pressure reduces the distance between the mating surfaces decreasing, consequently, the motion capability of the wear particles and their probability of leaving the tribosystem. The secondary plateaus affect the friction coefficient depending on the nature of the iron [95], whether metallic or oxide, of the secondary plateaus and their extension [59][89]. As will be discussed, the vT parameters have a stronger influence on the characteristics of the secondary plateaus.

As confirmed by the two clear peaks at -1 and +1 in the distribution of the correlation coefficient (Fig. 6.5.6), the temperature featured both a decreasing and increasing effect on the friction coefficient depending on the v and T levels.

The first effect of T is to cause an increase in the friction coefficient between 50-300 °C and all velocities for both the brake couples. For the cast-iron disc, this behavior holds, although with a lower intensity, for the initial brake temperature above 300 °C at the initial vehicle speed of 90 km/h. In this case, the increase in friction coefficient is ascribed to two phenomena. First, high contact temperatures cause softening of the friction material [75], thus, a higher degree of conformity in the contact. Higher conformity means a higher area of contact, hence a higher friction coefficient according to the theory of adhesion (Section 3.2).

Second, higher temperatures increase the probability to activate Van der Waals bonds [37], thus higher tangential forces between the surfaces in contact. Interestingly, between the T range of 50-300 °C, the brake couple display a different sensitivity to T (Fig. 6.5.3-4). The coated disc displays a higher friction coefficient with lower variability, $RSD_{\mu T}$ in Fig. 6.5.5, than the cast-iron disc. The explanation for these differences in frictional behavior is ascribed to the different characteristics of the surfaces. The surfaces of both friction materials featured comparable coverage factors, of approximately 40 %. However, the *FM-C* did not feature the typical secondary plateaus and the contact is attained mainly on primary plateaus and brass fibers. Secondary plateaus for the *FM-C* were identified as the Fe particles deposited onto the brass fibers owing better support than the typical secondary plateaus. Thus, as the extension of secondary plateaus is more sensitive to T than fibers, the friction coefficient of the *FM* displays higher sensitivity to T than the *FM-C*. The higher percentage of fibers in the contact also explains the higher friction coefficient of the *FM-C*, as suggested by the study [101]. Although the materials under study are different, these characteristics of the friction layer suggest the reason for the lower wear rate of the *FM-C*. The wear rate of the friction materials is typical for mild sliding conditions approx. $2-4 \cdot 10^{-14} \text{ m}^2/\text{N}$. Higher extension of primary plateaus in the contact of the *FM-C* means that the local stresses are comparatively lower, hence the surface attained lower wear.

The second effect of *T* on the friction coefficient is to cause a decrease in the friction coefficient and it occurs as a combination of high *vT conditions*. This effect is evident between 300-650 °C of initial disc temperature, and 200 km/h for both brake couples, and also at relatively high pressure for the velocity of 90-140 km/h for the coated disc. For both materials, secondary plateaus are very compacted and large glaze with a coverage factor above 70 % (Fig. 6.5.10 and Table 6.5.2). The formation of glazes is favored by high *vT conditions* as tribo-oxidative processes increase in intensity with *T* and *T rises* [48]. Furthermore, these sliding conditions (approx. above 600 °C and 10 m/s) are in the regime of *severe oxidation wear* for steels identified by Lim and Ashby [102]. In this *severe wear regime*, the source of Fe-oxide in the contact significantly increases. The oxides become plastic and form thick and large layers, thus the friction coefficient decreases as the oxide layers are easily deformed. In addition, the very high peak temperatures in the range of 900-1000 °C could determine local melting conditions for the oxides [102]. The studies by [103][104] for brake application ascribed a lubricating effect to compacted oxide layers on the surface of friction materials. As mentioned, the decrease in the friction coefficient passing from 300 to 650 °C of initial disc temperature is well correlated to the increase in the coverage factor and, in particular, to the steel fibers being progressively covered by the glaze layers. Steel fibers are tightly embedded in the pad matrix and compared to glaze layers they have higher mechanical strength and adhesion, hence they can exert higher tangential forces. Interestingly, for the cast-iron disc, the marked decrease of the friction coefficient is marked above 4 MPa and for the coated disc above 2 MPa. At lower *p* levels, the friction coefficient is stable to values of 0.5 and 0.6 respectively for the cast-iron and coated discs. This suggests that for high *vT* conditions, above a certain level of *p*, different for each system, glaze layers are stable, although, of course, they form, and destroy, at a high rate.

Thus, the different nature and wear behaviors between the two discs were important factors determining the different frictional behavior. The wear rate high $p\nu T$ conditions are comparable for both discs. Although the wear rate is considered in the *mild wear regime*, as of $3 \cdot 10^{-14} \text{ m}^2/\text{N}$, it is 6 times higher than the wear at low $p\nu T$ conditions for the cast-iron disc, and of few orders higher the coated disc (Fig. 6.5.7). A variation in the wear mechanisms is supported by the presence of loose particles (Fig. 6.5.11) on the surface of the *FM-C*. Comparing the EDXS analysis (Table 6.5.3) we can infer that they are mainly composed of W, thus originating from the disc, as the W content is, approx. 30 wt.%, three times higher than in the glaze regions. A sound explanation for this increase in the wear rate and the high amount of W in the friction layers is the catastrophic oxidation that Tungsten-based coatings may undergo above $550 \text{ }^\circ\text{C}$ [105][106]. For an initial speed of 200 km/h and initial disc temperature of $300 \text{ }^\circ\text{C}$, the peak temperatures are above 550°C (Fig. 6.5.1), thus oxidation is likely to occur at high velocity. On the other hand, the disc temperature is not always above $550 \text{ }^\circ\text{C}$ for the low and intermediate initial disc temperatures, thus the oxidation process of tungsten carbide is of lower intensity and may not occur at every brake event or require a higher number of brake stops. Thus, this mechanism could have played an important role in the, already mentioned, friction instability at low-intermediate velocity and high T . Regarding the wear rate of the friction materials under high $p\nu T$ conditions, the K_a is comparable and very high, approx. $30 \cdot 10^{-14} \text{ m}^2/\text{N}$. The increase in the wear rate of organic-based composites is strictly related to the degradation of the binder above $300\text{-}400 \text{ }^\circ\text{C}$ [51].

For the cast iron disc, between $300\text{-}650 \text{ }^\circ\text{C}$, the frictional behavior is controlled by the intensity of tribo-oxidative processes: at *high* v (200 km/h), the lubricating effect of the glaze is dominant, whereas the friction coefficient is observed to increase at low v (90 km/h) for the increasing adhesion and conformity in the contact, whereas at the intermediate v (140 km/h) the two effects are competing equally and the friction coefficient is rather stable. On the other hand, in this T range and *low-intermediate* v , the frictional behavior of the coated disc displayed friction instability. As described in Section 6.5.2, it means that the friction coefficient shows high fluctuations for relatively small variations of pT conditions. The surface of the *FM-C* shows scarce but very large and compacted patches. These patches are enriched in W, 55 % respect the 5 % at the conditions of low $p\nu T$. The interpretation of this behavior is that the source of oxide particles is too low to allow for the formation of stable glaze layers because the coating has a significantly lower content of Fe, approx. 13 wt.%. The absence of the lubricating effect and redistribution of stresses played by secondary plateaus, or glazes, result in high adhesion and local stresses. Consequently, as confirmed by EDXS analysis in Table 6.5.3, a high amount of disc material transfer, approx. 55 wt.% of W content, onto the surface of the friction material. Although the material transfer from the disc is high, the wear rate is negligible, comparable to low $p\nu$ conditions, in the range of $10^{-17} \text{ m}^2/\text{N}$ (Fig. 6.5.7). This confirms that the source of particles from the disc that contribute to the formation of secondary plateaus is low. On the other hand, the wear rate of the friction materials at these conditions is already severe, in the range $7\text{-}10 \cdot 10^{-14} \text{ m}^2/\text{N}$, and it is slightly higher for the *FM-C* probably for the higher local stresses due to the lower contact area.

Finally, from the sparse distribution of the correlation coefficient, the direct effect of v seems undefined. However, when the combination of vT for high values is considered, the

velocity becomes a significant parameter as it strongly increases tribo-oxidative processes. For the cast iron disc, the variation of the friction coefficient with v is lower than that is for p and T . On the other hand, the coated disc displayed a high variation with v , comparable with p . This is a consequence of the discussed *friction instability* observed at low intermediate velocity.

Chapter VII

Conclusions

In the present work, the influence of the bedding process and the braking parameters on the frictional, wear and emission behaviors of brake materials have been studied on a reduced-scale dynamometer with specifically developed testing protocols. This dynamometer was equipped with an LVDT sensor providing the wear value at different stages of the tests, and a system for the emission measurements was designed to allow for the collection of the airborne PM from the fine to the coarse fraction. The applied methodology employed *a-posteriori* SEM-EDXS analysis to correlate the observed behaviors with the surface characteristics.

Regarding the bedding process of the reference low-met material, run-in, transition stage and steady states were identified for the frictional, wear and emission behaviors. The frictional behavior achieved a steady state in a relatively low number of brake stops compared to the wear and emission behaviors. The frictional behavior stabilized thanks to the surface coverage by the secondary plateaus. During the *run-in* and the beginning of the transition state, the specific wear rises up to a stable value, typical for mild wear. During the run-in, the rise in emissions was correlated to the increase of the extension of the secondary plateaus. Whereas, during the *transition state*, the increase in the compaction of the secondary plateaus determined the decrease in the emissions. The wear mechanism of compacted friction layers, typical of the *steady state*, favored the detachment of large flake-like debris. These considerations are important as the bedding process affects the lifetime of brake materials and their environmental implications.

This work provides a comparison between a low-met and NAO material. The tests covered a wide range of conditions: 0.7-3.7 MPa of contact pressure (p), 4.2-16.8 m/s of initial sliding speed (v). The initial brake disc temperature (T) was fixed at 100 °C, and the temperature rises between 50-150 °C.

The influence of p and v was evaluated in the p - v -blocks. The original part of the braking cycle was the factorial design, the p - v -blocks, with the *reference blocks* (*Reduced cycle*). The reference blocks were conducted under mild conditions after each the p - v -block to establish the same surface conditions, before *the following* p - v -block. In the reference blocks, the friction coefficient and the emissions reduced their variability tending to typical values of the steady state. The more uniform and extended friction layer of the NAO, with the coverage factor higher by approx. 35 %, provided higher friction stability compared to the reference low-met material. Tribo-oxidative process was the dominant mechanism contributing to the formation of the friction layers: the Fe-O content is 60%-25%, in the secondary plateaus of the low-met, and 30%-35% for the NAO material, respectively. In the low-met material, repeated braking at high velocity caused a progressive decrease in the friction coefficient and this was correlated with the damage of the secondary plateaus. For the NAO materials, on

the other hand, with conditions of high velocity, the friction layer is thicker and more compact. The lower variation of contact area for the NAO material determined the lower sensitivity of the friction coefficient under different $p\nu$ conditions. The wear rate and emissions of the NAO material were lower than with the low-met material. In particular, at low ν the behaviors are comparable, whereas, at high ν , the wear and emissions of the low-met are significantly higher than in the NAO material. The wear rate of the NAO material displayed just a slight increase, approximately linear, with ν , compared to the wear rate of the low-met material, which significantly increased with ν with an approximately quadratic relationship. For both materials, the mean concentration of emitted airborne particles was described by a cubic relationship with ν . From low to high ν , the emissions changed by approx. two orders of magnitude. The pressure was not significantly influencing the particle emissions, if not in a monotonous way.

From tests of the *Reduced Cycle* of several friction materials sliding against cast-iron discs, a linear relationship was found between the specific wear rate of the system and the *emission factor*. This relationship identified a wear rate below $4 \cdot 10^{-14} \text{ m}^2/\text{N}$ to respect the Euro 7 limitation of 3 mg/km/vehicle after 2034. Among the friction materials sliding against cast iron discs, the NAO material and only one friction material displayed an *emission factor* below the limit of 3 mg/km/vehicle. The *emission factor* was lower than this limit also for the low-met material sliding against a cermet-coated disc. These observations confirmed that the NAO materials and coated discs are good strategies to mitigate emissions and that further efforts are required to improve the emission behavior of low-met materials. The found relationship represents a useful tool in the design of brake couples to comply with the limit of the Euro 7 regulation and to lower the emissions.

Regarding the brake performance, under severe sliding conditions, the NAO material displayed worse frictional and wear behaviors than the reference low-met material. The influence of the $p\nu T$ parameters on the brake performance under mild and severe conditions was studied with the *pνT-friction Maps Brake Cycle*. This brake cycle was developed to map the brake performance as a function of $p\nu T$ in a wide range of conditions: 0.7-4.8 MPa of contact pressure, 8-21 m/s of initial sliding speed and 50-650 °C of initial disc temperature, with temperature rises from 50 to above 300 °C. This work provided a comparison between a WC-Fe-Al-Cr cermet-coated and a conventional cast-iron disc. The effect of p was decreasing for all combinations of parameters and it was the most influential parameter for both brake couples. p influenced the formation of the secondary plateaus, however, it had a lower influence than ν and T on the tribo-oxidation and formation of large glazes. The effect of T on the friction coefficient was to cause an increase in the response variable up to 300 °C as the tribo-oxidative processes were contained. The surfaces of both friction materials featured comparable coverage factors, of approximately 40 %. For the low-met material sliding against the cast-iron disc, at the different T , the variation in the Fe-O contents of the secondary plateaus was, approx. 65%-20%, relatively low. Whereas, at the different testing conditions, the composition of the secondary plateaus of the FM-C showed high variation: the Fe-content varied from 20 % to 50 % and the W-content 5-55 wt.%. For the coated disc, the conditions below 14 m/s and above 300 °C were identified as *friction instability*, because the friction coefficient displayed high fluctuations for small variations of p

and T values. Under these conditions, the K_a of the friction materials was typical of severe wear in the range of 7-10 10^{-14} m^2/N . The wear rate of the coated disc was negligible and mild, 0.5 10^{-14} m^2/N , for the cast iron disc. The high values of friction were associated with scarce in number but very large compacted patches of the surface of the *FM-C*. On the other hand, for both brake couples, above 300°C and 14 m/s, the low values of the friction coefficient were observed in association with very large glazes. Under these conditions, the tribo-oxidative processes were intense enough to form large and thick glaze layers covering above 70 % of the surfaces of both friction materials. Regarding the wear rate of the friction materials, the specific wear rates, K_a , are comparable and very high, approx. 30 10^{-14} m^2/N , whereas the wear rates of the two discs are comparable, approx. 3 10^{-14} m^2/N .

Chapter VIII

Future Perspectives

The efforts made in the past years to reduce the particulate matter originating from brake systems have been finally delineated by the Euro 7 regulations. To comply with the stricter limitations and to improve the air quality, future works should focus on the development of materials for brake linings with low emissions and testing methodologies that can ease their development.

From the materials point of view, the formulations of low-met materials require strong improvements when coupled with conventional cast-iron discs. The deposition of new coating can reduce significantly the emission of this class of materials, although new tribological couples should be verified from several standpoints, mainly the brake performance and environmental hazard in terms of compositions of the wear products. The deposition of wear-resistant coatings on the disc surface should be also considered to allow for a wide diffusion of the technology. Further study should investigate how the already low emissions levels of the NAO materials can be further reduced, possibly as new formulations in combination with improvements in the wear resistance of discs. For NAO materials, an important focus is the improvement of the brake performance under severe conditions.

Testing methodologies should be designed in order to identify the peculiar behaviors of brake materials under a wide range of braking conditions and to include the modeling of the brake performance and emission behaviors with the relevant parameters. To improve the modeling of these behaviors, methodologies should focus on both mechanical properties and surface characterization of the materials to separate and quantify the surface and bulk effects on the material performance. The bedding process of new formulations of friction materials and, especially, new disc materials should be investigated, including specific mechanical and surface characterization, for their role in the lifetime performance of brake systems.

Bibliography

- [1] R. Dante, *Handbook of friction materials and their applications*. Woodhead publishing, 2015.
- [2] G. Perricone *et al.*, "A concept for reducing PM10 emissions for car brakes by 50%," *Wear*, vol. 396–397, no. January 2017, pp. 135–145, 2018, doi: 10.1016/j.wear.2017.06.018.
- [3] R. Kumar, I. Hussainova, R. Rahmani, and M. Antonov, "Solid Lubrication at High-Temperatures—A Review," *Materials (Basel)*, vol. 15, no. 5, 2022, doi: 10.3390/ma15051695.
- [4] M. H. Cho, J. Ju, S. J. Kim, and H. Jang, "Tribological properties of solid lubricants (graphite, Sb₂S₃, MoS₂) for automotive brake friction materials," *Wear*, vol. 260, no. 7–8, pp. 855–860, 2006, doi: 10.1016/j.wear.2005.04.003.
- [5] T. Grigoratos and G. Martini, "Brake wear particle emissions: a review," *Environ. Sci. Pollut. Res.*, vol. 22, no. 4, pp. 2491–2504, 2015, doi: 10.1007/s11356-014-3696-8.
- [6] B. D. Garg, S. H. Cadle, P. A. Mulawa, P. J. Groblicki, C. Laroo, and G. A. Parr, "Brake wear particulate matter emissions," *Environ. Sci. Technol.*, vol. 34, no. 21, pp. 4463–4469, 2000, doi: 10.1021/es001108h.
- [7] P. G. Sanders, N. Xu, T. M. Dalka, and M. M. Maricq, "Airborne brake wear debris: Size distributions, composition, and a comparison of dynamometer and vehicle tests," *Environ. Sci. Technol.*, vol. 37, no. 18, pp. 4060–4069, 2003, doi: 10.1021/es034145s.
- [8] P. Chandra Verma, L. Menapace, A. Bonfanti, R. Ciudin, S. Gialanella, and G. Straffelini, "Braking pad-disc system: Wear mechanisms and formation of wear fragments," *Wear*, vol. 322–323, pp. 251–258, 2015, doi: 10.1016/j.wear.2014.11.019.
- [9] H. Hagino, M. Oyama, and S. Sasaki, "Laboratory testing of airborne brake wear particle emissions using a dynamometer system under urban city driving cycles," *Atmos. Environ.*, vol. 131, pp. 269–278, 2016, doi: 10.1016/j.atmosenv.2016.02.014.
- [10] Y. F. Xing, Y. H. Xu, M. H. Shi, and Y. X. Lian, "The impact of PM2.5 on the human respiratory system," *J. Thorac. Dis.*, vol. 8, no. 1, pp. E69–E74, 2016, doi: 10.3978/j.issn.2072-1439.2016.01.19.
- [11] M. Gasser *et al.*, "Toxic effects of brake wear particles on epithelial lung cells in vitro," *Part. Fibre Toxicol.*, vol. 6, no. 1, pp. 1–13, 2009, doi: 10.1186/1743-8977-6-30.
- [12] M. Riediker *et al.*, "Cardiovascular effects in patrol officers are associated with fine particulate matter from brake wear and engine emissions," *Part. Fibre Toxicol.*, vol. 1, pp. 1–10, 2004, doi: 10.1186/1743-8977-1-2.
- [13] V. Roubicek, H. Raclavska, D. Juchelkova, and P. Filip, "Wear and environmental aspects of composite materials for automotive braking industry," *Wear*, vol. 265, no. 1–2, pp. 167–175, 2008, doi: 10.1016/j.wear.2007.09.006.
- [14] G. Straffelini and S. Gialanella, "Airborne particulate matter from brake systems: An assessment of the relevant tribological formation mechanisms," *Wear*, vol. 478–479, no.

- March, p. 203883, 2021, doi: 10.1016/j.wear.2021.203883.
- [15] H. A. C. Denier van der Gon, J. H. J. Hulskotte, A. J. H. Visschedijk, and M. Schaap, "A revised estimate of copper emissions from road transport in UNECE-Europe and its impact on predicted copper concentrations," *Atmos. Environ.*, vol. 41, no. 38, pp. 8697–8710, 2007, doi: 10.1016/j.atmosenv.2007.07.033.
- [16] D. S. T. Hjortenkrans, B. G. Bergbäck, and A. V. Häggerud, "Response to comment on 'Metal emissions from brake linings and tires: Case studies of Stockholm, Sweden 1995/1998 and 2005,'" *Environ. Sci. Technol.*, vol. 42, no. 7, p. 2710, 2008, doi: 10.1021/es7028069.
- [17] G. Straffelini, R. Ciudin, A. Ciotti, and S. Gialanella, "Present knowledge and perspectives on the role of copper in brake materials and related environmental issues: A critical assessment," *Environ. Pollut.*, vol. 207, pp. 211–219, 2015, doi: 10.1016/j.envpol.2015.09.024.
- [18] Q. Zhang *et al.*, "Separation and Tracing of Anthropogenic Magnetite Nanoparticles in the Urban Atmosphere," *Environ. Sci. Technol.*, vol. 54, no. 15, pp. 9274–9284, 2020, doi: 10.1021/acs.est.0c01841.
- [19] D. Plachá *et al.*, "Release of volatile organic compounds by oxidative wear of automotive friction materials," *Wear*, vol. 376–377, pp. 705–716, 2017, doi: 10.1016/j.wear.2016.12.016.
- [20] P. G. Sanders, T. M. Dalka, and R. H. Basch, "A reduced-scale brake dynamometer for friction characterization," *Tribol. Int.*, vol. 34, no. 9, pp. 609–615, 2001, doi: 10.1016/S0301-679X(01)00053-6.
- [21] S. Candeo, M. Federici, M. Leonardi, and G. Straffelini, "Brake Performance Maps for a Cu-Free Friction Material with Different Scorching Conditions," *Tribol. Trans.*, vol. 64, no. 3, pp. 540–550, 2021, doi: 10.1080/10402004.2020.1869360.
- [22] G. Perricone, V. Matějka, M. Alemani, J. Wahlström, and U. Olofsson, "A Test Stand Study on the Volatile Emissions of a Passenger Car Brake Assembly," *Atmosphere (Basel)*, vol. 10, no. 5, p. 263, 2019, doi: 10.3390/atmos10050263.
- [23] G. Perricone, J. Wahlström, and U. Olofsson, "Towards a test stand for standardized measurements of the brake emissions," *Proc. Inst. Mech. Eng. Part D J. Automob. Eng.*, vol. 230, no. 11, pp. 1521–1528, 2016, doi: 10.1177/0954407015616025.
- [24] F. H. F. zum H. M. G. H. R. G. V. Benter, "Study of Brake Wear Particle Emissions: Impact of Braking and Cruising Conditions," *Technol.20195395143-5150, Cite This Environ. Sci. Publ. Date April 2, 2019.*
- [25] G. Perricone, M. Alemani, J. Wahlström, and U. Olofsson, "A test stand investigation on a real driving cycle emission factor for car brakes," no. 1.
- [26] "SAEJ2707, Wear test procedure on inertia dynamometer for brake friction materials, SAE Int (2012)."
- [27] F. H. Farwick zum Hagen *et al.*, "On-road vehicle measurements of brake wear particle emissions," *Atmos. Environ.*, vol. 217, no. August, p. 116943, 2019, doi: 10.1016/j.atmosenv.2019.116943.

- [28] "REGULATION OF THE EUROPEAN PARLIAMENT AND OF THE COUNCIL on type-approval of motor vehicles and engines and of systems, components and separate technical units intended for such vehicles, with respect to their emissions and battery durability (Euro 7) and."
- [29] M. Mathissen *et al.*, "A novel real-world braking cycle for studying brake wear particle emissions," *Wear*, vol. 414–415, no. May, pp. 219–226, 2018, doi: 10.1016/j.wear.2018.07.020.
- [30] M. Alemani, O. Nosko, I. Metinoz, and U. Olofsson, "A study on emission of airborne wear particles from car brake friction pairs," *SAE Int. J. Mater. Manuf.*, vol. 9, no. 1, pp. 147–157, 2016, doi: 10.4271/2015-01-2665.
- [31] V. Brizmer, Y. Kligerman, and I. Etsion, "Elastic-plastic spherical contact under combined normal and tangential loading in full stick," *Tribol. Lett.*, vol. 25, no. 1, pp. 61–70, 2007, doi: 10.1007/s11249-006-9156-y.
- [32] G. Straffelini, *Friction and Wear: Methodologies for Design and Control*. 2014.
- [33] J. A. GREENWOOD AND J. B. P. WILLIAMSON, "Contact of nominally flat surfaces," *Sci. Vol. 295, No. 1442 (Dec. 6, 1966)*, pp. 300-319, vol. 315, no. 1531, pp. 203–219, 1966.
- [34] K. L. M. D.S. Ramai, L.P. DeMeio, *Fundamentals of adhesion and Interfaces, (1995)*. 1995.
- [35] E. Rabinowicz, "Friction and Wear of Self-Lubricating Metallic Materials.," *Am. Soc. Mech. Eng.*, no. 74-WA/Lub-1, pp. 217–221, 1974.
- [36] E. RABINOWICZ, "Influence of Surface Energy on Friction and Wear Phenomena," *J. Appl. Phys.*, vol. 32, no. 8, 1961.
- [37] M. Yamamoto and K. Nakajima, "A study of the physical adhesive state between solids," *Wear*, vol. 70, no. 3, pp. 321–327, 1981, doi: 10.1016/0043-1648(81)90352-5.
- [38] E. Rabinowicz, "The effect of size on the looseness of wear fragments," *Wear*, vol. 2, no. 1, pp. 4–8, 1958, doi: 10.1016/0043-1648(58)90335-1.
- [39] E. Rabinowicz, *Friction and Wear of Materials*. .
- [40] G. K. Nathan and W. J. D. Jones, "The empirical relationship between abrasive wear and the applied conditions," *Wear*, vol. 9, no. 4, pp. 300–309, 1966, doi: 10.1016/0043-1648(66)90004-4.
- [41] K. H. Cho, H. Jang, Y. S. Hong, S. J. Kim, R. H. Basch, and J. W. Fash, "The size effect of zircon particles on the friction characteristics of brake lining materials," *Wear*, vol. 264, no. 3–4, pp. 291–297, 2008, doi: 10.1016/j.wear.2007.03.018.
- [42] A. Jourani, B. Hagège, S. Bouvier, M. Bigerelle, and H. Zahouani, "Influence of abrasive grain geometry on friction coefficient and wear rate in belt finishing," *Tribol. Int.*, vol. 59, pp. 30–37, 2013, doi: 10.1016/j.triboint.2012.07.001.
- [43] S. S. Kim, H. J. Hwang, M. W. Shin, and H. Jang, "Friction and vibration of automotive brake pads containing different abrasive particles," *Wear*, vol. 271, no. 7–8, pp. 1194–1202, 2011,

doi: 10.1016/j.wear.2011.05.037.

- [44] R. Bilz and K. M. de Payrebrune, "Investigation of the influence of velocity in a tribological three-body system containing a single layer of rolling hard particles from a mechanical point of view," *Tribol. Int.*, vol. 159, no. November 2020, p. 106948, 2021, doi: 10.1016/j.triboint.2021.106948.
- [45] I. M. H. R.I. Trezona, D.N. Allsopp, "Transitions between two-body and three-body abrasive wear: influence of test conditions in the microscale abrasive wear test," *IEEE Int. Conf. Commun.*, vol. 7, pp. 3777–3783, 2004, doi: 10.1109/icc.2004.1313260.
- [46] M. Godet, "THE THIRD-BODY APPROACH: A MECHANICAL VIEW OF WEAR," *Wear*, vol. 100, pp. 437–452, 1984.
- [47] N. Fillot, I. Iordanoff, and Y. Berthier, "Wear modeling and the third body concept," *Wear*, vol. 262, no. 7–8, pp. 949–957, 2007, doi: 10.1016/j.wear.2006.10.011.
- [48] F. H. Stott, "The role of oxidation in the wear of alloys," *Tribol. Int.*, vol. 31, no. 1–3, pp. 61–71, 1998, doi: 10.1016/S0301-679X(98)00008-5.
- [49] J. Jiang, F. H. Stott, and M. M. Stack, "The role of triboparticulates in dry sliding wear," *Tribol. Int.*, vol. 31, no. 5, pp. 245–256, 1998, doi: 10.1016/S0301-679X(98)00027-9.
- [50] H. Blok, "The flash temperature concept," *Wear*, vol. 6, no. 6, pp. 483–494, 1963, doi: 10.1016/0043-1648(63)90283-7.
- [51] A. L. Cristol-Bulthé, Y. Desplanques, G. Degallaix, and Y. Berthier, "Mechanical and chemical investigation of the temperature influence on the tribological mechanisms occurring in OMC/cast iron friction contact," *Wear*, vol. 264, no. 9–10, pp. 815–825, 2008, doi: 10.1016/j.wear.2006.12.080.
- [52] M. Alemani *et al.*, "Dry sliding of a low steel friction material against cast iron at different loads: Characterization of the friction layer and wear debris," *Wear*, vol. 376–377, pp. 1450–1459, 2017, doi: 10.1016/j.wear.2017.01.040.
- [53] J. Kukutschová, V. Roubí, J. Kuba, D. Maccrimmon, and P. Filip, "Wear mechanism in automotive brake materials , wear debris and its potential environmental impact," vol. 267, pp. 807–817, 2009, doi: 10.1016/j.wear.2009.01.034.
- [54] P. Chandra, L. Menapace, A. Bonfanti, R. Ciudin, S. Gialanella, and G. Straffellini, "Braking pad-disc system : Wear mechanisms and formation of wear fragments," *Wear*, vol. 322–323, pp. 251–258, 2015, doi: 10.1016/j.wear.2014.11.019.
- [55] W. Österle, M. Griepentrog, T. Gross, and I. Urban, "Chemical and microstructural changes induced by friction and wear of brakes," *Wear*, vol. 250–251, no. PART 2, pp. 1469–1476, 2001, doi: 10.1016/s0043-1648(01)00785-2.
- [56] G. P. Ostermeyer and M. Müller, "Dynamic interaction of friction and surface topography in brake systems," *Tribol. Int.*, vol. 39, no. 5, pp. 370–380, 2006, doi: 10.1016/j.triboint.2005.04.018.
- [57] P. J. Blau, "On the nature of running-in," *Tribol. Int.*, vol. 38, no. 11-12 SPEC. ISS., pp. 1007–

- 1012, 2005, doi: 10.1016/j.triboint.2005.07.020.
- [58] X. Xiao, Y. Yin, J. Bao, L. Lu, and X. Feng, "Review on the friction and wear of brake materials," *Adv. Mech. Eng.*, vol. 8, no. 5, pp. 1–10, 2016, doi: 10.1177/1687814016647300.
- [59] M. Eriksson, F. Bergman, and S. Jacobson, "On the nature of tribological contact in automotive brakes," *Wear*, vol. 252, no. 1–2, pp. 26–36, 2002, doi: 10.1016/S0043-1648(01)00849-3.
- [60] J. Park *et al.*, "Analysis of wear induced particle emissions from brake pads during the worldwide harmonized light vehicles test procedure (WLTP)," *Wear*, vol. 466–467, no. September 2020, p. 203539, 2021, doi: 10.1016/j.wear.2020.203539.
- [61] M. Federici, M. Alemani, C. Menapace, S. Gialanella, G. Perricone, and G. Straffelini, "A critical comparison of dynamometer data with pin-on-disc data for the same two friction material pairs – A case study," *Wear*, vol. 424–425, no. February, pp. 40–47, 2019, doi: 10.1016/j.wear.2019.02.009.
- [62] A. P. G. Nogueira, M. Leonardi, G. Straffelini, and S. Gialanella, "Sliding Behavior and Particle Emissions of Cu-Free Friction Materials with Different Contents of Phenolic Resin," *Tribol. Trans.*, vol. 0, no. 0, p. 000, 2020, doi: 10.1080/10402004.2020.1753870.
- [63] "SAEJ2522, Dynamometer Global Brake Effectiveness," *SAE Int.*, 2014, doi: 10.4271/2012-01-0107.
- [64] V. Matějka, I. Metinöz, J. Wahlström, M. Alemani, and G. Perricone, "On the running-in of brake pads and discs for dyno bench tests," *Tribol. Int.*, vol. 115, no. March, pp. 424–431, 2017, doi: 10.1016/j.triboint.2017.06.008.
- [65] D. Hesse, C. Hamatschek, K. Augsburg, T. Weigelt, A. Prahst, and S. Gramstat, "Testing of alternative disc brakes and friction materials regarding brake wear particle emissions and temperature behavior," *Atmosphere (Basel)*, vol. 12, no. 4, 2021, doi: 10.3390/atmos12040436.
- [66] M. Eriksson and S. Jacobson, "Tribological surfaces of organic brake pads," *Tribol. Int.*, vol. 33, no. 12, pp. 817–827, 2000, doi: 10.1016/S0301-679X(00)00127-4.
- [67] H. Niemann, H. Winner, C. Asbach, H. Kaminski, and M. Zessinger, "Map Based Simulation of Brake Wear Particle Emissions," pp. 1–10, 2020, doi: 10.46720/eb2020-stp-022.
- [68] J. Wahlström, V. Matějka, Y. Lyu, and A. Söderberg, "Contact pressure and sliding velocity maps of the friction, wear and emission from a low-metallic/cast-iron disc brake contact pair," *Tribol. Ind.*, vol. 39, no. 4, pp. 460–470, 2017, doi: 10.24874/ti.2017.39.04.05.
- [69] C. Study, "Load, speed and temperature sensitivities of a carbon-fiber- reinforced phenolic friction material," vol. 183, pp. 913–921, 1995.
- [70] M. Kumar and J. Bijwe, "NAO friction materials with various metal powders: Tribological evaluation on full-scale inertia dynamometer," *Wear*, vol. 269, no. 11–12, pp. 826–837, 2010, doi: 10.1016/j.wear.2010.08.011.
- [71] K. Tanaka, S. Ueda, and N. Noguchi, "Fundamental studies on the brake friction of resin-

- based friction materials," *Wear*, vol. 23, no. 3, pp. 349–365, 1973, doi: 10.1016/0043-1648(73)90022-7.
- [72] W. Österle and A. I. Dmitriev, "Functionality of conventional brake friction materials - Perceptions from findings observed at different length scales," *Wear*, vol. 271, no. 9–10, pp. 2198–2207, 2011, doi: 10.1016/j.wear.2010.11.035.
- [73] G. P. Ostermeyer, "On the dynamics of the friction coefficient," *Wear*, vol. 254, no. 9, pp. 852–858, 2003, doi: 10.1016/S0043-1648(03)00235-7.
- [74] V. Ricciardi *et al.*, "A novel semi-empirical dynamic brake model for automotive applications," *Tribol. Int.*, vol. 146, no. January, p. 106223, 2020, doi: 10.1016/j.triboint.2020.106223.
- [75] U. S. Hong, S. L. Jung, K. H. Cho, M. H. Cho, S. J. Kim, and H. Jang, "Wear mechanism of multiphase friction materials with different phenolic resin matrices," *Wear*, vol. 266, no. 7–8, pp. 739–744, 2009, doi: 10.1016/j.wear.2008.08.008.
- [76] F. Eddoumy *et al.*, "Role of constituents of friction materials on their sliding behavior between room temperature and 400°C," *Mater. Des.*, vol. 65, pp. 179–186, 2015, doi: 10.1016/j.matdes.2014.08.048.
- [77] P. C. Verma, R. Ciudin, A. Bonfanti, P. Aswath, G. Straffellini, and S. Gialanella, "Role of the friction layer in the high-temperature pin-on-disc study of a brake material," *Wear*, vol. 346–347, pp. 56–65, 2016, doi: 10.1016/j.wear.2015.11.004.
- [78] O. Nosko and U. Olofsson, "Quantification of ultrafine airborne particulate matter generated by the wear of car brake materials," *Wear*, vol. 374–375, pp. 92–96, 2017, doi: 10.1016/j.wear.2017.01.003.
- [79] M. Alemani, J. Wahlström, and U. Olofsson, "On the influence of car brake system parameters on particulate matter emissions," *Wear*, vol. 396–397, no. November 2017, pp. 67–74, 2018, doi: 10.1016/j.wear.2017.11.011.
- [80] M. Vojtišek-Lom *et al.*, "Effects of braking conditions on nanoparticle emissions from passenger car friction brakes," *Sci. Total Environ.*, vol. 788, 2021, doi: 10.1016/j.scitotenv.2021.147779.
- [81] G. Perricone, M. Alemani, I. Metinöz, V. Matějka, J. Wahlström, and U. Olofsson, "Towards the ranking of airborne particle emissions from car brakes - A system approach," *Proc. Inst. Mech. Eng. Part D J. Automob. Eng.*, vol. 231, no. 6, pp. 781–797, 2017, doi: 10.1177/0954407016662800.
- [82] H. Niemann, H. Winner, C. Asbach, H. Kaminski, G. Frentz, and R. Milczarek, "Influence of disc temperature on ultrafine, fine, and coarse particle emissions of passenger car disc brakes with organic and inorganic pad binder materials," *Atmosphere (Basel)*, vol. 11, no. 10, 2020, doi: 10.3390/atmos11101060.
- [83] H. Hagino, M. Oyama, and S. Sasaki, "Airborne brake wear particle emission due to braking and accelerating," *Wear*, vol. 334–335, pp. 44–48, 2015, doi: 10.1016/j.wear.2015.04.012.
- [84] Y. Liu *et al.*, "Brake wear induced PM10 emissions during the world harmonised light-duty vehicle test procedure-brake cycle," *J. Clean. Prod.*, vol. 361, no. May, p. 132278, 2022, doi: 10.1016/j.jclepro.2022.132278.

- 10.1016/j.jclepro.2022.132278.
- [85] Z. Men *et al.*, "Determining factors and parameterization of brake wear particle emission," *J. Hazard. Mater.*, vol. 434, no. January, p. 128856, 2022, doi: 10.1016/j.jhazmat.2022.128856.
- [86] Hinds, "aerosol technology," *Int. J. Environ. Health*, vol. 2, no. 2, pp. 69–70, 2006, doi: 10.1080/17449200600935521.
- [87] M. Federici, C. Menapace, A. Mancini, G. Straffellini, and S. Gialanella, "Pin-on-disc study of dry sliding behavior of Co-free HVOF-coated disc tested against different friction materials," *Friction*, vol. 9, no. 5, pp. 1242–1258, 2021, doi: 10.1007/s40544-020-0463-3.
- [88] D. C. Montgomery, *Design and Analysis of Experiments Eighth Edition*. .
- [89] S. Candeo, M. Leonardi, S. Gialanella, and S. Straffellini, "Influence of contact pressure and velocity on the brake behaviour and particulate matter emissions," *Wear*, vol. 514–515, no. November 2022, p. 204579, 2023, doi: 10.1016/j.wear.2022.204579.
- [90] J. F. Archard, "Contact and rubbing of flat surfaces," *J. Appl. Phys.*, vol. 24, no. 8, pp. 981–988, 1953, doi: 10.1063/1.1721448.
- [91] F. Varriale, S. Candeo, G. Riva, J. Wahlström, and Y. Lyu, "A Brake System Coefficient of Friction Estimation Using 3D Friction Maps," *Lubricants*, vol. 10, no. 7, p. 134, 2022, doi: 10.3390/lubricants10070134.
- [92] S. Candeo, A. P. Nogueira, M. Leonardi, and G. Straffellini, "A study of friction, wear and particulate emissions during the bedding stage of a Cu-free friction material," *Wear*, vol. 486–487, no. August, p. 204095, 2021, doi: 10.1016/j.wear.2021.204095.
- [93] M. Leonardi, C. Menapace, V. Matějka, S. Gialanella, and G. Straffellini, "Pin-on-disc investigation on copper-free friction materials dry sliding against cast iron," *Tribol. Int.*, vol. 119, no. October 2017, pp. 73–81, 2018, doi: 10.1016/j.triboint.2017.10.037.
- [94] A. Paula, G. Nogueira, D. Carlevaris, C. Menapace, and G. Stra, "Tribological and Emission Behavior of Novel Friction Materials," 2020.
- [95] M. Federici, S. Gialanella, M. Leonardi, G. Perricone, and G. Straffellini, "A preliminary investigation on the use of the pin-on-disc test to simulate off-brake friction and wear characteristics of friction materials," *Wear*, vol. 410–411, no. May, pp. 202–209, 2018, doi: 10.1016/j.wear.2018.07.011.
- [96] G. Straffellini, *Friction and Wear Methodologies for Design and Control*. 2016.
- [97] J. Wahlström, A. Söderberg, L. Olander, U. Olofsson, and A. Jansson, "Airborne wear particles from passenger car disc brakes: A comparison of measurements from field tests, a disc brake assembly test stand, and a pin-on-disc machine," *Proc. Inst. Mech. Eng. Part J J. Eng. Tribol.*, vol. 224, no. 2, pp. 179–188, 2010, doi: 10.1243/13506501JET633.
- [98] J. W. Kim, B. S. Joo, and H. Jang, "The effect of contact area on velocity weakening of the friction coefficient and friction instability : A case study on brake friction materials," vol. 135, no. December 2018, pp. 38–45, 2019, doi: 10.1016/j.triboint.2019.02.034.

- [99] W. Österle and I. Urban, "Third body formation on brake pads and rotors," *Tribol. Int.*, vol. 39, no. 5, pp. 401–408, 2006, doi: 10.1016/j.triboint.2005.04.021.
- [100] M. Kumar and J. Bijwe, "Role of different metallic fillers in non-asbestos organic (NAO) friction composites for controlling sensitivity of coefficient of friction to load and speed," *Tribol. Int.*, vol. 43, no. 5–6, pp. 965–974, 2010, doi: 10.1016/j.triboint.2009.12.062.
- [101] F. Varriale, G. Riva, J. Wahlström, and Y. Lyu, "A Mesoscopic Simulation Approach Based on Metal Fibre Characterization Data to Evaluate Brake Friction Performance," *Lubricants*, vol. 10, no. 3, 2022, doi: 10.3390/lubricants10030034.
- [102] S. C. Lim and M. F. Ashby, "Overview no. 55 Wear-Mechanism maps," *Acta Metall.*, vol. 35, no. 1, pp. 1–24, 1987, doi: 10.1016/0001-6160(87)90209-4.
- [103] F. A. & Sultan Ö. Bülent Öztürk, "Effects of Different Kinds of Fibers on Mechanical and Tribological Properties of Brake Friction Materials." *Tribology Transactions*, 2013.
- [104] J. R. Gomes, O. M. Silva, C. M. Silva, L. C. Pardini, and R. F. Silva, "The effect of sliding speed and temperature on the tribological behavior of carbon-carbon composites," *Wear*, vol. 249, no. 3–4, pp. 240–245, 2001, doi: 10.1016/S0043-1648(01)00554-3.
- [105] W. Zhou, K. Zhou, Y. Li, C. Deng, and K. Zeng, "High temperature wear performance of HVOF-sprayed Cr 3 C 2 -WC-NiCoCrMo and Cr 3 C 2 -NiCr hardmetal coatings," *Appl. Surf. Sci.*, vol. 416, pp. 33–44, 2017, doi: 10.1016/j.apsusc.2017.04.132.
- [106] G. Bolelli, L. M. Berger, M. Bonetti, and L. Lusvardi, "Comparative study of the dry sliding wear behaviour of HVOF-sprayed WC-(W,Cr)2C-Ni and WC-CoCr hardmetal coatings," *Wear*, vol. 309, no. 1–2, pp. 96–111, 2014, doi: 10.1016/j.wear.2013.11.001.

Appendix A: Participation in Congresses, Schools and Workshops

- Tribology International Conference 2023, April 26th-28th 2023, Lisbon, Portugal;
- Metallurgy Summer School – Surface Engineering of Metals, July 24th-27th 2022, Bertinoro, Italy;
- EuroBrake 2022, May 17th-19th, online conference;
- PM 2022, May 18th-20th 2022, Bologna, Italy;
- EuroBrake 2021, May 17th -21st 2021, online conference;
- Winter School ECOPADS - From linear to circular thinking, December 2nd-6th 2019 Trento, Italy.

Appendix B: List of publications

- S. Candeo, M. Leonardi, S. Gialanella, and S. Straffelini, "Influence of contact pressure and velocity on the brake behaviour and particulate matter emissions," *Wear*, vol. 514–515, no. November 2022, p. 204579, 2023;
- S. Candeo, A. P. Nogueira, M. Leonardi, and G. Straffelini, "A study of friction, wear and particulate emissions during the bedding stage of a Cu-free friction material," *Wear*, vol. 486–487, no. August, p. 204095, 2021;
- S. Candeo, M. Federici, M. Leonardi, and G. Straffelini, "Brake Performance Maps for a Cu-Free Friction Material with Different Scorching Conditions," *Tribol. Trans.*, vol. 64, no. 3, pp. 540–550, 2021.
- A. Sinha, S. Candeo, G. Straffelini, and S. Gialanella, "TEM characterization of particulate matter emissions from the bedding stage of a Cu-free brake friction material," *Tribol. Int.*, vol. 188, no. May, p. 108832, 2023, doi: 10.1016/j.triboint.2023.108832.
- P. Jayashree, S. Candeo, M. Leonardi, C. Fidelio, and G. Straffelini, "Effect of the Addition of Waste Generated during the Plasma Cutting of Aluminum Products on the Friction and Emission Properties of a Commercial Friction Material Formulation," *Atmosphere (Basel)*, vol. 13, no. 12, 2022;
- P. Jayashree, S. Candeo, V. Matějka, K. Foniok, M. Leonardi, and G. Straffelini, "Study on the effect of the addition of bulk and exfoliated graphitic carbon nitride on the dry sliding behavior of a commercial friction material formulation through pin on disc and subscale dynamometer analysis," *Tribol. Int.*, vol. 179, no. December 2022, pp. 1–12, 2023;
- F. Varriale, S. Candeo, G. Riva, J. Wahlström, and Y. Lyu, "A Brake System Coefficient of Friction Estimation Using 3D Friction Maps," *Lubricants*, vol. 10, no. 7, p. 134, 2022;
- M. Rahimi, S. Candeo, M. Da Lio, F. Biral, J. Wahlström, and D. Bortoluzzi, "A novel approach for brake emission estimation based on traffic microsimulation, vehicle system dynamics, and machine learning modeling," *Atmos. Pollut. Res.*, vol. 14, no. 10, 2023, doi: 10.1016/j.apr.2023.101872.

Acknowledgements

My PhD was carried out at the Department of Industrial Engineering of the University of Trento. Here, the mixed experience of different research groups was a great gift, I found both a friendly and inspirational place. I am deeply grateful to my supervisor Giovanni Straffellini for his valuable guidance, support and motivation throughout my PhD research. I admire his passion for metals and tribology and I admire his kindness. A special thanks to my co-supervisor Stefano Gialanella for the valuable comments, explanations, and his great ability to make you comfortable with jokes. I am also deeply grateful to the Brembo organization and Andrea Bonfanti for the awesome collaboration with the University of Trento. I thank my colleagues, first in Trento, then moved to Brembo, Ana and Mara. My friends and colleagues in the tribology lab: Ankur, Hossein, Davide, Domenico, Priya and Sunil. My friends and colleagues Alberto, Michele. I am grateful to my old friend Andrea, a constant presence in my life, you were part of the journey in Trento too. To my new friend in Trento, Riccardo and many others, for the funny moments and quality talks. To Luca, you showed me what love is, I am glad you chose me as your best man. To Predrag and Samule, for the good beers and talks in my hometown. To Aleksandar, my old friend who always understands me. To Martina, everything is so simple with you. I thank my parents, Cristina and Francesco, for their support and my special big brothers Ettore and Enrico.